Icarus 200 (2009) 581–615

Contents lists available at ScienceDirect

Icarus

www.elsevier.com/locate/icarus

Analysis of Titan's neutral upper atmosphere from Cassini Ion Neutral Mass Spectrometer measurements

J. Cui[a,e,*], R.V. Yelle[a], V. Vuitton[b], J.H. Waite Jr.[c], W.T. Kasprzak[d], D.A. Gell[c], H.B. Niemann[d], I.C.F. Müller-Wodarg[e], N. Borggren[a], G.G. Fletcher[c], E.L. Patrick[d], E. Raaen[d], B.A. Magee[c]

[a] *Lunar and Planetary Lab., University of Arizona, Tucson, AZ 85721, USA*
[b] *Laboratoire de Planétologie de Grenoble, Université Joseph Fourier/CNRS, Grenoble Cedex 9, France*
[c] *Southwest Research Institute, San Antonio, TX 78228, USA*
[d] *NASA, Goddard Space Flight Center, Greenbelt, MD 20771, USA*
[e] *Space and Atmospheric Physics Group, Imperial College London, London SW7 2BW, UK*

ARTICLE INFO

Article history:
Received 10 August 2008
Revised 9 December 2008
Accepted 12 December 2008
Available online 24 December 2008

Keywords:
Atmospheres, composition
Atmospheres, structure
Titan

ABSTRACT

In this paper we present an in-depth study of the distributions of various neutral species in Titan's upper atmosphere, between 950 and 1500 km for abundant species (N_2, CH_4, H_2) and between 950 and 1200 km for other minor species. Our analysis is based on a large sample of Cassini/INMS (Ion Neutral Mass Spectrometer) measurements in the CSN (Closed Source Neutral) mode, obtained during 15 close flybys of Titan. To untangle the overlapping cracking patterns, we adopt Singular Value Decomposition (SVD) to determine simultaneously the densities of different species. Except for N_2, CH_4, H_2 and ^{40}Ar (as well as their isotopes), all species present density enhancements measured during the outbound legs. This can be interpreted as a result of wall effects, which could be either adsorption/desorption of these molecules or heterogeneous surface chemistry of the associated radicals on the chamber walls. In this paper, we provide both direct inbound measurements assuming ram pressure enhancement only and abundances corrected for wall adsorption/desorption based on a simple model to reproduce the observed time behavior. Among all minor species of photochemical interest, we have firm detections of C_2H_2, C_2H_4, C_2H_6, CH_3C_2H, C_4H_2, C_6H_6, CH_3CN, HC_3N, C_2N_2 and NH_3 in Titan's upper atmosphere. Upper limits are given for other minor species.

The globally averaged distributions of N_2, CH_4 and H_2 are each modeled with the diffusion approximation. The N_2 profile suggests an average thermospheric temperature of 151 K. The CH_4 and H_2 profiles constrain their fluxes to be 2.6×10^9 cm^{-2} s^{-1} and 1.1×10^{10} cm^{-2} s^{-1}, referred to Titan's surface. Both fluxes are significantly higher than the Jeans escape values. The INMS data also suggest horizontal/diurnal variations of temperature and neutral gas distribution in Titan's thermosphere. The equatorial region, the ramside, as well as the nightside hemisphere of Titan appear to be warmer and present some evidence for the depletion of light species such as CH_4. Meridional variations of some heavy species are also observed, with a trend of depletion toward the north pole. Though some of the above variations might be interpreted by either the solar-driven models or auroral-driven models, a physical scenario that reconciles all the observed horizontal/diurnal variations in a consistent way is still missing. With a careful evaluation of the effect of restricted sampling, some of the features shown in the INMS data are more likely to be observational biases.

1. Introduction

Titan has a thick and extended atmosphere, which is composed of at least four distinct regions: troposphere, stratosphere, mesosphere and thermosphere (Yelle, 1991). Throughout Titan's atmosphere below the exobase, the most abundant constituent is N_2, followed by several percent of CH_4 and several tenths of percent of H_2. Other minor species, including various hydrocarbons and nitrogen-bearing species, are also present on Titan, as products of the complicated photochemical network initiated by the dissociation of N_2 and CH_4 by solar UV photons, energetic ions/electrons from Saturn's magnetosphere, as well as cosmic ray particles (e.g., Yung et al., 1984). This paper focuses on the distributions of various neutral constituents in Titan's thermosphere above 950 km, which coexists with an ionosphere (e.g., Bird et al., 1997; Wahlund et al., 2005; Kliore et al., 2008).

---

* Corresponding author at: Space and Atmospheric Physics Group, Imperial College London, London SW7 2BW, UK.
E-mail address: jcui@imperial.ac.uk (J. Cui).

0019-1035/$ – see front matter © 2008 Elsevier Inc. All rights reserved.
doi:10.1016/j.icarus.2008.12.005

During the pre-Cassini epoch, our information on the structure and composition of Titan's thermosphere relied exclusively on the disk-averaged dayglow spectra and solar occultation data obtained with the Voyager UltraViolet Spectrometer (UVS) (e.g., Broadfoot et al., 1981; Smith et al., 1982; Strobel and Shemansky, 1982; Strobel et al., 1992; Vervack et al., 2004). These earlier results have been used extensively to develop models of Titan's upper atmosphere in various aspects, including photochemistry (e.g., Yung et al., 1984; Toublanc et al., 1995; Lara et al., 1996; Banaszkiewicz et al., 2000; Wilson and Atreya, 2004), ionospheric structure (e.g., Ip, 1990; Gan et al., 1992; Keller et al., 1992; Fox and Yelle, 1997), thermal structure (e.g., Lellouch et al., 1990; Yelle, 1991), non-thermal escape (e.g., Lammer and Bauer, 1993; Cravens et al., 1997; Lammer et al., 1998; Shematovich et al., 2001, 2003; Michael et al., 2005; Michael and Johnson, 2005), as well as dynamics (e.g., Rishbeth et al., 2000; Müller-Wodarg et al., 2000, 2003, Müller-Wodarg and Yelle, 2002).

The first in situ measurements of the concentrations of various species in Titan's thermosphere have been made by the Ion Neutral Mass Spectrometer (INMS) on the Cassini orbiter during its close Titan flybys (Waite et al., 2005). The INMS results, combined with observations made by other instruments onboard Cassini/Huygens, provide extensive information on the composition and structure of Titan's atmosphere, and will certainly initiate many new modeling efforts. Results of investigation based on INMS have already been presented in Waite et al. (2005, 2007), Cravens et al. (2006), Yelle et al. (2006, 2008), De La Haye et al. (2007a, 2007b), Lavvas et al. (2008a, 2008b), Vuitton et al. (2006, 2007, 2008), Cui et al. (2008), Müller-Wodarg et al. (2006, 2008) and Hörst et al. (2008). Primary scientific goals of the INMS investigation include (1) to understand the detailed photochemistry leading to the formation of various hydrocarbons, nitrogen-bearing species and oxygen compounds on Titan; (2) to examine Titan's atmospheric response to solar and magnetospheric energy inputs; and (3) to constrain the dynamics and escaping processes in Titan's upper atmosphere (Waite et al., 2004).

The INMS instrument consists of separate ion sources for sampling neutrals (in the Closed Source Neutral mode, hereafter CSN) and ions (in the Open Source Ion mode, hereafter OSI) in the coupled thermosphere and ionosphere of Titan (Waite et al., 2004). The INMS data obtained in the OSI mode have been presented recently by Cravens et al. (2006), Vuitton et al. (2007) and Waite et al. (2007) revealing that the composition of Titan's ionosphere is very complex, with ∼50 ion species detected by the INMS. Starting from the measured ion abundances and based on an ion-neutral chemistry model, Vuitton et al. (2007) calculated the densities of various neutral species in Titan's upper atmosphere. These predicted results can be compared with direct INMS measurements in the CSN mode, which helps to constrain more tightly the ion/neutral formation mechanisms in Titan's upper atmosphere.

In this paper, we present our analysis of a large sample of INMS measurements in the CSN mode, aimed at providing an extensive information on the abundances of various neutral species, both globally averaged and horizontally/diurnally varied in Titan's thermosphere, between 950 and 1500 km for abundant species (N_2, CH_4, H_2) and between 950 and 1200 km for other minor species. This study serves as an extension of the work by Waite et al. (2005) based on the INMS data from the TA flyby, and is also complementary to the work by Vuitton et al. (2007) based on the INMS T5 data in the OSI mode. Basic information on the instrumentation and observation is detailed in Section 2. We describe in Section 3 the basic algorithm to derive abundances of different neutral species, as well as an assessment of the primary source of errors. Results are given in Section 4, including a discussion of possible wall effects (Section 4.1), the globally averaged distributions of various neutral species (Section 4.2), as well as their possible horizontal/diurnal variations (Section 4.3). Finally, we summarize and conclude in Section 5. For reference, we present our detailed procedures of calibrating the raw INMS data in Appendix A.

2. Instrumentation and observation

The spectral analysis presented in this paper relies exclusively on the measurements made in the CSN mode, which is specifically designed to optimize interpretation of the sampled neutral species (Waite et al., 2004). In this mode, the inflowing gas particles enter the orifice of a spherical antechamber, and thermally accommodate to the wall temperature through collisions. These particles then enter the ionization region where they get ionized by a collimated electron beam emitted from hot-filament electron guns. A quadrupole switching lens and other electrostatic lenses focus these ions into a dual radio frequency quadrupole mass analyzer, which filters the incoming ion fluxes according to their mass-to-charge ratios (hereafter M/Z, Waite et al., 2004). A schematic drawing of the INMS instrument can be found in Waite et al. (2004) (see their Fig. 2.5).

Within the four years' length of the prime Cassini mission, there have been over 40 encounters with Titan. Our work is based on the INMS data acquired during 15 of them, known in project parlance as T5, T16, T18, T19, T21, T23, T25, T26, T27, T28, T29, T30, T32, T36 and T37. Part of this sample has been used in our previous investigations of N_2, CH_4, H_2 and ^{40}Ar on Titan (Müller-Wodarg et al., 2008; Yelle et al., 2008; Cui et al., 2008). In this study, for abundant species such as N_2, CH_4 and H_2, we investigate their distributions below the exobase at ∼1500 km, while for other minor constituents including various hydrocarbons, nitrogen-bearing species, and oxygen compounds, our analysis is constrained to altitudes below 1200 km. The INMS data from other low altitude flybys are excluded for various reasons: (1) The INMS operated only in the OSI mode during the T4 flyby; (2) The TA, T9, T13, T17 and T34 flybys primarily cover regions of Titan's upper atmosphere above the altitude range of our interest; (3) A software error occurred during the T7 flyby; (4) For all other flybys (including TB, T3, T6, T8, T10, T11, T12, T14, T15, T20, T22, T24, T31, T33 and T35), the spacecraft orientation was not appropriate for INMS measurements, with the ram angle at closest approach (hereafter C/A) greater than 60° (see Section A.2).

The main characteristics of all flybys at C/A are detailed in Table 1, including the date of observation, altitude, local solar time, latitude, longitude and F10.7 cm solar flux at 1 AU (i.e., the 10.7 cm

Table 1
Summary of the trajectory geometry at C/A for all Titan flybys used in this study. Altitudes (ALT) are given in km; local solar times (LST) are given in h; latitudes (LAT) and longitudes (LON) are given in degrees, with latitudes defined as positive north and the longitude values of 270° and 90° representing ideal magnetospheric ram and wake directions. The F10.7 cm solar fluxes are given in units of 10^{-22} W Hz^{-1} m^{-2} at 1 AU.

Flyby	Date	ALT (km)	LST (h)	LAT (deg)	LON (deg)	F10.7
T5	4/16/05	1027	23.28	74	271	83
T16	7/22/06	950	17.35	85	315	74
T18	9/23/06	960	14.42	71	357	70
T19	10/9/06	980	14.34	61	357	75
T21	12/12/06	1000	20.33	43	265	102
T23	1/13/07	1000	14.02	31	358	81
T25	2/22/07	1000	0.58	30	16	76
T26	3/10/07	981	1.76	32	358	71
T27	3/26/07	1010	1.72	41	358	74
T28	4/10/07	991	1.67	50	358	69
T29	4/26/07	981	1.60	59	358	81
T30	5/12/07	960	1.53	69	359	71
T32	6/13/07	965	1.31	85	1.2	71
T36	10/2/07	973	16.13	−60	109	66
T37	11/19/07	999	15.47	−21	117	70

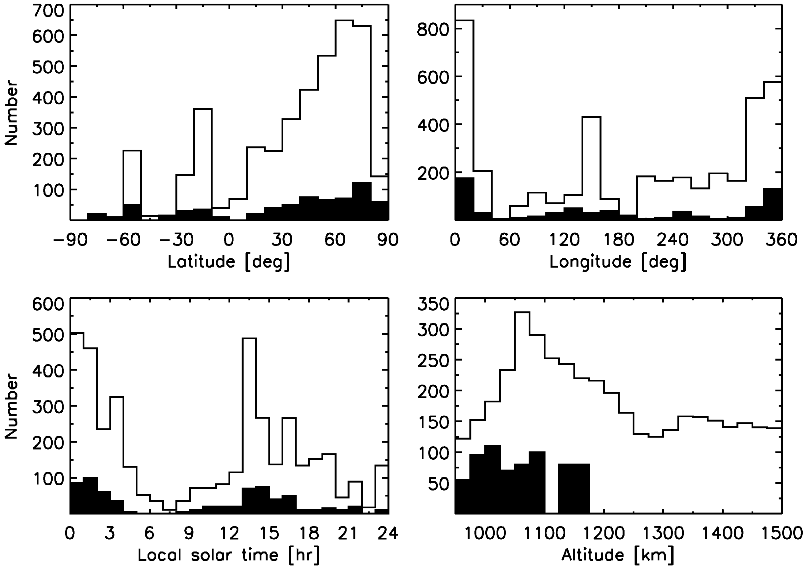

Fig. 1. The distribution of the INMS sample adopted in this work, with respect to latitude, longitude, local solar time, as well as altitude. The sample is exclusively for solar minimum conditions, and preferentially selects measurements made over Titan's northern hemisphere and the facing-Saturn side. The open histograms represent the sampling of abundant species including N_2, CH_4 and H_2, extending from 950 km to 1500 km. The filled histograms represent the sampling of other minor species (multiplied by a factor of 5), which is restricted to altitudes below 1200 km.

solar radio flux at 1 AU in $\mathrm{W\,Hz^{-1}\,m^{-2}}$ multiplied by 10^{22}). Latitude is defined as northward positive. Longitude values of 270° and 90° correspond to the ideal magnetospheric ram and wake directions. The data sampling covers more than two and a half years, between Apr 16, 2005 for T5 and Nov 19, 2007 for T37. The F10.7 cm solar fluxes are adopted from the daily values reported by the Dominion Radio Astrophysical Observatory at Penticton, B.C., Canada. Table 1 shows that altitudes at C/A range from 950 km for T16 to 1027 km for T5.

We show in Fig. 1 the distribution of the INMS sample adopted in this work with respect to latitude, longitude, local solar time and altitude. The geometric information represented by the open histograms is extracted from channel 28 of all flybys, between 950 and 1500 km. This represents the sample distributions for abundant species including N_2, CH_4 and H_2 analyzed in this work. The filled histograms represent the sample distributions for minor species, whose abundances are derived from the best-fit solutions to individual mass spectra below 1200 km (see Section 3.1 for details). In Fig. 1, the distributions for minor species have been multiplied by a factor of 5. Though both inbound and outbound passes are included in Fig. 1, we will show below that our analysis of most minor species will primarily rely on the inbound measurements. For all species, the sample is unevenly distributed with respect to latitude, in the sense that most measurements were made over Titan's northern hemisphere. The T36 and T37 data are unique since they are the only low altitude flybys probing Titan's southern hemisphere to date. In spite of this, the INMS sample coverage in Titan's southern hemisphere is still too limited to allow possible asymmetry between the northern and southern parts to be identified (see also Section 4.3.1). In terms of the longitude distribution, the sample preferentially selects measurements made over Titan's facing-Saturn side, while the other sides (especially the magnetospheric wakeside) are poorly sampled. The mean F10.7 cm flux at 1 AU for our sample ranges from 66 to 102, with a mean value of 76, therefore the sample exclusively represents solar minimum conditions.

The INMS data in the CSN mode consist of a sequence of number counts in mass channels with mass-to-charge ratios, M/Z in the range of 1–8 and 12–99 Daltons. For channels that are expected to show significant count rates (channels 2, 12–17, 27–29), the INMS measures the ambient atmosphere with a typical sampling time of $\sim$0.92 s, corresponding to a spatial resolution of $\sim$5.5 km along the spacecraft trajectory for a typical flyby velocity of 6 $\mathrm{km\,s^{-1}}$ relative to Titan. These channels are primarily associated with N_2, CH_4 and H_2 in the ambient atmosphere. A special case is channel 28 for the T16 flyby, with a sampling time of 0.034 s, about equal to the INMS mass step dwell time (Waite et al., 2004). For all other channels, the sampling time is $\sim$9.3 s, indicating that the INMS data have a typical spatial resolution of $\sim$56 km for the distributions of minor neutral species.

3. Singular value decomposition (SVD) of the neutral mass spectra

The raw INMS data are first corrected for various systematic uncertainties before they are used to derive the number densities of the ambient neutrals. In the CSN mode, we take into account calibration of sensitivities, ram pressure enhancement, saturation in the high gain counter, thruster firing contaminations, subtraction of background counts, as well as channel cross-talk. The details of these calibrations are presented in Appendix A.

3.1. Basic algorithm

The density determination of neutral constituents in Titan's upper atmosphere is complicated by the fact that the counts in a particular mass channel are likely to be contributed by more than one species. This is a result of the overlapping cracking patterns for various species present on Titan. In general, we can write

$$c_i = \sum_{j=1}^{N} S_{i,j} n_j, \tag{1}$$

where $i = 1, 2, \ldots, M$, $j = 1, 2, \ldots, N$, with M and N being the total numbers of the mass channels and neutral species included in the spectral analysis. In Eq. (1), c_i is the measured count rate in channel i, n_j is the density of the neutral species j, and $S_{i,j}$ represents the element of the sensitivity matrix, which is used to convert the count rates in a given mass channel to the number densities of the associated neutrals (see Section A.1). These sen-

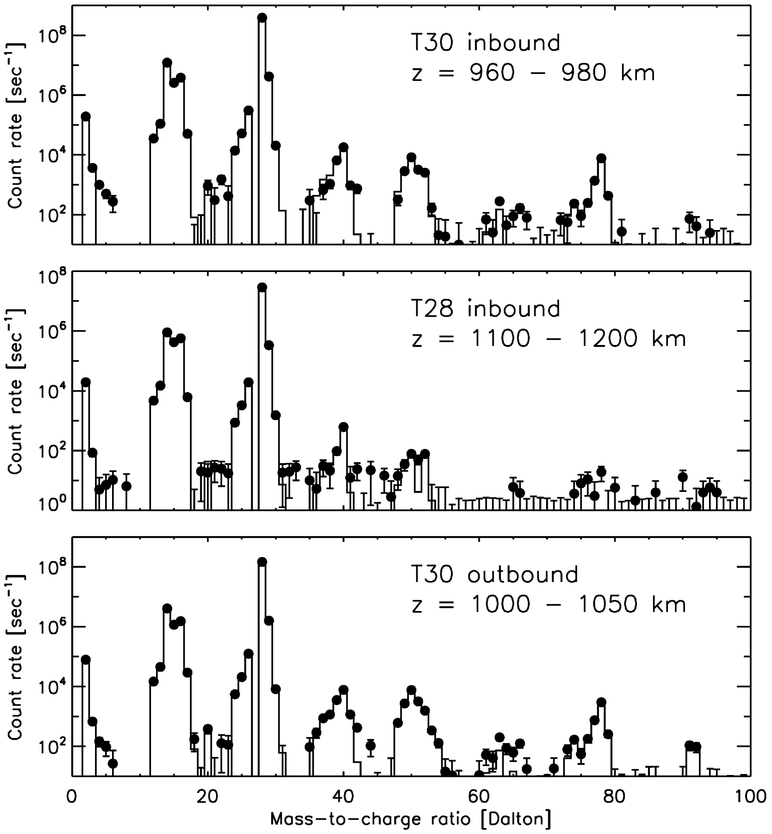

Fig. 2. The INMS mass spectra averaged between 960 and 980 km for the inbound T30 flyby (upper panel), between 1100 and 1200 km for the inbound T28 flyby (middle panel), and between 1000 and 1050 km for the outbound T30 flyby (lower panel). The solid circles give the measurements with 1σ errors due to counting statistics. Instrumental effects have been properly removed from the raw spectra. The count rates in channel 27 are not shown since they are not included in the spectral fitting due to crosstalk. The histograms show the model spectra, which are calculated with calibrated sensitivity values, appropriate ram enhancement factors, and best-fit densities obtained from the SVD algorithm.

sitivity values have also been multiplied by the appropriate ram enhancement factors, which characterize the instrument response to the magnitude and orientation of the spacecraft velocity relative to Titan (see Section A.2). From Eq. (1), the problem of deriving neutral densities from count rates is essentially one of solving the linear algebraic equations for n_j's. In this problem, the number of equations (M) is larger than the number of unknowns (N), which implies that we have to solve for n_j's in a minimum χ^2 sense. Here we adopt specifically the method of Singular Value Decomposition (SVD) to obtain the most probable densities, n_j's for all species. With the SVD decomposition applied to the sensitivity matrix and inserted back into Eq. (1), the solution to n_j's can be written as

$$n_j = \sum_{k=1}^{N}\sum_{i=1}^{M}\left(\frac{u_{ik}c_i}{w_k}\right)v_{jk}, \tag{2}$$

where u_{ij}'s and v_{ij}'s are the elements of the $M \times N$ column-orthogonal matrix $\mathbf{U}$ and the $N \times N$ orthogonal matrix $\mathbf{V}$, w_i's are the non-zero diagonal elements of the $N \times N$ orthogonal matrix $\mathbf{W}$. These matrices satisfy the condition of $\mathbf{S} = \mathbf{U} \times \mathbf{W} \times \mathbf{V}^{\mathrm{T}}$, where $\mathbf{S}$ is the sensitivity matrix in Eq. (1) (Press et al., 1992). The associated density errors can be calculated by

$$\sigma_j = \sqrt{\sum_{i=1}^{M}\left(\sum_{k=1}^{N}\frac{u_{ik}v_{jk}}{w_k}\right)^2 \tilde{\sigma}_i^2}, \tag{3}$$

where σ_j is the density error of species j and $\tilde{\sigma}_i$ is the error of the count rate recorded in channel i. These density errors are associated with counting statistics only.

Three examples of the INMS spectral fits based on the SVD algorithm are given in Fig. 2, for the inbound T30 data between 960 and 980 km (upper panel), the inbound T28 data between 1100 and 1200 km (middle panel), and the outbound T30 data between 1000 and 1050 km (lower panel), respectively. The solid circles show the INMS measurements, averaged over the specified altitude range for a given flyby. Instrumental effects have been properly removed following the procedures described in Appendix A. The signals in channel 27 are not shown since this channel is not included in the SVD fit due to channel crosstalk (see Section A.6). Also shown in Fig. 2 are $\pm 1\sigma$ uncertainties due to counting statistics. The solid histograms in Fig. 2 show the model spectra, that are calculated with calibrated sensitivity values (see Section A.1), appropriate ram enhancement factors (see Section A.2), and best-fit densities obtained from the SVD fit.

At both high and low altitudes, the model spectra reasonably describe the data. The major features near channels 2, 16, 28, 40, 50 and 78 in the observed spectra are well reproduced by the model. These features are mainly associated with H_2, CH_4, N_2, $^{40}Ar/CH_3C_2H$, C_4H_2/HC_3N and C_6H_6, as detailed in Fig. 3. C_6H_6 produces a minor feature near channel 63, which is also consistent with the model prediction (not shown in Fig. 3). Significant deviations occur at channel 42, especially for spectral analysis at relatively low altitudes (see the lower left panel of Fig. 3). This might be a signature of C_3H_6 on Titan. Sensitivity calibration has not been made for this species, and thus it is not included in our spectral analysis (see also Section 3.3).

Comparing the three panels of Fig. 2 immediately shows an interesting feature. Although the densities of any species in general decrease with increasing altitudes, some species show stronger sig-

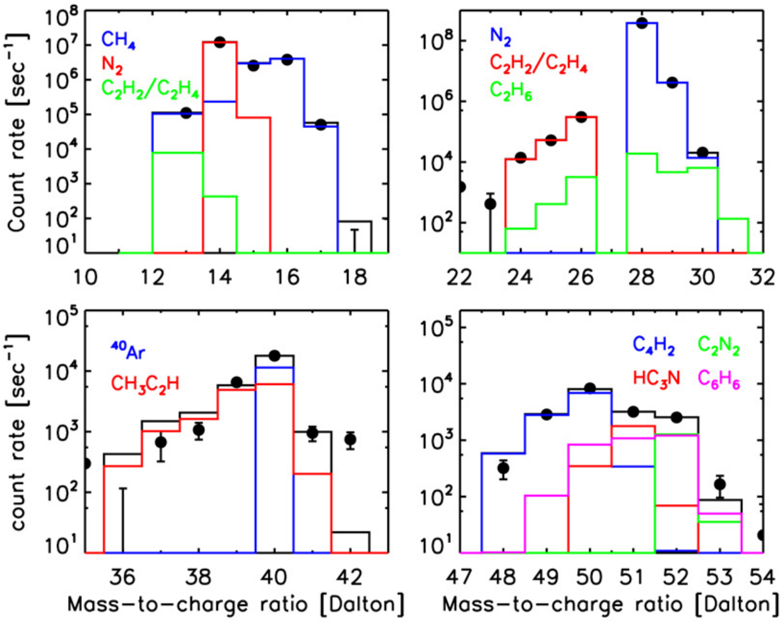

Fig. 3. The INMS mass spectra averaged between 960 and 980 km for the inbound T30 flyby, near mass channels 16 (upper left), 28 (upper right), 40 (lower left) and 50 (lower right). The solid circles give the measurements with 1σ errors due to counting statistics. The histograms with different colors show the model spectra contributed by different neutral components of Titan's upper atmosphere, with the black ones representing the summation. The deviation between model and observation at channel 42 might be a signature of C_3H_6 on Titan.

nals in the outbound spectra, irrespective of altitude. An example is C_7H_8, which is not detected at 3σ significance level from the inbound data, even at the lowest altitudes. However, the spectrum averaged between 1000 and 1050 km for the outbound T30 flyby (the lower panel of Fig. 2) clearly shows a peak near channel 90 which is produced by C_7H_8 molecules. Such a feature can be reasonably explained by the wall effects (Vuitton et al., 2008), and this is found to be the primary source of uncertainty in the determination of minor neutral abundances (see Section 4.1).

3.2. Major neutral species and their isotopes

3.2.1. Nitrogen

The most abundant neutral species in Titan's upper atmosphere is N_2. Its presence was predicted by Hunten (1972) and observationally confirmed with the Voyager UVS instrument (Broadfoot et al., 1981). The cracking patterns of N_2 as well as its isotopes $^{14}N^{15}N$ and $^{15}N^{15}N$ peak at channels 28, 29 and 30, respectively. However, other neutral species in Titan's atmosphere also contribute to counts in these channels, e.g., C_2H_4, C_2H_6 and C_3H_8. This raises a difficulty in the SVD spectral analysis, in which any small fractional change in the derived densities of N_2, $^{14}N^{15}N$ or $^{15}N^{15}N$ causes a large variation in the densities of other neutral species. To avoid this, we directly determine the abundances of N_2 and $^{14}N^{15}N$ from counts in channels 14, 28 and 29, with all necessary calibrations taken into proper account. The detailed procedure for deriving N_2 densities is described in Müller-Wodarg et al. (2008), which is based on counts in the low gain counter (hereafter $C^{(2)}$) of channel 28 at low altitudes, counts in the high gain counter (hereafter $C^{(1)}$) of the same channel at high altitudes, and $C^{(1)}$ counts in channel 14 between (see also Section A.3). The determination of $^{14}N^{15}N$ densities is based on counts in channel 29 only. An estimate of the nitrogen isotope ratio, $y_N = n(^{14}N)/n(^{15}N)$ on Titan can thus be determined, from which we can further obtain the ratio of the $^{15}N^{15}N$ density to N_2 density from $1/[1+y(N)]^2$. With the known densities of N_2 as well as its isotopes ($^{14}N^{15}N$ and $^{15}N^{15}N$), we calculate from their cracking patterns the contributions of these species to channels 14, 15, 28, 29, and 30. These contributions are subtracted from the original mass spectra, and the SVD analysis can then be performed without the difficulty induced by the N_2 density errors. An independent determination of the $^{15}N^{15}N$ densities is important, since the abundances of both $^{15}N^{15}N$ and C_2H_6 are mainly constrained by counts in the same channel (30), and thus the coupling between these two species in the SVD analysis needs to be untangled.

3.2.2. Methane

The second major species in Titan's thermosphere is CH_4, of which the abundances can be derived accurately from the INMS measurements based on counts in channel 16, except below ~1100 km where the $C^{(1)}$ counts of this channel become saturated and the CH_4 densities are alternatively determined from counts in channels 12 and 13 (see Müller-Wodarg et al., 2008 for details). However, the density determination of its isotope, $^{13}CH_4$ suffers from the contamination of NH_3, since the densities of both species are mainly constrained by counts in channel 17.

To untangle the coupling between $^{13}CH_4$ and NH_3, we apply an ad-hoc carbon isotope ratio for a given mass spectrum. This is then used to estimate the $^{13}CH_4$ density from the CH_4 measurement, independent of the actual count rate in channel 17. Here we need to incorporate the vertical variation of the isotope ratio, as a result of diffusive separation since $^{13}CH_4$ is slightly heavier than CH_4 (Lunine et al., 1999). The most recent determination of the carbon isotope ratio on Titan gives $y(CH_4) = n(CH_4)/n(^{13}CH_4) = 82.3 \pm 0.1$, based on the Huygens GCMS measurements made between 6 and 18 km (Niemann et al., 2005). Approximating this value as the carbon isotope ratio at the homopause, which we place at an altitude of 850 km (Yelle et al., 2008), it is easy to show that $y(CH_4) = n(CH_4)/n(^{13}CH_4) = 97.1$ at an altitude of 1150 km, where we have ignored eddy mixing above the homopause as well as CH_4 escape.

The carbon isotope ratio above the homopause can also be estimated directly from the INMS measurements. The upper panel of Fig. 4 shows the mean CH_4 (solid lines) and $^{13}CH_4$ (dashed lines) densities as a function of altitude. The inbound and outbound profiles are given separately by the thin and thick lines, respectively.

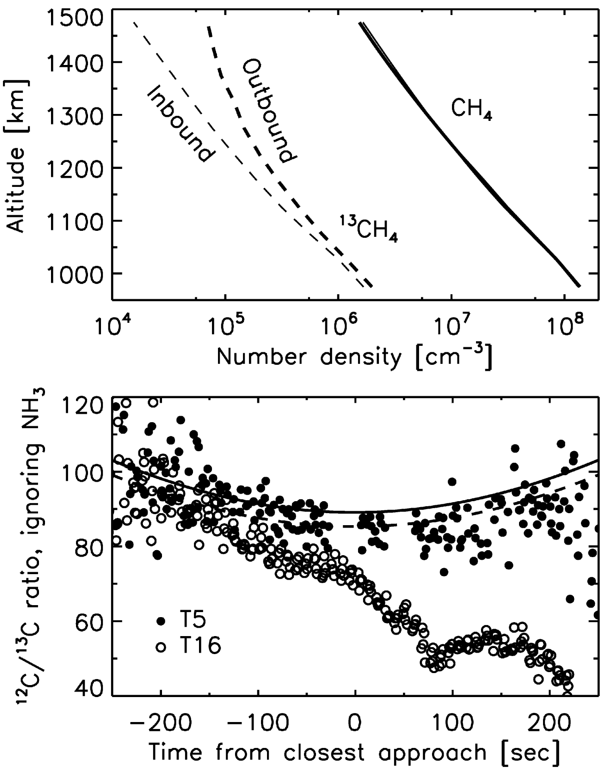

Fig. 4. Upper panel: the mean density profiles of CH_4 (solid lines) and $^{13}CH_4$ (dashed lines) averaged over all flybys, with contribution from NH_3 ignored. The thin and thick lines give the inbound and outbound profiles, respectively. The inbound and outbound profiles of CH_4 are nearly identical, indicating that wall effects are negligible for this species below 1500 km. Lower panel: the observed $^{12}C/^{13}C$ ratio as a function of time from C/A, ignoring the contribution from NH_3. Two extreme cases are shown, one for the T5 flyby with the maximum C/A altitude of 1027 km in our sample, and the other one for the T16 flyby with the minimum C/A altitude of 950 km. The solid and dashed lines give the $^{12}C/^{13}C$ ratios adopted for the T5 and T16 flybys in our SVD analysis, with their variations along the spacecraft trajectories purely due to diffusive separation.

The $^{13}CH_4$ densities in Fig. 4 are calculated from counts in channel 17, ignoring contribution from NH_3 for the moment. The densities shown in the figure are obtained by averaging over all flybys, which should effectively remove possible horizontal and diurnal variations. The CH_4 distribution is symmetric about C/A, indicating that wall effects are not important for this species. The same feature should in principle be observed for $^{13}CH_4$ as well, since both species have similar chemical properties. The asymmetric distribution of $^{13}CH_4$ therefore implies that the counts in channel 17 are actually contributed by both $^{13}CH_4$ and NH_3, of which the latter is subject to wall effects and the former has a symmetric distribution about C/A similar to the observations of CH_4. The lower panel of Fig. 4 further shows the observed $^{12}C/^{13}C$ ratio, ignoring the contributions from NH_3 to counts in channel 17. Two extreme cases are given, one for the T5 flyby with the maximum C/A altitude of 1031 km in our sample, and the other one for the T16 flyby with the minimum C/A altitude of 950 km. The $^{12}C/^{13}C$ ratio does tend to the same constant level above ∼1100 km for the inbound data of both flybys, implying that the contributions from NH_3 are probably negligible for these high altitude inbound measurements. The very low $^{12}C/^{13}C$ ratios obtained from the outbound data, especially for the T16 flyby, suggest that a significant fraction of the channel 17 counts are from NH_3 molecules during the outbound legs. The apparent asymmetry of the NH_3 counts about C/A is a signature of wall effect for this species. The issue of wall effect will be presented in Section 4.1 in a more general context.

Based on the above discussions, we estimate the carbon isotope ratio in Titan's thermosphere by averaging all observed $n(CH_4)/n(^{13}CH_4)$ values between 1100 and 1200 km during the inbound legs of all flybys. This gives $n(^{12}C)/n(^{13}C) = 95.2 \pm 0.1$ at a mean altitude of 1150 km, which is consistent with the value of 97.1 inferred from the GCMS measurements when corrected for diffusive separation. Throughout our SVD analysis, we evaluate the $^{12}C/^{13}C$ ratio in Titan's thermosphere by taking into account diffusive separation, with a boundary condition of $n(^{12}C)/n(^{13}C) = 95.2$ at 1150 km. The calculated $^{12}C/^{13}C$ ratios are shown in the lower panel of Fig. 4 for the T5 (solid line) and T16 (dashed line) flybys.

Finally, we emphasize that in this study, the presence of NH_3 in the observed mass spectra is implied from the distribution of channel 17 counts with respect to time from C/A in the context of wall effects. The detection of NH_3 on Titan will be revisited in Section 4.2.2.

3.3. *Identification of neutral constituents*

One of the key problems in the spectral analysis is to decide what neutral species should be included in the SVD fit described in Section 3.1. The candidate neutrals include N_2, CH_4, H_2, C_2H_2, C_2H_4, C_2H_6, C_3H_4, C_3H_8, C_4H_2, C_4H_6, C_6H_6, C_7H_8, NH_3, HCN, CH_3CN, HC_3N, C_2H_3CN, C_2H_5CN, C_2N_2, H_2O, CO_2 and ^{40}Ar. The isotopes of N_2, CH_4, H_2 and ^{40}Ar are also considered, including $^{14}N^{15}N$, $^{15}N^{15}N$, $^{13}CH_4$, HD and ^{36}Ar. The choice of the above species list is based on (1) results from recent nadir observations made with the Cassini Composite Infrared Spectrometer (CIRS) (Coustenis et al., 2007); (2) predictions from existing photochemical models of Titan's neutral upper atmosphere (e.g., Wilson and Atreya, 2004; Lavvas et al., 2008b); and (3) available sensitivity calibrations (therefore we exclude C_3H_6 though its presence is suggested by the counts in channel 42, see Section 3.1). For a historical description of the identification of various neutral species on Titan, see Waite et al. (2004). It should also be pointed out that the CIRS spectra characterize regions in Titan's stratosphere, well below the altitude range probed by the INMS. Therefore observational evidence for a given species in the CIRS spectra does not necessarily indicate the presence of the same species in the INMS spectra.

In the above list, several neutral species are excluded in our SVD analysis for various reasons, which are detailed as follows. (1) C_3H_4 can be either CH_3C_2H (methylacetylene, with an enthalpy of formation of 185.4 $kJ\,mol^{-1}$) or $CH_2C_2H_2$ (allene with an enthalpy of formation of 199.6 $kJ\,mol^{-1}$). The cracking patterns of both species are similar for the main channels (39 and 40) from which their abundances can be constrained. Therefore, these two species cannot be distinguished reliably based on the INMS data alone. However, recent Cassini/CIRS nadir observations show evidence for the CH_3C_2H ν_9 emission band, whereas signatures for the ν_{10} and ν_{11} bands of $CH_2C_2H_2$ appear to be absent (Coustenis et al., 2007). Theoretically, CH_3C_2H is more stable than $CH_2C_2H_2$, and can be formed indirectly through collisional isomerization of $CH_2C_2H_2$ (Wilson and Atreya, 2004). Considering these, we ignore $CH_2C_2H_2$ in our spectral analysis, though strictly speaking, the derived abundances of CH_3C_2H should refer to the sum of CH_3C_2H and $CH_2C_2H_2$ due to the similarity in their cracking patterns. (2) No direct detection of C_2H_5CN has been reported to date, though it has been predicted from the INMS OSI spectra (Vuitton et al., 2007). More important, the cracking pattern of C_2H_5CN peaks at channel 28, which is dominated by counts from N_2. This implies that the C_2H_5CN densities, even if this species is present in Titan's upper atmosphere, are difficult to be constrained directly with the INMS data. (3) The presence of HCN has been confirmed by Cassini/CIRS observations through its 713 cm^{-1} emission band

(Coustenis et al., 2007). In the context of INMS measurements, the abundances of HCN are mainly constrained by counts in channel 27. However, this channel is ignored in this study since there is no solid way to correct for crosstalk near channel 28 (see Section A.6). For the reasons above, $CH_2C_2H_2$, HCN and C_2H_5CN are excluded from our spectral analysis.

C_2H_2 and C_2H_4 present an additional difficulty in the SVD analysis. Their cracking patterns suggest that in principle, their abundances can be constrained from counts in channels 24–26. The signals in channels 12–14 cannot be reliably used because these channels are dominated by CH_4. For channels 24–26, the branching ratios of C_2H_2 are approximately a factor of 3 higher than those of C_2H_4, i.e., their relative signals in these channels remain nearly the same. This indicates that in practice, the counts in channels 24–26 can only be used to constrain the linear combination of C_2H_2 and C_2H_4 densities in the form of $3n(C_2H_2) + n(C_2H_4)$, where we have ignored the small difference in their ram enhancement factors. In the following spectral analysis, rather than treating the two species separately, we investigate an *imaginary* species with densities set equal to $\frac{3}{4}n(C_2H_2) + \frac{1}{4}n(C_2H_4)$ on Titan. It is easily seen that the sensitivities of this species should be set as four times the C_2H_4 values.

Throughout our analysis, those species with relatively high abundances on Titan are always incorporated, including N_2, CH_4, H_2, C_2H_2, C_2H_4 and their isotopes. Notice that the contributions from N_2, $^{14}N^{15}N$ and $^{15}N^{15}N$ are determined independently and subtracted from the raw data before the SVD fit is applied, the CH_4 to $^{13}CH_4$ density ratio is fixed with an ad-hoc value which takes into account diffusive separation, and the inclusion of C_2H_2 and C_2H_4 is through the linear combination of $\frac{3}{4}n(C_2H_2) + \frac{1}{4}n(C_2H_4)$. The remaining minor species are more difficult to detect at high altitudes. For each of these species, whether it is included in the spectral fit depends on the signal-to-noise ratio of the count rate in its main channel. In more detail, we adopt the following scheme: (1) if $c_{18} > 3\sigma_{18}$, then H_2O is included; (2) if $c_{30} > 3\sigma_{30}$ (with the contribution from $^{15}N^{15}N$ subtracted), then C_2H_6 is included; (3) if $c_{36} > 3\sigma_{36}$, then ^{36}Ar is included; (4) if $c_{39} > 3\sigma_{39}$, then CH_3C_2H is included; (5) if $c_{40} > 3\sigma_{40}$, then ^{40}Ar is included; (6) if $c_{41} > 3\sigma_{41}$, then CH_3CN is included; (7) if $c_{43} > 3\sigma_{43}$, then C_3H_8 is included; (8) if $c_{44} > 3\sigma_{44}$, then CO_2 is included; (9) if $c_{50} > 3\sigma_{50}$, then C_4H_2 is included; (10) if $c_{51} > 3\sigma_{51}$, then HC_3N is included; (11) if $c_{52} > 3\sigma_{52}$, then C_2N_2 is included; (12) if $c_{53} > 3\sigma_{53}$, then C_2H_3CN is included; (13) if $c_{54} > 3\sigma_{54}$, then C_4H_6 is included; (14) if $c_{78} > 3\sigma_{78}$, then C_6H_6 is included; (15) if $c_{91} > 3\sigma_{91}$, then C_7H_8 is included. In all the above expressions, c_i and σ_i represent the count rate in channel i and its uncertainty. Such a scheme is aimed at minimizing the coupling between the cracking patterns of all species. In general, the above inequalities imply that a particular species is considered to be present and included in the spectral analysis, only when it is detected at more than 3σ significance level based on its signal in one of its main channels. On the other hand, if a species is below the detection limit, we estimate an upper limit density based on the 3σ uncertainty of count rate in the same channel.

We notice that the cracking pattern of C_3H_8 peaks at both channels 43 and 44. Therefore in principle, CO_2 does not need to be included in the spectral analysis, if we assign most of the channel 44 counts to C_3H_8. However, in a typical mass spectrum, the ratio of the channel 44 count to channel 43 count is much higher than the corresponding ratio in the C_3H_8 cracking pattern. This implies the presence of CO_2 in the INMS mass spectra, and thus we include both C_3H_8 and CO_2 in the SVD fits. Similarly, the ratio of the channel 40 count to channel 39 count is much higher than the corresponding ratio in the CH_3C_2H cracking pattern, and therefore ^{40}Ar has to be included in the spectral analysis.

The situation for NH_3 is more complicated, since there is no single channel of which the count rate is mainly contributed by this species. Note that $^{13}CH_4$ contributes to a significant fraction of the channel 17 counts in all cases. Here we adopt a scheme in which the SVD fit is applied to a given spectrum with NH_3 always included. However, in many cases the derived NH_3 density is too low to justify the presence of NH_3 at more than 3σ significance level. In such cases, we simply replace the derived NH_3 density with an upper limit evaluated from the density error tripled.

3.4. Error analysis

The density determination based on the SVD analysis described above relies on the most probable sensitivity values either directly taken from the flight unit (FU) measurements or scaled from the refurbished engineering unit (REU) measurements (see Section A.1 for details). Therefore the errors given directly by the SVD fits are associated with counting statistics only. Here we use a Monte-Carlo technique to estimate the extra uncertainties related to sensitivity calibration (see Section A.1). By comparing with uncertainties due to counting statistics, we are then able to identify the dominant source of errors in the derived abundances of all species.

We start from the relative uncertainties of peak sensitivities listed in Table 8, and we further include uncertainties due to calibration of cracking patterns, as detailed in Section A.1.2. For an individual flyby, either inbound or outbound, we perform 1000 SVD fits to the mean mass spectrum obtained by averaging over a given altitude bin. Random choices of the sensitivity values are adopted in these SVD fits, following a Gaussian distribution with the standard deviation taken from the combined uncertainty of peak sensitivity and cracking pattern. For any given spectrum, the densities obtained from these random samples are used to evaluate the uncertainties due to sensitivity calibration for all neutral species. We detail in Table 2 the relative uncertainties of mixing ratios obtained for two representative mass spectra, one for the inbound T16 spectrum between 980 and 1000 km, and the other one for the inbound T36 spectrum between 1050 and 1100 km. Uncertainties due to sensitivity calibration and counting statistics are given separately for comparison.

For relatively abundant constituents in Titan's upper atmosphere, such as CH_4, H_2 and C_2H_2/C_2H_4, uncertainties due to counting statistics are usually smaller than those due to sensi-

Table 2
Relative uncertainties due to counting statistics and sensitivity calibration, for two representative mass spectra (both inbound). In cases where the upper limits are obtained for the mixing ratios of some neutral species, we only give the relative uncertainties due to sensitivity calibration, calculated as the standard deviations of upper limits from 1000 random realizations.

Species	T16 (980–1000 km)		T36 (1050–1100 km)	
	Counting	Sensitivity	Counting	Sensitivity
N_2	3.6×10^{-4}	6.5×10^{-4}	6.1×10^{-4}	2.1×10^{-3}
CH_4	1.9×10^{-3}	2.9×10^{-2}	2.4×10^{-3}	4.5×10^{-2}
H_2	1.1×10^{-2}	2.7×10^{-2}	1.8×10^{-2}	4.8×10^{-2}
C_2H_2/C_2H_4	9.4×10^{-3}	2.9×10^{-2}	1.6×10^{-2}	5.7×10^{-2}
C_2H_6	1.0×10^{-1}	1.4×10^{-1}	1.8×10^{-1}	1.8×10^{-1}
CH_3C_2H	2.5×10^{-1}	4.6×10^{-2}	2.5×10^{-1}	7.8×10^{-2}
C_3H_8	–	4.1×10^{-2}	–	8.0×10^{-2}
C_4H_2	1.9×10^{-1}	4.2×10^{-2}	2.6×10^{-1}	9.2×10^{-2}
C_4H_6	–	7.1×10^{-2}	–	1.3×10^{-1}
C_6H_6	1.2×10^{-1}	5.7×10^{-2}	–	1.1×10^{-1}
C_7H_8	–	6.4×10^{-2}	–	1.4×10^{-1}
NH_3	1.2×10^{-1}	1.5×10^{-1}	–	5.1×10^{-2}
HC_3N	3.6×10^{-1}	9.2×10^{-2}	–	8.7×10^{-2}
CH_3CN	–	7.1×10^{-2}	–	8.1×10^{-2}
C_2H_3CN	–	6.1×10^{-2}	–	6.1×10^{-2}
C_2N_2	4.3×10^{-1}	1.2×10^{-1}	–	1.0×10^{-1}
H_2O	–	6.8×10^{-2}	–	3.8×10^{-2}
CO_2	3.1×10^{-1}	5.9×10^{-2}	–	4.5×10^{-2}
^{40}Ar	7.8×10^{-2}	3.1×10^{-2}	1.4×10^{-1}	9.6×10^{-2}

tivity calibration. This is expected as a result of the high signal-to-noise ratios of counts in their main channels. On the contrary, for many minor constituents, the counting statistics is the dominant source of error in their derived mixing ratios. As the most abundant species, the uncertainties of the N_2 mixing ratios are not strongly affected by sensitivity calibration. This is because the total density varies in response to the N_2 density, leading to a small change of the N_2 mixing ratio. However, the uncertainties of the N_2 number density are still on ∼5% level due to sensitivity calibration. For most species, the relative uncertainties due to sensitivity calibration are typically ∼3–15% at different altitudes, while those due to counting statistics span a considerably large range from smaller than 1% to over 40%, and may vary significantly with altitude.

4. Results

For a given flyby, the fully calibrated count rates in any mass channel are interpolated to the grid of time from C/A defined by channel 26. These interpolated count rates are then divided into several altitude bins, with typical widths of 20–25 km below 1000 km and 50–100 km above. Throughout our analysis, the inbound and outbound data are treated separately. For minor species, only measurements made below 1200 km are considered, and their densities (or 3σ upper limits) are obtained following the SVD algorithm described in the previous section. To retain the full spatial resolution of the INMS data, we adopt the density profiles of N_2, CH_4 and H_2 directly determined from counts in the main channels (e.g., Müller-Wodarg et al., 2008; Cui et al., 2008), and we extend the analysis of these species to Titan's exobase at ∼1500 km. The distribution of these abundant species in Titan's exosphere have been presented in De La Haye et al. (2007a) and Cui et al. (2008), and will not be discussed here. All errors quoted in this section reflect uncertainties associated with both counting statistics and sensitivity calibration (see Section 3.4). A total number of 133 individual spectra are analyzed. Among all the density measurements, 1033 are upper limits. Most of the upper limits are obtained for minor species at relatively high altitudes for inbound measurements. Especially, for C_3H_8, C_4H_6, C_7H_8, C_2H_3CN, CO_2 and H_2O, the SVD fits to most of the observed spectra give 3σ upper limits only.

Each of the density measurements is associated with definite values of altitude, latitude, longitude, local solar time and time from C/A. The combination of all the densities and upper limits provides information on the vertical distribution and horizontal/diurnal variations of all neutral constituents in Titan's upper atmosphere above 950 km. The variations of neutral species with time from C/A do not necessarily provide information on the ambient atmosphere, but reflect whether wall effects are important. An investigation of possible wall effects is necessary for justifying that the derived densities are associated with the ambient atmosphere rather than processes within the instrument. In this section, we start with a discussion of the wall effects in Section 4.1. We present in Section 4.2 the globally averaged vertical profiles of various species in Titan's upper atmosphere, followed by a discussion of possible horizontal and/or diurnal variations in Section 4.3.

4.1. Wall effect

The INMS chamber walls have a certain probability to adsorb molecules entering the instrument orifice. On one hand, the adsorption of incoming molecules on the chamber walls reduces the actual signals, leading to an underestimate of the atmospheric abundances. On the other hand, these molecules are desorbed from the chamber walls at a later time, leading to overestimated values. The latter effect is enhanced by heterogeneous surface chemistry, such as the recombination of H and C_6H_5 radicals to form C_6H_6 molecules on the chamber walls (Vuitton et al., 2008). The recombination of radicals on the chamber walls has been realized in previous analysis of mass spectrometer data, such as been used to derive the densities of atomic N in the Venusian upper atmosphere (Kasprzak et al., 1980).

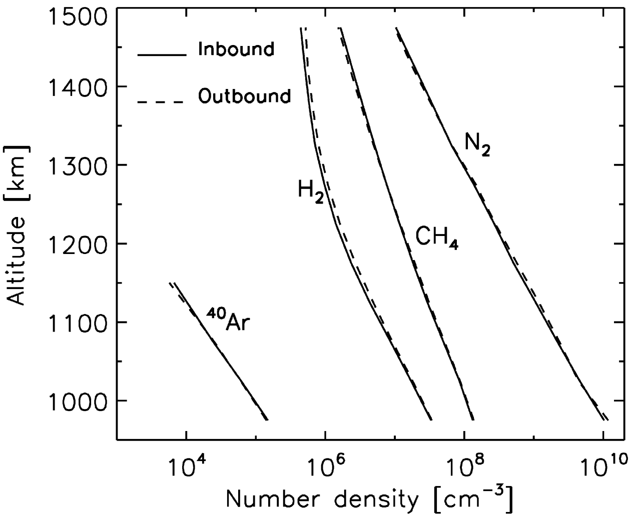

Fig. 5. The density profiles of N_2, CH_4, H_2 and ^{40}Ar, averaged over all flybys. The inbound (solid) and outbound (dashed) profiles are nearly identical, indicating that the wall effects are negligible for these species.

A simple way to examine whether the wall effect is important for a given species is to check the differences between the average inbound and outbound density profiles, as done by Cui et al. (2008). Since other effects such as horizontal and/or diurnal variations tend to be removed by averaging, the appearance of a density enhancement for the average outbound profile is considered as an indication of the wall effects. Alternatively, we may also investigate the density distribution of a given species as a function of time from C/A (also averaged over all flybys), in which wall effects are illustrated as an asymmetric distribution about C/A with a positive time shift.

Fig. 5 shows the density profiles of N_2, CH_4, H_2 and ^{40}Ar measured by INMS, with the solid and dashed lines representing inbound and outbound measurements, respectively. The CH_4 profiles are the same as those shown in the upper panel of Fig. 4. The ^{40}Ar profiles are obtained by averaging densities derived from SVD fits, while the N_2, CH_4 and H_2 densities are directly calculated from counts in their main channels. The inbound and outbound profiles are nearly identical for these species as well as their isotopes (not shown in the figure), indicating that the wall effects are negligible, at least below 1500 km. For N_2, CH_4 and H_2, their densities in the ambient atmosphere are much higher than those involved in wall effects. On the other hand, the wall effect is unlikely to be relevant for ^{40}Ar, which is an inert species. However, it should be pointed out that the outbound densities of N_2 and H_2 may still be affected by wall effects well above the exobase (e.g., Cui et al., 2008), probably as a result of the recombination of H and N atoms on the chamber walls.

In Fig. 6, we show the average density distribution for several minor species, including C_2H_2/C_2H_4, C_4H_2, C_6H_6, C_2N_2, HC_3N and C_2H_3CN. Solid and dashed lines are for inbound and outbound profiles, respectively. Notice that the C_2H_2/C_2H_4 profiles represent densities of the *imaginary* species described in Section 3.3. Some minor species are not detected at more than 3σ significance level, and thus only 3σ upper limits can be put on their densities. Here we use the Kaplan–Meier product-limit estimator to evaluate the mean densities as well as the uncertainties in each altitude bin, us-

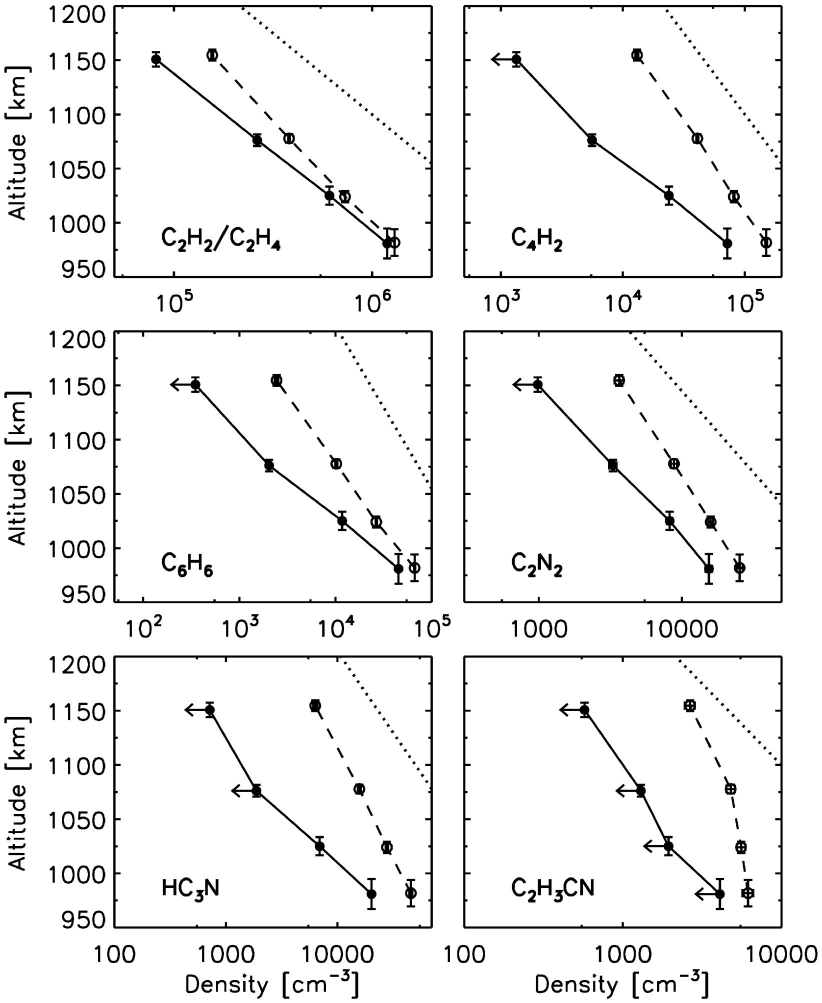

Fig. 6. The density profiles of C_2H_2/C_2H_4, C_4H_2, C_6H_6, C_2N_2, HC_3N and C_2H_3CN, obtained by averaging over all flybys and treating inbound (solid) and outbound (dashed) measurements separately. Leftward arrows indicate upper limit densities. All species show some signature of density enhancement over the outbound legs, indicating that wall effects are important. The dotted lines in the figure show the average N_2 distribution on an arbitrary scale. The scale heights of minor heavy species implied from the outbound measurements are comparable with or even greater than the N_2 scale height, and such an unrealistic feature could be interpreted as a result of wall effects.

ing both exact measurements and upper limits (Feigelson and Nelson, 1985). All species in the figure show clear signatures of wall effects, represented by density enhancement observed on the outbound legs. Especially, we notice that significant C_2H_3CN molecules are detected in the outbound spectra but only upper limits can be put for the inbound measurements. The dotted lines in Fig. 6 give the average N_2 density distribution on an arbitrary scale. For all heavy species shown in the figure, their average outbound profiles show scale heights that are comparable with or even greater than the N_2 scale height. These unrealistic features could be reasonably interpreted as a result of the wall effects.

In Fig. 7, the density profiles of several species are shown as a function of time from C/A, calculated by averaging over all flybys with the Kaplan–Meier product-limit estimator. Downward arrows indicate 3σ upper limits. No scaling has been applied to correct for the vertical variations. The solid line, corresponding to ^{40}Ar, shows a roughly symmetric distribution about C/A and represents a typical case for which the wall effects are not a concern. All other species, including CH_3C_2H, CH_3CN and NH_3, show enhanced densities measured on the outbound legs, and all their profiles peak at a positive time from C/A.

With sufficient information on the details of the adsorption/desorption and surface chemical processes that take place on the INMS chamber walls, it is possible to correct for the wall effects

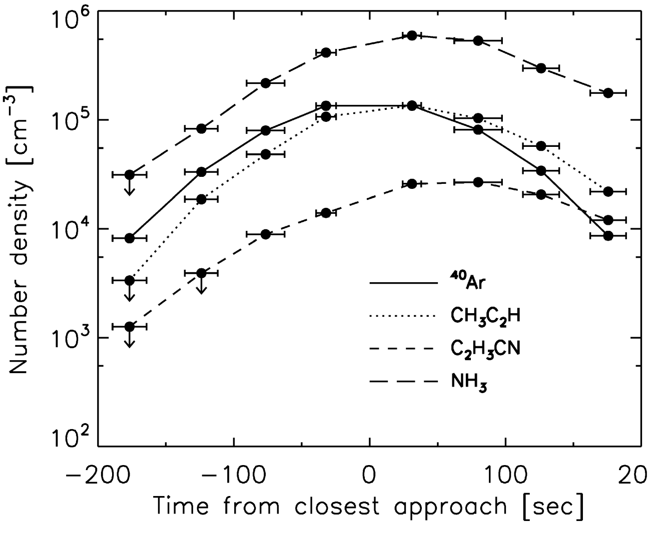

Fig. 7. Density profiles of ^{40}Ar, CH_3C_2H, CH_3CN and NH_3 as a function of time from C/A, obtained by averaging over all flybys. Downward arrows are for upper limit densities. The ^{40}Ar profile serves as a reference which is symmetric about C/A. All other species show density enhancements over the outbound legs, indicating that wall effects are important.

for various species and obtain their true atmospheric densities. Based on photochemical considerations, Vuitton et al. (2008) have shown that the majority of the C_6H_6 molecules recorded by the INMS detector are those formed on the chamber walls through the recombination of C_6H_5 with H. While this study does emphasize the importance of heterogeneous surface chemistry, such a feature cannot be naively generalized to all species since it depends critically on the abundances of the associated radicals in the ambient atmosphere as well as the relevant time constant for the detailed wall chemistry. The example for C_6H_6 may simply be an exception, due to the relatively high C_6H_5 abundances in Titan's upper atmosphere as a result of the large C_6H_6 photolysis rate (Vuitton et al., 2008).

If, for most heavy species, the simple processes of adsorption and desorption are dominant, we expect that the way the measured counts are affected by wall effects depends on the fraction of molecules that are adsorbed to the walls (hereafter adsorption probability, denoted as p_{ads}) and the characteristic time constant for the molecules to spend on the walls before desorption (hereafter desorption time constant, denoted as t_{des}). In the absence of heterogeneous wall chemistry, the atmospheric densities, n_{atm}, chamber densities, n_{ch} and surface densities, σ on the walls of a given species are related through

$$0 = n_{\mathrm{atm}} v_{\mathrm{sc}} A_{\mathrm{x}} - \frac{1}{4} n_{\mathrm{ch}} v_{\mathrm{th}} A_{\mathrm{x}} - S\frac{d\sigma}{dt}, \tag{4}$$

$$\frac{d\sigma}{dt} = \frac{1}{4} n_{\mathrm{ch}} v_{\mathrm{th}} p_{\mathrm{ads}} - \frac{\sigma}{t_{\mathrm{des}}}, \tag{5}$$

where $S = 11\ \mathrm{cm}^2$ is the surface area of the chamber walls, $A_{\mathrm{x}} = 0.22\ \mathrm{cm}^2$ is the size of the entrance aperture, $v_{\mathrm{sc}} = 6\ \mathrm{km\,s^{-1}}$ is the spacecraft velocity, $v_{\mathrm{th}} = \sqrt{\frac{8k_{\mathrm{B}}T}{\pi m}}$ is the thermal velocity of the given species corresponding to a constant wall temperature of 300 K (Waite et al., 2004). Here we adopt a zero ram angle and assume a steady state for the gas in the chamber, but we allow for the accumulation/depletion of gas on the chamber walls with time, i.e., non-zero $d\sigma/dt$. Clearly, in the limit of negligible wall effects (i.e., $p_{\mathrm{ads}} = 0$ and $t_{\mathrm{des}} = \infty$), the above equations reduce to the ideal case of ram pressure enhancement (see Section A.2).

In Eqs. (4) and (5), p_{ads} is assumed to be constant for any given species throughout the mission, and t_{des} is taken to be inversely proportional to the N_2 density in the chamber. This choice of t_{des} is based on the consideration that desorption is likely to be initiated by the bombardment of N_2 molecules on the chamber walls. Model calculations based on Eqs. (4) and (5) show that adopting a constant t_{des} (independent of the N_2 chamber density) produces too many counts on the outbound legs in all realistic cases to match the observations, thus the scheme with a constant t_{des} will not be further discussed in this paper. Since the N_2 densities in the chamber are directly determined from the measurements, we only need to specify the value of t_{des} for a reference N_2 density, chosen as a chamber density of $1 \times 10^{11}\ \mathrm{cm}^{-3}$ throughout our model calculations (corresponding to an ambient N_2 density of $\sim 2 \times 10^9\ \mathrm{cm}^{-3}$). For any heavy species, the value of t_{des} for this reference N_2 density is assumed to be constant for all flybys. This parameter is denoted as $t_{\mathrm{des}}^{(\mathrm{ref})}$ in the rest of the paper, and clearly we have $t_{\mathrm{des}} = t_{\mathrm{des}}^{(\mathrm{ref})}[10^{11}/n_{\mathrm{ch}}(N_2)]$ where $n_{\mathrm{ch}}(N_2)$ is the chamber density of N_2 in units of cm^{-3}.

We solve Eqs. (4) and (5) for the chamber density, n_{ch} and wall surface density, σ for a given species and given flyby, with any combination of p_{ads} and $t_{\mathrm{des}}^{(\mathrm{ref})}$. An initial condition of zero wall surface density at -500 s from C/A is adopted. The density profile of the given species in the ambient atmosphere has also to be specified a priori. Here we assume that the atmospheric density profile of any heavy species follows diffusive equilibrium, i.e., decreases exponentially with its own scale height (with a constant temperature of 151 K in the ambient atmosphere, see Section 4.2.1 below). The remaining free parameter of the atmospheric density at any reference altitude is then constrained by requiring that the peak model profile of n_{ch} matches the observed peak chamber density. Such a procedure is justified by the self-similarity of Eqs. (4) and (5).

In principle, we can compare the model chamber density profiles directly to the INMS observations, and search for the most probable values of p_{ads} and $t_{\mathrm{des}}^{(\mathrm{ref})}$ in a minimum χ^2 sense. Here we adopt a simplified scheme, in which both the observed and calculated chamber densities are parametrized in the same way, and the most probable values of p_{ads} and $t_{\mathrm{des}}^{(\mathrm{ref})}$ are identified by comparing the values of the selected parameters. In more detail, we find that for a given species, the variation of the chamber density with time from C/A can be reasonably fit with a shifted Gaussian distribution, $n_{\mathrm{ch}} \propto \exp[-(t - t_0)^2/\Delta t^2]$, where the time shift, t_0 and time width, Δt are two free parameters in the fitting. Similarly, we use the same empirical form to fit the model chamber density profile. For any combination of p_{ads} and $t_{\mathrm{des}}^{(\mathrm{ref})}$, the model chamber density profiles are calculated separately for different flybys and then averaged over the whole sample. We search for regions in the p_{ads}–$t_{\mathrm{des}}^{(\mathrm{ref})}$ parameter space where t_0 and Δt values roughly overlap between the model and the observations.

An example is given in Fig. 8 for C_4H_2, representing a case for which the values of p_{ads} and $t_{\mathrm{des}}^{(\mathrm{ref})}$ can be reasonably constrained by the data. The upper and lower panels of Fig. 8 show the distribution of t_0 and Δt with respect to p_{ads} and $t_{\mathrm{des}}^{(\mathrm{ref})}$, as calculated from the adsorption/desorption model. Their values are estimated from the INMS data as 42 ± 5 s and 100 ± 8 s, respectively, where the uncertainties quoted above represent standard deviations among different flybys. The dashed lines in Fig. 8 give the region for consistent values of both t_0 and Δt between the model and the observations (within 1σ standard deviation). This region constrains reasonable values of the adsorption probability roughly as $p_{\mathrm{ads}} > 0.15$ and the desorption time constant roughly as $50 < t_{\mathrm{des}}^{(\mathrm{ref})} < 180$ s, where $t_{\mathrm{des}}^{(\mathrm{ref})}$ is for a reference N_2 chamber density of $10^{11}\ \mathrm{cm}^{-3}$.

We show in Fig. 9 the model calculations for the wall effects of C_4H_2 observed during the T29 flyby. The solid lines show the C_4H_2 density profiles in the chamber, calculated from Eqs. (4) and (5). The thick solid line is calculated with an adsorption probability of $p_{\mathrm{ads}} = 0.8$ and a desorption time constant of $t_{\mathrm{des}}^{(\mathrm{ref})} = 150$ s, within the region of the p_{ads}–$t_{\mathrm{des}}^{(\mathrm{ref})}$ parameter space where the model reasonably matches the observed C_4H_2 chamber density profile (indicated by the solid circles). The thin solid line is calculated with $p_{\mathrm{ads}} = 0.05$ and the same desorption time constant, which does not fit the observations very well. The thick and thin dotted lines give the corresponding C_4H_2 density profiles in the ambient atmosphere, which are symmetric about C/A and follow diffusive equilibrium. Clearly, the true atmospheric abundances of C_4H_2 in both cases are significantly higher than the values derived by considering the ram pressure enhancement only (indicated by the open triangles in the figure). This example illustrates the importance of correcting for wall effects, in order to obtain the true atmospheric abundances of some species. On one hand, for the inbound measurements, the true atmospheric densities of C_4H_2 seem to be underestimated by more or less the same factor as compared with the values obtained by assuming ram pressure enhancement only. This indicates that the actual scale height of the given species is more reasonably represented by inbound measurements. On the other hand, Fig. 9 shows that the outbound densities obtained by assuming ram pressure enhancement only are close to the true atmospheric abundances, especially near a time shift

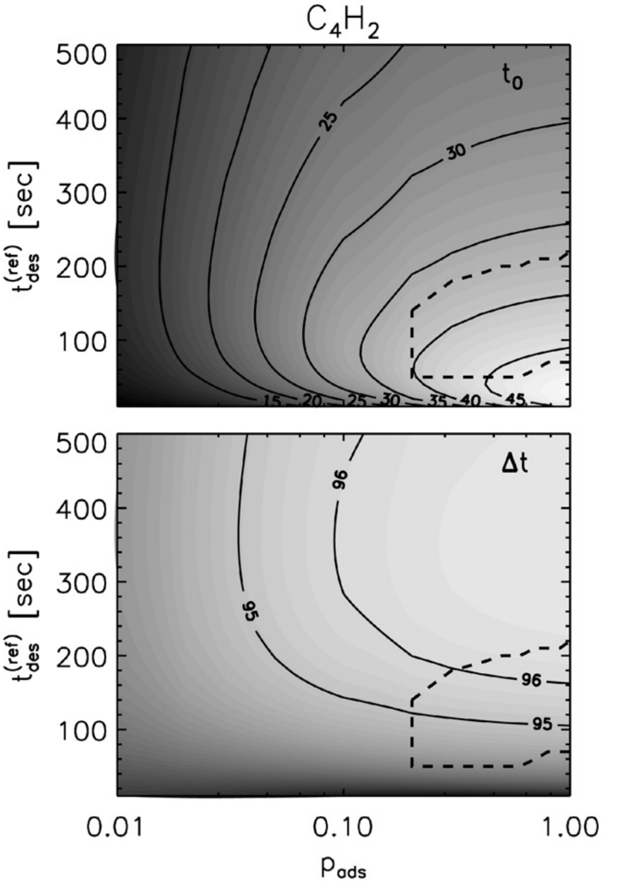

Fig. 8. The distribution of t_0 and Δt in the parameter space of adsorption probability (p_{ads}) and desorption time constant ($t_{des}^{(ref)}$, referred to an N_2 chamber density of 10^{11} cm^{-3}), where t_0 and Δt represent the time shift and width of the shifted Gaussian function used to characterize both the observed and model chamber density profiles of C_4H_2. The dashed lines mark the region where the combination of p_{ads} and $t_{des}^{(ref)}$ provides reasonable fit to the observed C_4H_2 chamber densities, following the simple adsorption/desorption model proposed in the paper.

of about +200 s which is comparable with the desorption time constant adopted in the model calculations. In spite of this, the outbound density profile obtained by assuming ram pressure enhancement does not reflect the true scale height of C_4H_2 in the ambient atmosphere.

The simple adsorption/desorption model presented above reasonably describes the time behavior of several minor species, including C_2H_2/C_2H_4, CH_3C_2H, C_4H_2, C_6H_6, HC_3N and NH_3. We show in Fig. 10 the regions of the p_{ads}–$t_{des}^{(ref)}$ parameter space for C_2H_2/C_2H_4, CH_3C_2H, C_4H_2 and HC_3N where the calculated chamber density profiles reasonably match the observations in terms of the parametrization with a shifted Gaussian, as outlined above. C_6H_6 and NH_3 are not shown in the figure, since heterogeneous surface chemistry on the chamber walls might be of more importance, which will be addressed further below. The values for the adsorption probability and desorption time constant are not well constrained for C_2H_2/C_2H_4 and CH_3C_2H, with a wide range of p_{ads} and $t_{des}^{(ref)}$ values reasonably reproducing the observations. For most other minor species, the simple adsorption/desorption model for wall effects will not be directly applied to the data, since most of the inbound spectra give upper limit densities for these species, and model fits to constrain p_{ads} and $t_{des}^{(ref)}$ are unreliable.

In spite of the difficulty in applying the simple adsorption/desorption model directly to other heavy species, it is interesting to investigate how the realistic instrument response for a given species varies with time from C/A, for various choices of the adsorption probability and desorption time constant. Owing to the self-similarity of Eqs. (4) and (5), such an investigation can be easily performed for all species independent of their actual measurements. An example is shown in Fig. 11 for C_2H_3CN, for which most of the individual INMS spectra give upper limit densities due to the low signal-to-noise ratios of counts in channel 53 (see also Section 3.3). The realistic instrument response functions for all flybys are given as a function of altitude, normalized by the ram pressure enhancement factor assuming zero ram angle. The solid line portion and dotted line portion of each curve in the figure stand for inbound and outbound passes, respectively. The values of p_{ads} and $t_{des}^{(ref)}$ adopted for the calculations are also indicated in the figure. Clearly, the true atmospheric abundances are underestimated for normalized instrument response smaller than unity. Comparisons between different panels of Fig. 11 and the same calculations for other species immediately reveal that

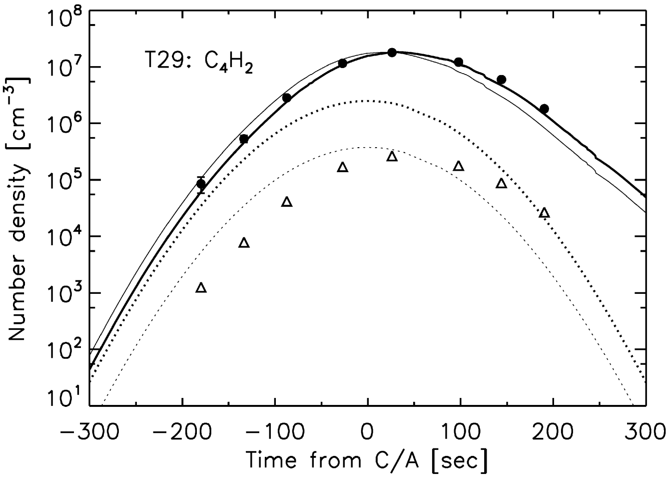

Fig. 9. The simple adsorption/desorption model fitting to the C_4H_2 densities obtained during the T29 flyby, as a function of time from C/A. The solid circles represent the observed C_4H_2 densities in the chamber, and the open triangles the corresponding atmospheric densities calculated with the ram enhancement factor. The solid and dotted lines represent the model density profiles in the INMS chamber and in the ambient atmosphere, respectively. The thick lines are calculated with $p_{ads} = 0.8$ and $t_{des} = 150$ s (referred to an N_2 chamber density of 10^{11} cm^{-3}) and the thin ones with $p_{ads} = 0.05$ and the same desorption time constant.

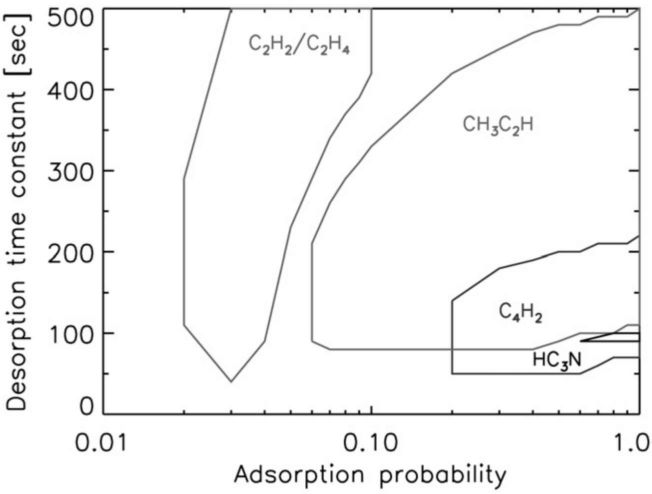

Fig. 10. The regions in the parameter space of adsorption probability and desorption time constant (referred to an N_2 chamber density of 10^{11} cm^{-3}), where the combinations of these two parameters provide reasonable fits to the observed chamber densities, following the simple adsorption/desorption model proposed in the paper. Four species are shown, and for other species, the values of these parameters are not well constrained by the INMS data.

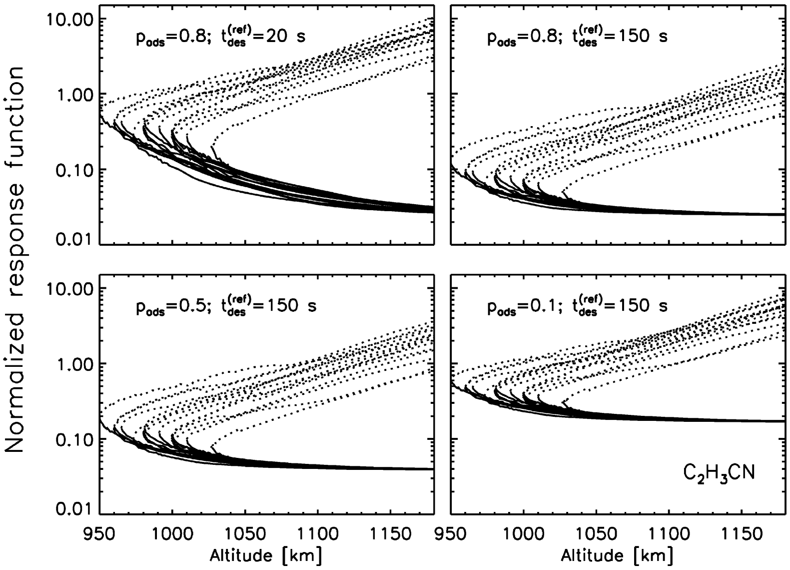

Fig. 11. The realistic instrument response functions calculated for C_2H_3CN for different flybys and normalized by the ideal ram enhancement factor. The solid and dotted line portions of each curve represent the inbound and outbound passes, respectively. Values of the adsorption probability, p_{ads} and the desorption time constant, $t_{des}^{(ref)}$ (referred to an N_2 chamber density of 10^{11} cm^{-3}) used in the model calculations are indicated.

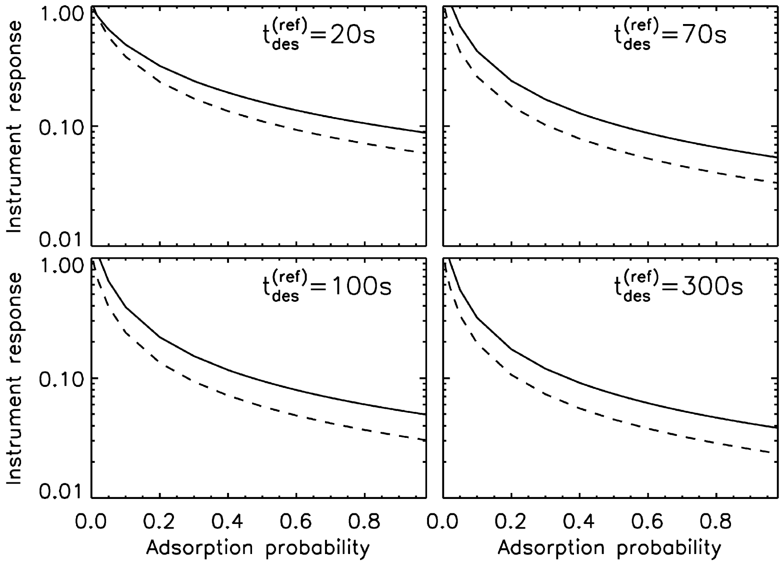

Fig. 12. The instrument response as a function of adsorption probability, for several choices of the desorption time constant (all referred to an N_2 chamber density of 10^{11} cm^{-3}), and averaged over all flybys in the sample. In each panel, the solid and dashed lines represent the instrument response for species with molecular masses of 30 and 80, respectively. This represents the reasonable mass range for all heavy species included in our spectral analysis.

the instrument response for the inbound measurements tends to a fairly constant level above ∼1050 km for all flybys. This feature suggests that the easiest way to obtain the true atmospheric abundances of the heavy species in question is to correct for the wall adsorption/desorption effects based on the inbound measurements obtained not too close to C/A. In such a scheme, the adopted correction factor is expected to be independent of the detailed flyby geometry as indicated in Fig. 11.

We show in Fig. 12 the instrument response as a function of adsorption probability, normalized by the 'ideal' ram enhancement factor and averaged between 1050 and 1200 km over the inbound portions of all flybys. Different panels represent different choices of the desorption time constant, $t_{des}^{(ref)}$ (referred to the N_2 chamber density of 10^{11} cm^{-3}, see above). In each panel, the solid and dashed lines correspond to species with molecular masses of 30 and 80, respectively. This reasonably represents the mass range for most heavy species included in our spectral analysis. From Fig. 12, at the limit of no adsorption ($p_{ads} = 0$), the normalized instrument response is close to unity, i.e., identical to the ram enhancement factor, which is expected since no correction for wall effects is required. At the limit of complete adsorption ($p_{ads} = 1$), the instrument response tends to a constant value which is not sensitive to the molecular mass and the desorption time constant, at least for $t_{des}^{(ref)} > 100$ s. We notice that for any individual flyby, the spacecraft travels through Titan's upper atmosphere from an altitude of 1200 km to C/A with a typical time of ∼200 s. Therefore, with a desorption time constant comparable with or greater than this value, the desorption term in Eq. (5) is not important, and thus the chamber densities are largely controlled by the adsorption probability alone. On the other hand, with a small desorption time constant, incoming molecules adsorbed on the chamber walls get desorbed nearly locally and the instrument response depends on both the adsorption probability and desorption time constant.

Fig. 12 presents a scheme to correct for the wall adsorption/desorption effects for typical heavy species detected by the INMS. The (multiplicative) correction factor can be adopted as the inverse of the normalized instrument response shown in the figure. In the case of complete adsorption ($p_{\rm ads} = 1$) and large desorption time constant ($t_{\rm des} > 100$ s), the normalized instrument response tends to a constant value of $\sim$0.03 roughly independent of molecular mass. This is to say that the densities obtained from the INMS measurements adopting the ram enhancement factor should be divided by the same factor, or equivalent, multiplied by a factor of $\sim$30, in order to get the true atmospheric abundances. We emphasize that the normalized instrument response shown in Fig. 12 should only be applied to inbound measurements away from C/A. At lower altitudes or for outbound measurements, correction for wall adsorption/desorption is more difficult, since Fig. 11 shows that the calculated instrument response function presents a significant scattering from flyby to flyby and is sensitive to both the adsorption probability and desorption time constant.

An inherent assumption in our simple wall effect model presented here is that no heterogeneous surface chemistry is involved. Therefore, even though the adsorption/desorption model is able to provide reasonable fits to the observed chamber density profiles of C_6H_6 as mentioned above, the interpretation of this result deserves some caution, since Vuitton et al. (2008) have shown that a significant fraction of the observed C_6H_6 molecules are those formed through the recombination of C_6H_5 radicals on the chamber walls. This additional chemical source term is not included in the model presented above. The similar process for C_7H_8 has also been discussed in Vuitton et al. (2008). Another species likely to be influenced by wall surface chemistry is NH_3, due to the relatively high abundances of N and H radicals in the ambient atmosphere. In fact, the NH_3 mixing ratios directly obtained from the INMS data in the CSN mode are much higher than those predicted from the measurements of the associated ion species in the OSI mode (Vuitton et al., 2007), even without a correction for wall adsorption/desorption. To reconcile with the OSI results, we suspect that a significant fraction of the NH_3 molecules in the INMS chamber are formed from N and H radicals through surface chemistry. Fortunately, such an effect of surface chemistry may not be important for other minor species, due to the very low abundances of the associated radicals in the ambient atmosphere, as revealed by photochemical model calculations (e.g., Lavvas et al., 2008b). For these species, the simple adsorption/desorption processes are likely to be the dominant aspect of the wall effects, and with a knowledge of their adsorption probability as well as desorption time constant, their true atmospheric abundances can be reasonably obtained with the realistic instrument response as shown in Figs. 11 and 12. We will revisit this issue in Section 4.2.2, in which we present the atmospheric abundances of various minor species with possible effects of wall adsorption/desorption corrected.

To summarize, in the following sections, we will analyze both the inbound and outbound measurements. While the densities derived for N_2, CH_4, H_2 and ^{40}Ar (as well as their isotopes) reflect true values in the ambient atmosphere, the interpretation of the abundances of other minor species deserves caution, since wall effects have been shown as important. How the measured counts reflect the abundances of the local atmosphere relies on the details of the wall effects, which could be either simple adsorption/desorption processes or more complicated heterogeneous surface chemistry on the chamber walls. Due to the peculiar scale heights as shown in Fig. 6, we suggest that the outbound measurements of heavy minor species are not representative of the ambient atmosphere. We choose two schemes for the analysis of heavy species, either based on direct SVD fits to the inbound mass spectra or based on the simple model proposed above to correct for wall adsorption/desorption. The model requires a knowledge of the adsorption probability and desorption time constant, the latter of which is assumed to be inversely proportional to the N_2 density in the chamber. The possible values for these two parameters are obtained for several species in this section (see Fig. 10), which will be treated as a guide to the analysis of other species in Section 4.2.2.

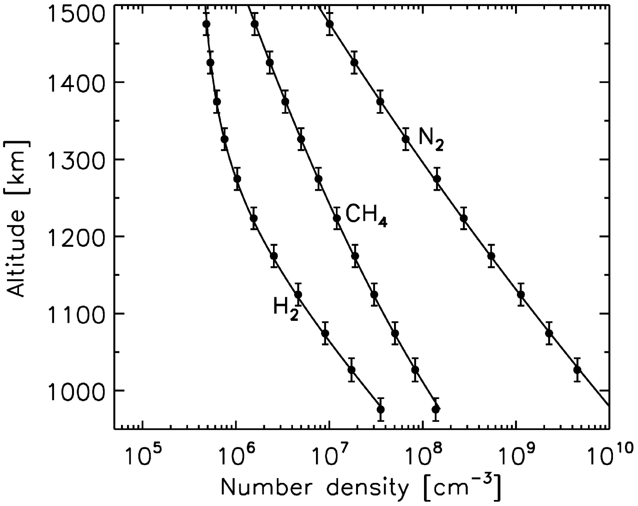

Fig. 13. The globally averaged density profiles of N_2, CH_4 and H_2, below 1500 km. The solid line overplotted on the N_2 observations is the best-fit hydrostatic equilibrium model, with a thermospheric temperature of 151 K. Also shown are the best-fit isothermal diffusion models for CH_4 and H_2, with a most probable escape flux of 2.6×10^9 cm^{-2} s^{-1} (for CH_4) and 1.1×10^{10} cm^{-2} s^{-1} (for H_2), referred to Titan's surface.

4.2. Globally averaged vertical distribution

4.2.1. Nitrogen, methane and hydrogen

The globally averaged density profiles of N_2, CH_4 and H_2 have been presented in some recent papers, based on a smaller INMS sample (Yelle et al., 2006, 2008; Cui et al., 2008). The mixing ratios of these species and their errors are detailed in Table 3 at four representative altitudes, based on the INMS sample adopted in this study. These errors correspond to uncertainties due to counting statistics and sensitivity calibration, not necessarily associated with horizontal and/or diurnal variations. Fig. 13 shows with the solid circles the globally averaged density profiles of these species as a function of altitude, between 950 and 1500 km. These profiles are based on the densities directly determined from their main channels (Müller-Wodarg et al., 2008; Cui et al., 2008). Both inbound and outbound data are included for these species, since the wall effects are negligible as shown in Fig. 5.

As the most abundant atmospheric species on Titan, the density distribution of N_2 directly provides information on the thermospheric temperature, assuming hydrostatic equilibrium. The most recent determination is given by Cui et al. (2008) as 152.5 K, which is also consistent with earlier results from Voyager UVS measurements (Vervack et al., 2004). Based on the N_2 distribution between 950 and 1500 km obtained in this work, we derive a similar average thermospheric temperature of 151.0 ± 1.5 K, and the corresponding hydrostatic equilibrium model is overplotted on the data in Fig. 13. The small change in the temperature value, as compared with that from Cui et al. (2008), is primarily associated with the additional data (T36 and T37) included in this work, as well as an improvement in the calibration of the $C^{(2)}$–$C^{(1)}$ conversion ratios for channel 28 (see Section A.3).

Table 3
Globally averaged total densities and mixing ratios of neutral constituents in Titan's upper atmosphere, obtained directly from the inbound measurements, assuming ram pressure enhancement only. Errors include uncertainties due to both counting statistics and sensitivity calibration.

	Altitude			
	981 km	1025 km	1077 km	1151 km
Density (cm^{-3})	$(1.03 \pm 0.01) \times 10^{10}$	$(4.84 \pm 0.01) \times 10^9$	$(2.27 \pm 0.01) \times 10^9$	$(8.47 \pm 0.01) \times 10^8$
N_2	$(98.4 \pm 0.1)\%$	$(97.8 \pm 0.2)\%$	$(97.4 \pm 0.5)\%$	$(96.6 \pm 0.1)\%$
CH_4	$(1.31 \pm 0.01)\%$	$(1.78 \pm 0.01)\%$	$(2.20 \pm 0.01)\%$	$(3.00 \pm 0.01)\%$
H_2	$(3.30 \pm 0.01) \times 10^{-3}$	$(3.72 \pm 0.01) \times 10^{-3}$	$(3.90 \pm 0.01) \times 10^{-3}$	$(4.28 \pm 0.01)\%$
^{40}Ar	$(1.42 \pm 0.03) \times 10^{-5}$	$(1.25 \pm 0.02) \times 10^{-5}$	$(1.10 \pm 0.03) \times 10^{-5}$	$(7.56 \pm 0.32) \times 10^{-6}$
C_2H_2/C_2H_4	$(1.16 \pm 0.01) \times 10^{-4}$	$(1.26 \pm 0.01) \times 10^{-4}$	$(1.16 \pm 0.01) \times 10^{-4}$	$(9.58 \pm 0.10) \times 10^{-5}$
C_2H_6	$(5.33 \pm 0.16) \times 10^{-5}$	$(4.05 \pm 0.19) \times 10^{-5}$	$(2.68 \pm 0.19) \times 10^{-5}$	$<2.21 \times 10^{-5}$
CH_3C_2H	$(9.93 \pm 0.31) \times 10^{-6}$	$(9.02 \pm 0.22) \times 10^{-6}$	$(6.31 \pm 0.24) \times 10^{-6}$	$<3.62 \times 10^{-6}$
C_3H_8	$<2.68 \times 10^{-6}$	$<1.84 \times 10^{-6}$	$<2.16 \times 10^{-6}$	$<1.90 \times 10^{-6}$
C_4H_2	$(6.98 \pm 0.16) \times 10^{-6}$	$(4.92 \pm 0.10) \times 10^{-6}$	$(2.46 \pm 0.10) \times 10^{-6}$	$<1.58 \times 10^{-6}$
C_4H_6	$<3.10 \times 10^{-7}$	$<2.63 \times 10^{-7}$	$<3.66 \times 10^{-7}$	$<6.99 \times 10^{-7}$
C_6H_6	$(4.39 \pm 0.09) \times 10^{-6}$	$(2.42 \pm 0.05) \times 10^{-6}$	$(8.95 \pm 0.44) \times 10^{-7}$	$<4.12 \times 10^{-7}$
C_7H_8	$<1.13 \times 10^{-7}$	$<8.73 \times 10^{-8}$	$<1.32 \times 10^{-7}$	$<2.23 \times 10^{-7}$
HC_3N	$(1.96 \pm 0.08) \times 10^{-6}$	$(1.43 \pm 0.06) \times 10^{-6}$	$<8.27 \times 10^{-7}$	$<8.46 \times 10^{-7}$
CH_3CN	$(1.42 \pm 0.09) \times 10^{-6}$	$(1.51 \pm 0.08) \times 10^{-6}$	$<1.48 \times 10^{-6}$	$<1.36 \times 10^{-6}$
C_2H_3CN	$<3.97 \times 10^{-7}$	$<4.00 \times 10^{-7}$	$<5.71 \times 10^{-7}$	$<6.77 \times 10^{-7}$
C_2N_2	$(1.51 \pm 0.08) \times 10^{-6}$	$(1.70 \pm 0.07) \times 10^{-6}$	$(1.45 \pm 0.09) \times 10^{-6}$	$<1.16 \times 10^{-6}$
NH_3	$(4.22 \pm 0.18) \times 10^{-5}$	$(3.48 \pm 0.19) \times 10^{-5}$	$(2.99 \pm 0.22) \times 10^{-5}$	$<3.38 \times 10^{-5}$
H_2O	$<8.24 \times 10^{-6}$	$<2.79 \times 10^{-6}$	$<3.42 \times 10^{-6}$	$<3.92 \times 10^{-6}$
CO_2	$<9.91 \times 10^{-7}$	$<5.44 \times 10^{-7}$	$<8.49 \times 10^{-7}$	$<1.36 \times 10^{-6}$

The vertical distribution of CH_4 and H_2 can each be described by the diffusion model,

$$F_i = -(D_i + K)\left(\frac{dn_i}{dr} + \frac{n_i}{T}\frac{dT}{dr}\right) - \left(\frac{D_i}{H_i} + \frac{K}{H_a}\right)n_i, \qquad (6)$$

where n_i and F_i are the number density and flux of species i, D_i is the molecular diffusion coefficient taken from Mason and Marrero (1970) and K the eddy diffusion coefficient, $H_i = (k_B T)/(m_i g)$ is the scale height with $T = 151$ K being the thermospheric temperature (assuming isothermal), k_B the Boltzmann constant, g the local gravity, and m_i the molecular mass of species i, $H_a = (k_B T)/(m_a g)$ is the scale height of the ambient atmosphere, with m_a representing the mean molecular mass. The mean molecular mass is evaluated from the observed densities of all major species (including N_2, CH_4 and H_2) at any given altitude, which decreases monotonically from ~28 amu at 950 km to ~25 amu at 1500 km. We adopt an eddy profile given by Eq. (4) in Yelle et al. (2008). The asymptotic eddy diffusion coefficient, K_∞ is taken as 3×10^7 $cm^2\,s^{-1}$, based on both INMS and GCMS observations of ^{40}Ar (Yelle et al., 2008). The eddy mixing profile adopted in this work, along with the molecular diffusion coefficients for H_2 and CH_4 are shown in Fig. 14. The figure shows that diffusive separation becomes important above a homopause level at ~800–850 km.

The isothermal diffusion model given by Eq. (6) is applied to the globally averaged density profiles of CH_4 and H_2 between 950 and 1500 km. The boundary conditions are adopted from the INMS data as 1.35×10^6 cm^{-3} for CH_4 and 4.70×10^5 cm^{-3} for H_2 at 1500 km. Since we assume isothermal conditions the thermal diffusion term is neglected in Eq. (6). Though the condition of energy continuity may imply modest temperature decrement near the exobase for these two species, such a thermal effect does not have an appreciate influence on the solution to the diffusion equation (Cui et al., 2008).

We solve Eq. (6) with a 4th-order Runge–Kutta algorithm, taking into account the variation of gravity with altitude. The CH_4 and H_2 fluxes referred to Titan's surface are treated as free parameters in the fitting. The most probable flux values are found to be $(2.6 \pm 0.1) \times 10^9$ $cm^{-2}\,s^{-1}$ for CH_4 and $(1.12 \pm 0.01) \times 10^{10}$ $cm^{-2}\,s^{-1}$ for H_2. These flux values are in general consistent with the values given by Yelle et al. (2008) and Cui et al. (2008), with the small differences due to the inclusion of more INMS data and improvement in data calibration. Notice that eddy diffusion is not included in the analysis of H_2 distribution by Cui et al. (2008), which causes some further deviations, but not significant since molecular diffusion dominates at these altitudes well above the homopause. The errors of the best-fit fluxes given above are related to uncertainties in the eddy profile, with a reasonable range of K_∞ values between 2×10^7 $cm^2\,s^{-1}$ and 5×10^7 $cm^2\,s^{-1}$ (Yelle et al., 2008). The diffusion models for CH_4 and H_2, calculated with the best-fit fluxes, are shown by the solid lines in Fig. 13.

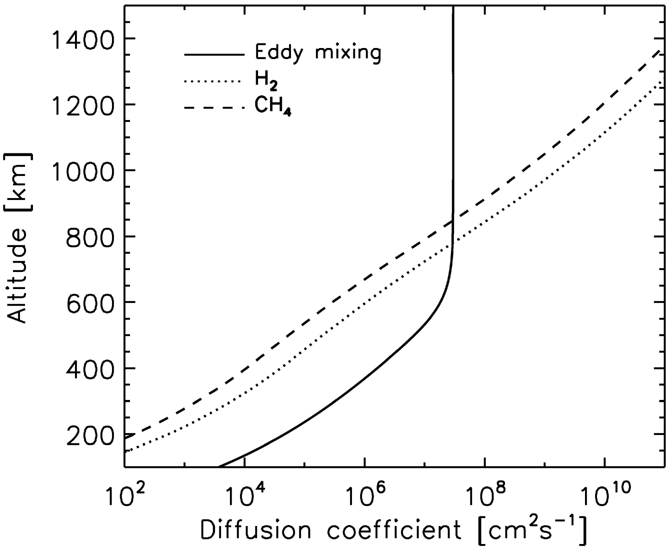

Fig. 14. Diffusion coefficients adopted in this study as a function of altitude below 1500 km. The eddy mixing profile, adopted from Yelle et al. (2008), is given by the solid line. The molecular diffusion coefficients are given by the dotted line (for H_2) and dashed line (for CH_4).

The H_2 escape flux on Titan derived above is higher than the Jeans value of 4.3×10^9 $cm^{-2}\,s^{-1}$ (referred to the surface) by a factor of ~2.7, where the Jeans flux is calculated with a temperature of 151 K and an exobase height of 1500 km. This has been interpreted as thermal evaporation enhanced primarily by an upward conductive heat flux (Cui et al., 2008).

The CH_4 escape flux is more sensitive to the choice of the eddy profile, due to the relatively low molecular diffusion coefficient (see Fig. 14). Yelle et al. (2006) have shown that the CH_4 distribution on Titan observed with INMS can be understood in terms of either a significant escape flux or an eddy diffusion coefficient much higher than the typical values for other planetary systems. However, the eddy profile constrained independently from the INMS/GCMS observations of ^{40}Ar unambiguously shows that interpreting the observed CH_4 distribution on Titan requires a significant escape flux (Yelle et al., 2008). Since the Jeans flux of CH_4 is tiny due to the relatively large CH_4 molecular mass and the low exobase temperature on Titan, non-thermal processes are required to account for the observed CH_4 escape. Further supports on the non-thermal escape of CH_4 come from the exospheric distribution of this species on Titan, which suggests the presence of a suprathermal CH_4 corona (De La Haye et al., 2007a).

4.2.2. Minor species

In this section, we present our analysis of the abundances of heavy species in Titan's upper atmosphere. For these species, the dominant uncertainties are due to the wall effects, which could be either simple adsorption/desorption processes or more complicated heterogeneous surface chemistry on the chamber walls (see Section 4.1). First, we will concentrate on the inbound measurements only, since the density profiles extracted from the outbound data show peculiar scale heights (i.e., comparable with or greater than the N_2 scale height, see Fig. 6), implying serious contamination by the wall effects during the outbound legs. Next, including both the inbound and outbound data, we adopt a simple model to correct for contamination by adsorption/desorption, assuming that no surface chemistry is involved. Such a model has been presented in Section 4.1, and in this section we will emphasize the results. The alternative scheme of wall effects through heterogeneous surface chemistry will not be considered here, since a correction for wall chemistry requires detailed information of the chemical reactions involved as well as an estimate of the abundances of the associated radicals in the ambient atmosphere (Vuitton et al., 2008).

4.2.2.1. Inbound measurements We show in Fig. 15 the globally averaged mixing ratios of various minor species observed in Titan's upper atmosphere, obtained from the inbound measurements with the 'ideal' ram enhancement factor. No attempt has been made to correct for possible wall effects. The upper and lower panels present the distribution of various hydrocarbons and nitrogen-bearing species, respectively, as a function of altitude between 950 and 1200 km. Leftward arrows in the figure indicate 3σ upper limits. Notice that upper limit mixing ratios obtained for the globally averaged distribution of a given minor species do not necessarily mean that all measurements from individual mass spectra are upper limits. In our analysis, upper limits are assigned to all cases in which more than half of the data points are upper limits, since in the statistical sense, the calculated mean value tends to be overestimated for such a sample (Feigelson and Nelson, 1985). The values of the mixing ratios for all minor species included in our spectral analysis are detailed in Table 3, at four representative altitudes. A detailed comparison of the abundances of minor species between this study and previous works will be presented in Section 4.2.3. Here we notice that the typical mixing ratios for trace species given in Table 3 are $\sim 10^{-6}$–10^{-5}. These values approximately correspond to a signal of 10 count per IP or ~ 300 counts s^{-1} for an individual measurement. Adopting a typical sensitivity of 5×10^{-4} counts $(cm^{-3}\,s)^{-1}$ and a typical ram enhancement factor of 70 for heavy species, we get $300/(5 \times 10^{-4})/70 \approx 8 \times 10^3$ cm^{-3} for their typical densities, which correspond to a mixing ratio of $\sim 10^{-6}$–10^{-5} depending on altitude. Typical upper limits of mixing ratio can be as low as 10^{-7}, since integrating over several individual full mass scan helps to reduce the uncertainties caused by counting statistics.

The detection of several species in Titan's thermosphere, including C_2H_2, C_2H_4, HCN and HC_3N, has been reported by Vervack et al. (2004) based on the Voyager UVS solar occultation results. We have firm detections for three of them, except that the crosstalk near channel 28 prevents a reliable measurement of the HCN abundances (see Section A.6).

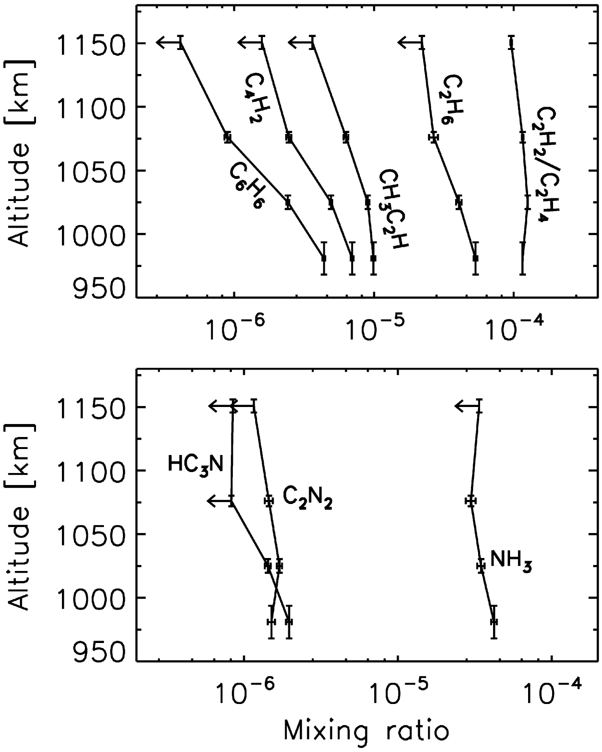

Fig. 15. The globally averaged mixing ratios of various hydrocarbons and nitrogen-bearing species observed in Titan's upper atmosphere, as a function of altitude between 950 and 1200 km. These mixing ratios are obtained by averaging over all inbound measurements, assuming ram pressure enhancement only. Leftward arrows indicate 3σ upper limits.

Most of the minor species presented here have also been detected in Titan's stratosphere based on the recent Cassini/CIRS mid-infrared observations, including C_2H_2, C_2H_4, C_2H_6, CH_3C_2H, C_3H_8, C_4H_2, C_6H_6, HC_3N, C_2N_2 and CO_2 (Coustenis et al., 2007; Teanby et al., 2007a, 2007b). Based on the INMS data, we have firm detections for most of them at much higher altitudes in Titan's thermosphere, except for C_3H_8 and CO_2 on which we are only able to put upper limits. However, as we have emphasized above, upper limit mixing ratios do not necessarily mean that all individual measurements are upper limits. Among all the 69 inbound mass spectra considered in this work, 5 of them show firm detections of CO_2 with a mean mixing ratio of $\sim 1 \times 10^{-6}$. For C_3H_8, no firm detection is obtained for any individual spectrum, due to the low signal-to-noise ratio of counts in channel 43.

The detection of CH_3CN has been reported in the stratosphere from heterodyne ground-based spectroscopy (Bézard et al., 1995), but not revealed by the Cassini/CIRS data (Coustenis et al., 2007). The presence of C_2H_3CN on Titan has not been reported in any previous work, and only upper limit has been put (Marten et al., 2002; Coustenis et al., 2007). Based on the INMS data, CH_3CN is firmly detected below ~ 1050 km, with a mixing ratio of $\sim(1.4$–$1.5) \times 10^{-6}$. C_2H_3CN is not firmly detected in the thermosphere on a global average sense, indicated by upper limits at all altitudes. However, 6 individual inbound spectra give firm detections of C_2H_3CN, and the mean mixing ratio for these firm detections is 6×10^{-7} with a variation of $\sim 60\%$.

No direct observation of NH_3 on Titan has been reported in previously works (in both the thermosphere and stratosphere), though this species was observed in laboratory experiments simulating the condition on this satellite (e.g., Bernard et al., 2003). Although NH_3 is likely to be a component of the spacecraft effluent, the thruster firing contamination may not be important here, since large excursions of signals in channel 17 are not seen, as opposed to what we observe for channel 2 (see Section A.4). Firm detection of NH_3 in a global average sense appears below 1100 km, with a mixing ratio of $\sim(3–4) \times 10^{-5}$. These measurements are much higher than the values predicted in existing photochemical models (e.g., Wilson and Atreya, 2004; Lavvas et al., 2008b). This may indicate missing chemical pathways in previous works. As pointed out by Vuitton et al. (2007), heterogeneous chemistry on the surfaces of aerosol particles might be a solution. However, such an interpretation deserves some caution, since Fig. 7 shows that the distribution of NH_3 along the spacecraft trajectory presents a large time offset, implying significant wall effects for this species. Though we find that the simple adsorption/desorption model presented in Section 4.1 is able to reproduce the observed time behavior of NH_3, we suspect that a full investigation of the NH_3 wall effects requires that surface chemistry be included, due to the relatively high abundances of N and H radicals in Titan's upper atmosphere. This is also motivated by measurements of the associated ion species in the OSI mode (Vuitton et al., 2007).

Finally, for the remaining three species, including C_4H_6, C_7H_8 and H_2O, no firm detection can be made at any given altitude between 950 and 1200 km. Especially, C_4H_6 and C_7H_8 is not detected at 3σ significance level in any individual inbound spectrum, though they are observed in some of the outbound spectra (however, see Vuitton et al., 2008, for a discussion of the wall effects of C_7H_8). For H_2O, 7 individual inbound spectra show firm detections. The H_2O mixing ratios for these firm detections are in the range of $\sim(0.4–3.4) \times 10^{-5}$, with a mean value of 1.2×10^{-5}. For comparison, Coustenis et al. (2003) reported an H_2O mixing ratio of 8×10^{-9} in Titan's stratosphere (near 400 km), based on observations with the Short Wavelength Spectrometer (SWS) onboard the Infrared Space Observatory (ISO). H_2O and CO_2 are the only two oxygen compounds that are included in our spectral analysis. The prediction of these species in photochemical model calculations requires either micrometeorite influx or surficial processes such as volcanic outgassing, and more recently, precipitation of O^+ ions motivated by Cassini Plasma Spectrometer (CAPS) measurements (Hörst et al., 2008, and references therein).

The globally averaged (inbound) density distribution of each of the heavy minor constituents detected in Titan's upper atmosphere can be reasonably described by a power law. Some of these power laws are shown in Fig. 16, which will be used in Section 4.3 to investigate the horizontal/diurnal variations of these species in Titan's thermosphere. The scale heights implied by these power law fittings are sometimes different from the values inferred from diffusive equilibrium. This might be associated with possible wall effects, since the realistic instrument response varies along the spacecraft trajectory. Though Fig. 11 has revealed that the variation of the instrument response is most prominent over the outbound legs, it may still be at a troubling level for inbound measurements, especially those made near C/A.

4.2.2.2. Abundances corrected for adsorption and desorption on the INMS chamber walls In this section, we present the abundances of various minor species in Titan's upper atmosphere, that are corrected for the effects of wall adsorption/desorption. The correction is based on the simple model presented in Section 4.1, which assumes a constant adsorption probability for any given species and a desorption time constant inversely proportional to the N_2 density in the INMS chamber. The correction for C_6H_6, C_7H_8 and NH_3 will not be included here since heterogeneous surface chemistry on the chamber walls is suspected to be of more importance for these species (Vuitton et al., 2008, see also Section 4.1).

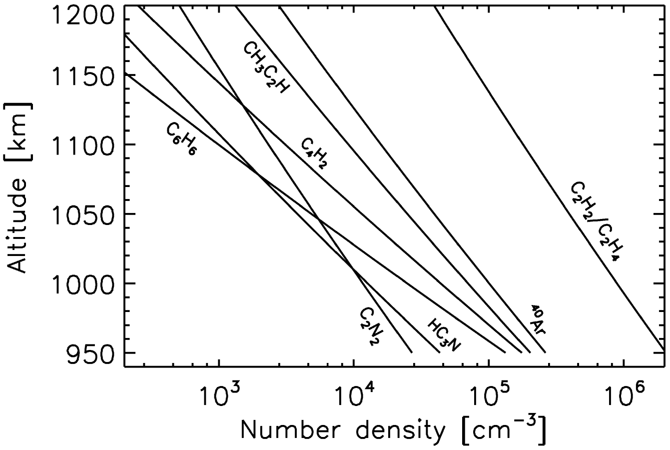

Fig. 16. The power law fitting to the density distribution of various species in Titan's upper atmosphere, obtained by averaging over all inbound measurements and assuming ram pressure enhancement only. These profiles are used to remove vertical dependence of these species before investigating possible horizontal/diurnal variations (see Section 4.3 for details).

Table 4

Globally averaged mixing ratios of various minor species, both directly obtained from the inbound measurements assuming ram pressure enhancement and with possible effects of wall adsorption/desorption corrected. The correction is based on the possible values of adsorption probability and desorption time constant that reasonably reproduce the time behavior of observed chamber densities. All mixing ratios are referred to an altitude of 1077 km or 1025 km, and the values at other altitudes can be obtained with the assumption of diffusive equilibrium.

Species	z (km)	Uncorrected	Corrected	Comment
C_2H_2/C_2H_4	1077	1.2×10^{-4}	$(3.1 \pm 1.1) \times 10^{-4}$	Fig. 10
C_2H_6	1077	2.7×10^{-5}	$(7.3 \pm 2.6) \times 10^{-5}$	Assuming C_2H_2/C_2H_4 values
CH_3C_2H	1077	6.3×10^{-6}	$(1.4 \pm 0.9) \times 10^{-4}$	Fig. 10
C_3H_8	1077	$<2.2 \times 10^{-6}$	$<4.8 \times 10^{-5}$	Assuming CH_3C_2H values
C_4H_2	1077	2.5×10^{-6}	$(6.4 \pm 2.7) \times 10^{-5}$	Fig. 10
C_4H_6	1077	$<3.7 \times 10^{-7}$	$<9.5 \times 10^{-6}$	Assuming C_4H_2 values
CH_3CN	1025	1.5×10^{-6}	$(3.1 \pm 0.7) \times 10^{-5}$	Assuming HC_3N values
C_2H_3CN	1077	$<5.7 \times 10^{-7}$	$<1.8 \times 10^{-5}$	Assuming HC_3N values
HC_3N	1025	1.4×10^{-6}	$(3.2 \pm 0.7) \times 10^{-5}$	Fig. 10
C_2N_2	1077	1.5×10^{-6}	$(4.8 \pm 0.8) \times 10^{-5}$	Assuming HC_3N values

The possible range of adsorption probability and desorption time constant (referred to an N_2 chamber density of 10^{11} cm^{-3}) is shown in Fig. 10 for several species, from which we calculate their true atmospheric abundances with the realistic instrument response function. In practice, we throw random values of p_{ads} and $t_{des}^{(ref)}$ that covers the region drawn in Fig. 10 for the given species. We then calculate the corresponding instrument response functions for different flybys and take averages. We have shown in Section 4.1 that the instrument response function for the inbound measurements not too close to C/A presents the smallest scattering for different flybys and different species (see Fig. 11). Therefore we use the realistic instrument response at 1077 km, averaged over all flybys, to correct for the corresponding inbound measurements at the same altitude listed in Table 3. The corrected mixing ratios are given in Table 4, where the uncertainties represent the standard deviations of all corrected values calculated for different combinations of p_{ads} and $t_{des}^{(ref)}$ (within the corresponding region shown in Fig. 10), as well as different flybys. For other species listed in Table 4, we assume that their possible values of p_{ads} and $t_{des}^{(ref)}$ resemble those of a similar species for which these two parameters are reasonably well constrained by the data. In more detail, we adopt the C_2H_2/C_2H_4 values for C_2H_6, the CH_3C_2H values for C_3H_8, the C_4H_2 values for C_4H_6, and the HC_3N values for all other

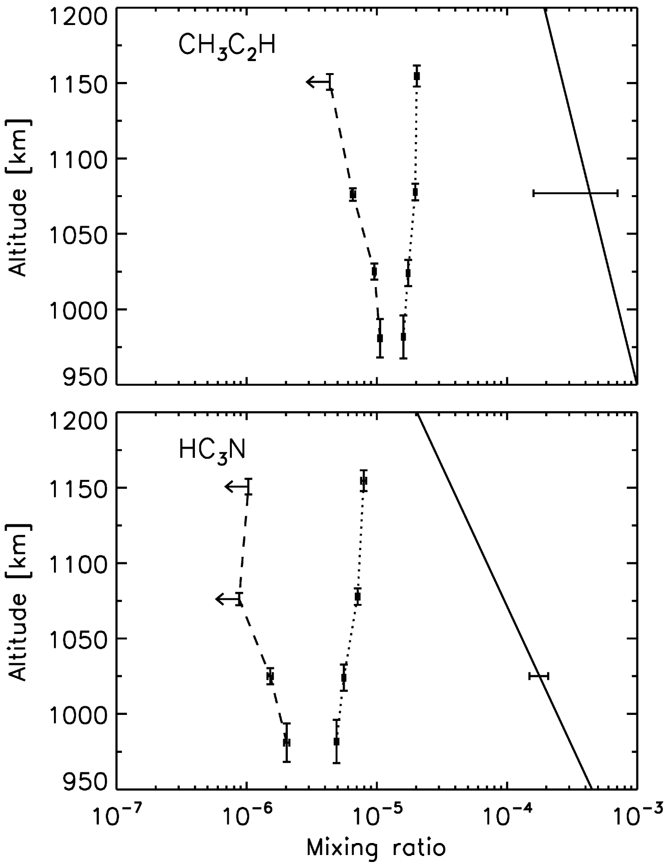

Fig. 17. The globally averaged distribution of CH_3C_2H (upper panel) and HC_3N (lower panel) in Titan's upper atmosphere. The dashed and dotted lines show the mixing ratio profiles averaged over all inbound and outbound measurements (assuming ram pressure enhancement only). The solid lines represent the profiles corrected for adsorption/desorption and satisfying the condition of diffusive equilibrium.

nitrogen-bearing species. For HC_3N and CH_3CN, the corrected mixing ratios are given for an altitude of 1025 km, where an exact determination (rather than an upper limit) is available. Though the instrument response shows a large scattering at this lower altitude, as shown in Fig. 11, the adsorption probability and desorption time constant of nitrogen-bearing species are tightly constrained by the INMS data (see Fig. 10), and as a consequence, the uncertainties of the corrected mixing ratios tend to be small. The wall effect correction for C_2H_2/C_2H_4 is not as prominent as the other species. This is expected as a result of their relatively high abundances on Titan, and the C_2H_2/C_2H_4 molecules in the ambient atmosphere may contribute to a significant fraction of the chamber densities of these species. Finally, since our simple adsorption/desorption model assumes that the atmospheric distribution for any species follows diffusive equilibrium, the mixing ratios for all species listed in Table 4 at other altitudes can be easily obtained from their scale heights.

As two examples, we show in Fig. 17 the distribution of CH_3C_2H and HC_3N in Titan's upper atmosphere, between 950 and 1200 km. The dashed and dotted lines give the inbound and outbound profiles, respectively. The solid lines are calculated from the corrected mixing ratios given in Table 4, assuming diffusive equilibrium. Fig. 17 shows that the true atmospheric abundances are significantly underestimated by both inbound and outbound measurements, when taking into account ram pressure enhancement only. Typically, the inbound values underestimate the atmospheric abundances by a factor of ∼20–30. However, above some altitude level, the outbound counts could be well representative of the atmospheric abundances for some species, as a consequence of the desorption of molecules accumulated on the chamber walls throughout the inbound legs. The behavior of the outbound profile depends critically on the desorption time constant, which may vary significantly for different species.

The above results on the true atmospheric abundances of various minor species in Titan's upper atmosphere are based on a simple model to describe the adsorption/desorption processes on the chamber walls. Such a model might be over-simplified for some species, e.g., C_6H_6, C_7H_8 and NH_3, for which wall surface chemistry is suspected to be of more importance (see Section 4.1). On the other hand, even in cases when the simple model does work, the possible values of the adsorption probability and desorption time constant may not be well constrained by the data (especially CH_3C_2H, see Fig. 10), leading to considerable uncertainties associated with the correction for wall adsorption/desorption. Lab experiments performed with the REU are probably required to figure out the details of the wall effects unambiguously.

4.2.3. Comparison with previous results

In this section, we compare the densities and/or mixing ratios of various neutral species based on our analysis to those given in previous works, including (1) the INMS results given by Waite et al. (2005) based on the TA data; (2) the early results based on the Voyager UVS solar occultation data (Vervack et al., 2004); and (3) the densities of several neutral species predicted from the INMS T5 observations in the OSI mode, based on an ion-neutral chemistry model (Vuitton et al., 2007).

First, we compare our results obtained directly from the inbound measurements (with no correction for possible wall effects) with those of Waite et al. (2005). Based on the INMS data acquired during the first Titan flyby (TA), Waite et al. (2005) estimated the mixing ratios of several minor species with relatively high abundances. The C_2H_2 and C_2H_4 mixing ratios from Waite et al. (2005) are 1.9×10^{-4} and $(2.6\text{–}5.3) \times 10^{-4}$, at an altitude of ∼1200 km. This corresponds to a mixing ratio of $(2.1\text{–}2.7) \times 10^{-4}$ for the *imaginary* species of $\frac{3}{4}n(C_2H_2) + \frac{1}{4}n(C_2H_4)$, about a factor of 2 higher than our value of 1×10^{-4} at a slightly lower altitude of 1150 km averaged over all flybys. Their CH_3C_2H mixing ratio of 3.9×10^{-6} is comparable with our value of 3.6×10^{-6}, which is an upper limit. The differences between these measurements could be accounted for by horizontal and/or diurnal variations (see Section 4.3). Especially, we will present in Section 4.3.1 that meridional variations are tentatively identified in the sense that relatively heavy species such as CH_3C_2H show enhanced mixing ratios at Titan's equatorial region. This is qualitatively consistent with the differences between the two works, since the TA trajectory covers low latitude regions near Titan's equator, while our results represent globally averaged measurements. The C_2H_6 mixing ratio given by Waite et al. (2005) is 1.2×10^{-4} at ∼1200 km, while our SVD analysis puts an upper limit of 2×10^{-5} at ∼1150 km. Such a considerable difference is likely due to the neglect of $^{15}N^{15}N$ in the early analysis of the INMS data. For all the other minor species, Waite et al. (2005) declares upper limit mixing ratios of 5 ppm, consistent with our determinations. Therefore, both analyses, though based on completely different methods, reach consistent results on the abundances of most minor species detected in Titan's upper atmosphere. It should also be mentioned that the above comparison is based on densities uncorrected for any possible wall effect. In the case when processes such as adsorption/desorption are important, both results may significantly underestimate the true atmospheric abundances of some heavy species.

Previous results about the abundances of various neutral species in Titan's thermosphere have also been obtained from the Voyager UVS solar occultation observations (Smith et al., 1982; Vervack et al., 2004). The early analysis of Smith et al. (1982) only

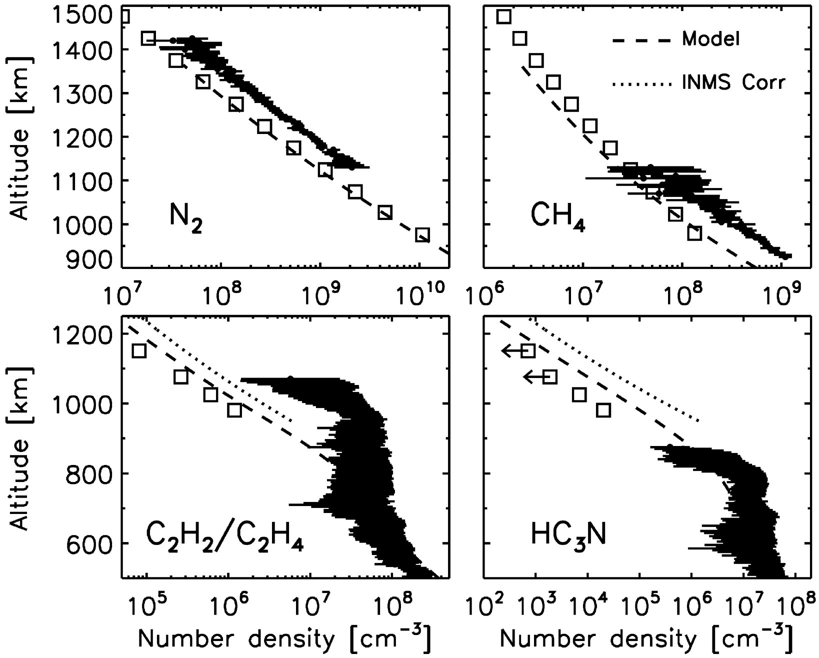

Fig. 18. Comparison between Cassini/INMS and Voyager/UVS results of the distribution of neutral species in Titan's thermosphere. The open squares represent globally averaged mixing ratios from this work, combining data from 15 Titan flybys. These values are obtained by assuming ram pressure enhancement only. The mixing ratio profiles for C_2H_2/C_2H_4 and HC_3N which are corrected for wall adsorption/desorption are shown by the dotted lines. The UVS results from Vervack et al. (2004) are given by the solid circles with large horizontal error bars. Photochemical model calculations from Lavvas et al. (2008b) are shown with the dashed lines.

included N_2, CH_4 and C_2H_2, and their results were unable to match the UVS observations of Titan's dayglow emission (Strobel and Shemansky, 1982). More accurate re-analysis has been performed by Vervack et al. (2004), including density determination of N_2, CH_4, C_2H_2, C_2H_4, HCN, and HC_3N. The INMS data are complementary to the early Voyager UVS observations: (1) The INMS samples a relatively higher altitude range in Titan's thermosphere; (2) The UVS and INMS data characterize conditions with high and low solar activities, respectively; (3) These data have different sources of uncertainty, in the sense that the interpretation of the UVS data is subject to blending between different atmospheric constituents in UV absorption, whereas the interpretation of the INMS data requires separation of the overlapping patterns in electron impact dissociative ionization.

Here we compare the INMS abundances of these species with the ingress results of Vervack et al. (2004), except for HCN which is not constrained by the INMS data due to crosstalk near channel 28 (see Section A.6). The egress results of Vervack et al. (2004) are less reliable, due to the uncertainties in the solar reference spectra as well as a larger altitude range subtended by the projection of the Sun (Vervack et al., 2004). The UVS density profiles for N_2, CH_4, C_2H_2/C_2H_4 and HC_3N are shown in Fig. 18, represented by the solid circles with large horizontal error bars. The INMS profiles are given by the open squares, obtained by averaging over all flybys and including inbound data only (assuming ram pressure enhancement). The leftward arrows indicate upper limits. For C_2H_2/C_2H_4 and HC_3N, we also show with the dotted lines their profiles corrected for wall adsorption/desorption. The dashed lines in Fig. 18 are adopted from the photochemical model calculations of Lavvas et al. (2008b), where we have scaled their total densities by a constant factor of 0.67 to match the INMS values. The UVS N_2 densities are about a factor of 2 higher than the INMS values, for overlapping altitude regions. Such a difference can be either due to uncertainties in absolute calibration or due to the long-term variations in Titan's upper atmosphere since the two missions cover a time span of over 20 years. The N_2 scale heights from both works are nearly identical, therefore giving similar values of thermospheric temperature (see Section 4.2.1). The CH_4 mixing ratios obtained from the UVS data are about 25% higher than the INMS values. Such a deviation cannot be due to different solar conditions, since the low solar activities appropriate for our INMS sample should lead to higher CH_4 mixing ratios as a result of smaller CH_4 photolysis rate. The difference in the C_2H_2/C_2H_4 mixing ratios is considerably larger. Compared with the direct inbound measurements (uncorrected for wall effects), the UVS values are higher by a factor of 20 and 13 at 980 km and 1025 km, respectively. Qualitatively, variations in solar activities may partly account for these differences, since a large CH_4 photolysis rate results in more efficient production of hydrocarbon molecules. Wall effects seem not strong enough to produce such a large difference, as indicated by the dotted line in the figure. Finally, no direct comparison can be made for HC_3N, since the altitude range probed by both instruments do not overlap. It is also worth mentioning that the UVS densities of this species were obtained with the contribution from HCN ignored, therefore the UVS profile of HC_3N represents the limiting case with largest densities allowed by the data (Vervack et al., 2004).

Based on the INMS T5 data obtained in the OSI mode, Vuitton et al. (2007) derived the densities of various ion species in Titan's upper atmosphere, from which they were able to estimate the densities of the related neutral species. These results, which rely on the details of the presumed ion-neutral chemistry model, can be compared with direct INMS measurements in the CSN mode. Such a comparison is detailed in Table 5, giving the INMS CSN densities obtained from direct SVD fits to both the inbound and outbound T5 spectra. The mixing ratios corrected for wall adsorption/desorption are based on the realistic instrument response function calculated specifically for T5. All mixing ratios listed in the table are for ~1100 km, and most of the inbound CSN values are upper limits. We notice that the neutral abundances predicted by Vuitton et al. (2007) are systematically higher than direct inbound measurements in the CSN mode, by one order of magnitude (for C_4H_2) or two orders of magnitude (for HC_3N and C_2H_3CN). For most species, the mixing ratios obtained from the outbound measurements are

Table 5
Comparisons between the INMS mixing ratios obtained directly from the CSN mode and the values predicted from the ion abundances measured in the OSI mode. The OSI values are adopted from Vuitton et al. (2007) based on the INMS T5 measurements. The CSN values for both the inbound and outbound T5 measurements are given, along with the values corrected for wall adsorption/desorption. All mixing ratios are given for a reference altitude of ∼1100 km.

Species	CSN			OSI
	Inbound	Outbound	Corrected	
C_4H_2	$<8.1 \times 10^{-7}$	$(4.5 \pm 0.5) \times 10^{-6}$	$(2.7 \pm 1.4) \times 10^{-5}$	1×10^{-5}
CH_3CN	$<1.3 \times 10^{-6}$	$(4.1 \pm 0.6) \times 10^{-6}$	$(2.8 \pm 0.5) \times 10^{-5}$	3×10^{-6}
C_2H_3CN	$<4.4 \times 10^{-7}$	$(1.5 \pm 0.4) \times 10^{-6}$	$(8.5 \pm 1.5) \times 10^{-6}$	1×10^{-5}
HC_3N	$<4.7 \times 10^{-7}$	$(1.7 \pm 0.4) \times 10^{-6}$	$(1.0 \pm 0.2) \times 10^{-5}$	4×10^{-5}

still lower by a significant amount. However, when corrected for possible effects of adsorption/desorption, the results from both works are consistent. The only exception is CH_3CN, and such a deviation between CNS and OSI results is probably related to missing reactions in the ion-neutral chemistry model adopted by Vuitton et al. (2007), for this particular species. Alternatively, it may also imply that processes other than simple adsorption/desorption are important. In spite of this, Table 5 does show a general agreement between neutral abundances predicted from OSI measurements and those corrected for wall effects in the CSN mode. The above discussion also suggests the possibility of correcting for wall effects based on a comparison between the INMS data obtained in the CSN and OSI modes. The INMS measurements in the OSI mode are not contaminated by wall effects, and the associated ion-neutral chemistry network is better understood compared with either the adsorption/desorption or the heterogeneous surface chemistry on the chamber walls.

4.3. Horizontal and diurnal variations

In this section, we investigate the neutral gas distribution with latitude, longitude and local solar time, aimed at identifying possible horizontal and/or diurnal variations in Titan's upper atmosphere.

Calculations based on the solar-driven Thermospheric Global Circulation Model (TGCM) have already inferred meridional and zonal winds in Titan's thermosphere, with speeds of ∼20–50 $m\,s^{-1}$ (Müller-Wodarg et al., 2000, 2003; Müller-Wodarg and Yelle, 2002). Such a wind field is accompanied with both horizontal and diurnal variations of the atmospheric composition on Titan (Müller-Wodarg et al., 2003). Especially, the predicted accumulation of light species such as CH_4 near Titan's polar regions gets observational support from the INMS data (Müller-Wodarg et al., 2008). The thermospheric dynamics on Titan may also be driven by its interactions with Saturn's magnetosphere (termed as auroral-driven throughout this paper), which could deposit significant energy in Titan's upper atmosphere through electron/ion precipitation with a pattern that depends primarily on longitude rather than local solar time. In analogy to the solar-driven TGCM model, the interactions with the Saturn's magnetosphere may cause extra heating over limited ranges of longitude, drive large scale horizontal wind field, and induce redistribution of neutral gas in the thermosphere. The detailed picture of the interactions between Titan's atmosphere and Saturn's magnetosphere is still not well understood at this stage. The realistic configuration of the magnetic field in the vicinity of Titan may cause the energy deposit from precipitating electrons to deviate significantly from the ideal ramside (e.g., Backes et al., 2005). For ions such as O^+, N^+ and CH_4^+, this is further complicated by the fact that their trajectories may not follow along the magnetic field lines as a result of the finite gyroradius effect (e.g., Luhmann, 1996; Ledvina et al., 2000; Brecht et al., 2000).

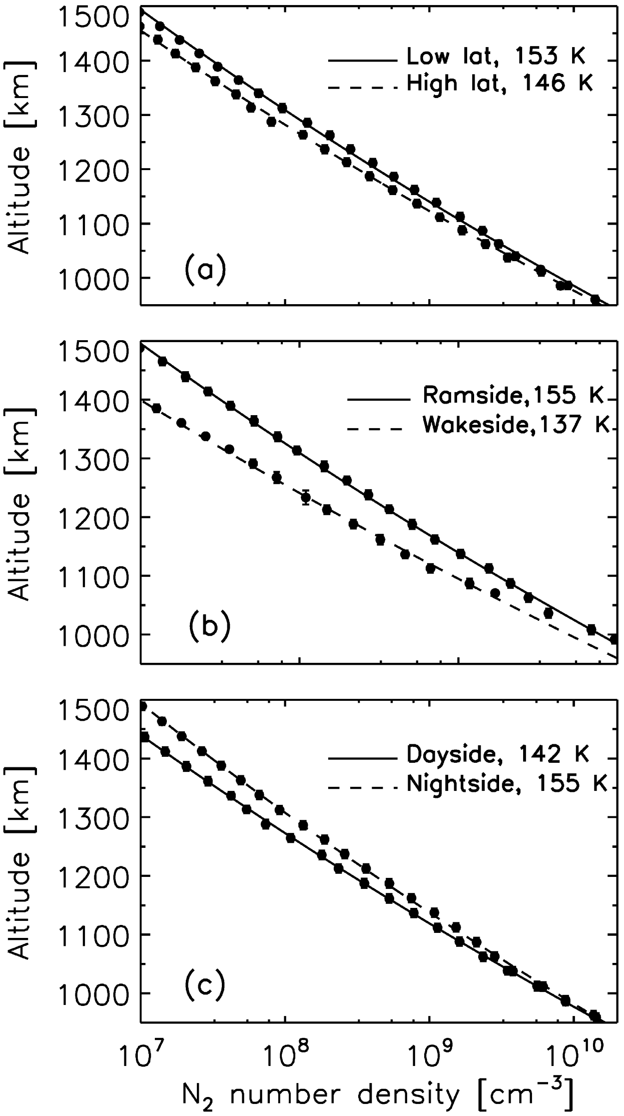

Fig. 19. The barometric model fitting of the N_2 density distribution in Titan's upper atmosphere. Panel (a) shows the model fitting for the equatorial region and north polar region; panel (b) presents the N_2 distribution for the ideal magnetospheric ramside and wakeside; and panel (c) shows the average N_2 density profiles for the dayside and nightside. The figure implies that the equatorial region, ideal magnetospheric ramside, and nightside hemisphere of Titan are relatively warmer.

As the dominant atmospheric constituent, the N_2 distribution provides information on the thermal structure in Titan's upper atmosphere, as described in Section 4.2.1. Early studies based on the Voyager UVS data have tentatively suggested that the morning terminator of Titan is slightly warmer than the evening terminator, though this result is not statistically significant due to the large uncertainties in temperature (Smith et al., 1982). More recently, horizontal/diurnal variations in temperature identified from the INMS data were presented in De La Haye et al. (2007a) and Müller-Wodarg et al. (2008). In this work, we investigate this problem further by dividing all density measurements of N_2 into several bins with different values of latitude, longitude as well as local solar time, and adopt the simple barometric model to estimate the corresponding temperature in each bin. Some of the N_2 model profiles are shown in Fig. 19. The details will be covered in the following sections. As a summary, we list all the derived temperature values in Table 6.

To investigate the horizontal/diurnal variations of neutral gas distribution on Titan, the simplest scheme is to divide all measure-

Table 6

Thermospheric temperatures of Titan. ϕ, θ and t stand for latitude, longitude and local solar time, respectively. All temperatures are determined from the barometric fitting of the observed N_2 profiles averaged over the selected ranges of latitude, longitude or solar local time.

Bin definition	Temperature (K)
Global average	151.0 ± 1.5
Low latitude, $0^\circ < \phi < 30^\circ$	153.4 ± 1.4
Mid latitude, $30^\circ < \phi < 60^\circ$	151.2 ± 1.5
High latitude, $60^\circ < \phi < 90^\circ$	146.4 ± 1.5
Facing-Saturn side, $\theta < 45^\circ$ or $\theta > 315^\circ$	152.8 ± 1.5
Anti-Saturn side, $135^\circ < \theta < 225^\circ$	137.5 ± 1.4
Magnetospheric ramside, $225^\circ < \theta < 315^\circ$	154.7 ± 1.4
Magnetospheric wakeside, $45^\circ < \theta < 135^\circ$	137.0 ± 1.6
Dayside, 6 h $< t <$ 18 h	142.1 ± 1.4
Nightside, $t <$ 6 h or $t >$ 18 h	154.8 ± 1.5

ments for a given species into several bins with different ranges of latitude, longitude or local solar time. Comparisons between the average density profiles in these bins provide direct information on the horizontal/diurnal variations of the species under consideration. For CH_4 and H_2, such a procedure is easily implemented, since the sampling of their densities, derived from the counts in their main channels, covers a large altitude range (from 950 to 1500 km) and a high spatial resolution ($\sim$5.5 km) compared with most of the minor species (see also Fig. 1). This is also true for the N_2 distribution, used to infer the thermospheric temperature on Titan as described above. On the other hand, the density determination of most minor species relies on the SVD fits to the integrated mass spectra over certain altitude ranges below 1200 km. These species are sparsely sampled, making it difficult to investigate their horizontal/diurnal variations with the procedure adopted for CH_4 and H_2. Here we use a more complicated procedure in which we correct for vertical variations by scaling all measurements of minor species to a common altitude level of 1050 km. Such a scaling is based on the simple power law fits shown in Fig. 16. The objective of such a procedure is to include as many individual measurements as possible, to enhance the statistical significance of our conclusions. However, the disadvantage is that the procedure introduces additional uncertainties inherent in the adopted model profiles for scaling.

To investigate the horizontal/diurnal variations of CH_4 and H_2, comparisons should be made between density profiles as a function of pressure rather than altitude. This is aimed at removing possible effects of asymmetric atmospheric shape. Observational evidences for an asymmetric thermosphere on Titan have been reported by Müller-Wodarg et al. (2008). Based on an INMS sample similar to the one adopted here, they found a pronounced oblateness in Titan's thermosphere, with isobaric surfaces being $\sim$45 km higher over the equator than at the north pole. Throughout this section, to examine the horizontal/diurnal variations of CH_4 and H_2, we calculate pressure values from the ideal gas law with the measured total densities and a constant thermospheric temperature of 151 K (see Section 4.2.1). Though Titan's upper atmosphere is not strictly isothermal, the temperature variation of order $\sim$5% (see below and Fig. 19) is too small to have any appreciable influence. For an investigation of the horizontal/diurnal variations of heavy species, we will not attempt to correct for possible atmospheric oblateness directly. In stead, we estimate a posteriori how significant the observed variations can be biased by this effect.

In Section 4.2.1, we use the diffusion model to describe the density distribution of CH_4 and H_2. Though this is a valid procedure in a global average sense, it is not justified to apply the same model to the CH_4 and H_2 profiles obtained by averaging over a limited range of latitude, longitude and local solar time. This is because diffusion is coupled with the global circulation pattern in Titan's upper atmosphere which presents both horizontal and vertical wind components (Müller-Wodarg et al., 2008). Such a wind is probably canceled out in a global average sense, but not over limited ranges of latitude, longitude and local solar time. On the other hand, the vertical component of the wind speed may not be negligible compared with the diffusion velocities of both CH_4 and H_2, as inferred from their best-fit fluxes given in Section 4.2.1. Therefore to investigate quantitatively the horizontal/diurnal variations of CH_4 and H_2 diffusion/escape, the full three-dimensional kinetic model should be adopted.

In this section, we present our analysis of the variations of temperature and CH_4/H_2 mixing ratio with latitude (Section 4.3.1), longitude (Section 4.3.2) and local solar time (Section 4.3.3), followed by the horizontal/diurnal variations of heavy species (Section 4.3.4). Finally, we conclude with an assessment of the observed variations in Section 4.3.5.

4.3.1. *Meridional variations*

The meridional variation of the N_2 distribution can be used to infer the horizontal thermal structure in Titan's upper atmosphere. This has been investigated by Müller-Wodarg et al. (2008) based on their empirical model of Titan's thermosphere, constructed from an INMS sample smaller than the one adopted here. In their work, a two-dimensional temperature field was derived by integrating the hydrostatic equation downward at each latitude and then calculating temperature from the ideal gas law (see also Müller-Wodarg et al., 2006). Such a temperature field is characterized by a warmer equatorial region and a cooler north polar region, consistent with predictions of solar heating models (Müller-Wodarg et al., 2008). Here, we divide the INMS sample into three latitude bins, at 0°–30° N, 30°–60° N and 60°–90° N, respectively. We use the simple barometric relation to fit the average N_2 distribution in each bin, and the best-fit thermospheric temperature decreases from 153.4 ± 1.4 K for the low latitude bin, to 151.2 ± 1.5 K for the mid latitude bin, and to 146.4 ± 1.4 K for the high latitude bin. Therefore both works, though based on different procedures of deriving temperature, reach a consistent result that the equatorial region in Titan's thermosphere appears to be warmer and the north polar region is cooler, with a temperature difference between the equator and north pole of $\sim$10 K. The model profiles of N_2 for the low and high latitude bins are shown in Fig. 19a.

Similarly, we investigate the CH_4 and H_2 density profiles averaged over the latitude bins defined above. Differences between these profiles are clearly seen in Fig. 20. The CH_4 distribution shows accumulation near the north polar region and depletion near the equatorial region, supporting the possible trend identified by Müller-Wodarg et al. (2008). The difference in the observed CH_4 mixing ratios between the equatorial and polar regions is about 25% at a pressure level of $\sim 1.7 \times 10^{-7}$ dynes cm^{-2} (or near Titan's exobase). The observed meridional variation of CH_4 has been interpreted as a result of upwelling motion near the equator and downwelling motion near the north pole, in response to the horizontal transport by thermospheric winds (Müller-Wodarg and Yelle, 2002; Müller-Wodarg et al., 2003). Meridional variation is also observed for H_2, as shown in the lower panel of Fig. 20. However, the observed H_2 mixing ratio peaks at mid latitudes, and decreases toward both the equator and north pole. Near the exobase, the average H_2 mixing ratio for the mid latitude bin is about 20% higher than the polar value and 60% higher than the equatorial value. Such a feature is likely to be associated with the rapid thermal escape and large ballistic flow of H_2 in Titan's exosphere, since escape tends to enhance depletion near the equator but counteract accumulation near the north pole. As mentioned above, a thorough investigation of this issue requires a three-dimensional modeling of the global circulation pattern in Titan's thermosphere that also includes the effect of escape.

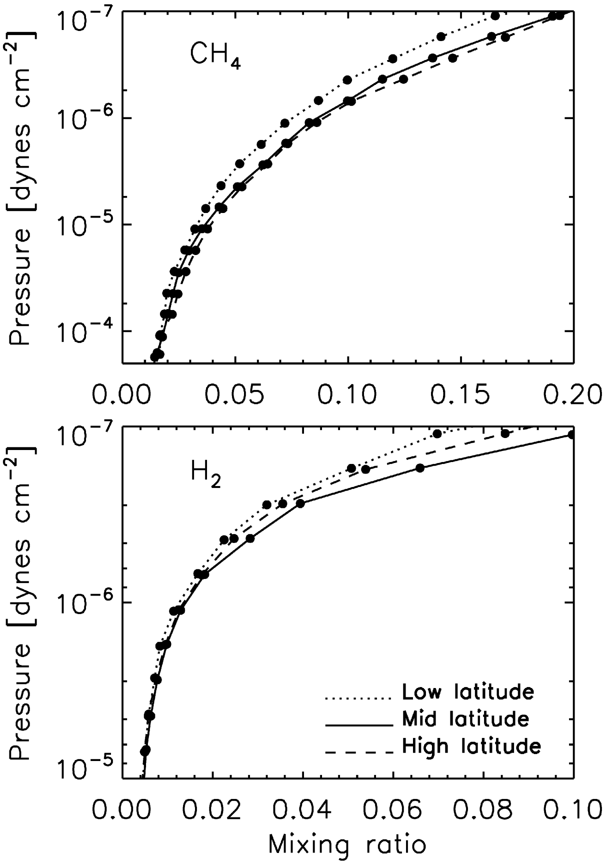

Fig. 20. The average profiles of CH_4 and H_2 mixing ratios in Titan's upper atmosphere for three latitude bins, defined as 0°–30° N for the low latitude bin, 30° N–60° N for the mid latitude bin and 60° N–90° N for the high latitude bin. The figure shows depletion of CH_4 near the equator and accumulation of CH_4 near the north pole. The meridional variation of H_2 shows a more complicated pattern, with enhanced abundances at mid latitudes.

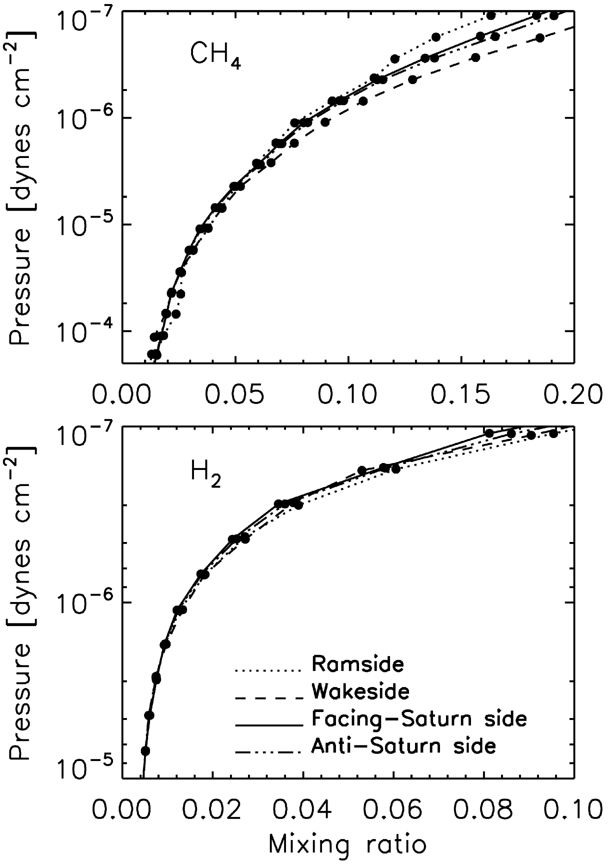

Fig. 21. The average profiles of CH_4 and H_2 mixing ratios in Titan's upper atmosphere for four longitude sectors, referred to as the magnetospheric ramside and wakeside, as well as the facing-Saturn side and anti-Saturn side of Titan, each spanning a longitude range of 90°. The zonal variation of CH_4 suggests depletion at Titan's ramside and accumulation at the wakeside. The zonal variation of H_2 shows a more complex pattern.

From Fig. 20, the magnitude of meridional variations of both CH_4 and H_2 decreases at low altitudes or high pressure levels. Especially, no variation with latitude appears to be present for H_2 below $\sim 2 \times 10^{-6}$ dynes cm^{-2} (at ~1300 km). On the contrary, the meridional variation of CH_4 is observable down to 1×10^{-4} dynes cm^{-2} (at ~1030 km).

The meridional variations presented above are obtained from the neutral gas distribution over Titan's northern hemisphere, where the majority of the INMS measurements adopted in this work were made. Without constraints from measurements in the southern hemisphere, symmetry is usually assumed about Titan's equator (e.g., Müller-Wodarg et al., 2008). Although our INMS sample contains two flybys (T36 and T37) that probe Titan's southern hemisphere, the sample coverage is still too limited to allow robust conclusions to be made with regards to the differences between Titan's northern and southern hemispheres. A thorough investigation of this issue can be attempted with the release of the data to be obtained in the extended Cassini mission.

4.3.2. *Zonal variations*

We first investigate possible zonal variation of the thermospheric temperature by considering the N_2 distribution averaged in different longitude bins. Here, we consider four longitude sectors, one for $\theta < 45°$ or $\theta > 315°$ (facing-Saturn side), one for $135° < \theta < 225°$ (anti-Saturn side), one for $225° < \theta < 315°$ (ideal magnetospheric ramside), and one for $45° < \theta < 135°$ (ideal magnetospheric wakeside). The most probable thermospheric temperatures obtained from barometric fitting in these bins are 152.8 ± 1.5 K (for the facing-Saturn side), 137.5 ± 1.4 K (for the anti-Saturn side), 137.0 ± 1.6 K (for the wakeside) and 154.7 ± 1.4 K (for the ramside), respectively. These values are also listed in Table 6, and the model fits (for the ideal ramside and wakeside) are shown in Fig. 19b. The above results imply that the magnetospheric ramside and facing-Saturn side of Titan appear to be warmer than the wakeside and anti-Saturn side. This may imply extra heating of Titan's upper atmosphere through precipitation of energetic electrons/ions preferentially over the ramside and facing-Saturn side. However, Titan's wakeside is poorly sampled, with measurements below ~1050 km not available as shown in Fig. 19b. Therefore the interpretation of a cooler wakeside on Titan deserves some caution (see also Section 4.3.5 below).

Next we investigate the zonal variations of the CH_4 and H_2 distribution, using their abundances obtained directly from counts in the main channels between 950 and 1500 km. Only measurements made over the northern hemisphere are included, to avoid possible asymmetry about the equator (see above). The CH_4 profiles averaged over the four longitude sectors defined above are shown in the upper panel of Fig. 21. From the figure, CH_4 appears to be depleted at the ramside, but accumulated at the wakeside. Such a trend is clearly seen above 1×10^{-6} dynes cm^{-2} (at ~1350 km). Along with the variation of temperature with longitude described above, the observed zonal variation of CH_4 distribution can be accommodated with the scenario of auroral-driven thermospheric dynamics, in which light species always present depletion in warmer regions (ramside) and accumulation in cooler regions (wakeside).

As shown in the lower panel of Fig. 21, significant zonal variation is also observed for H_2, suggesting accumulation at both the ramside and wakeside. Clearly, the zonal variations of CH_4 and H_2 do not show a similar pattern. Analogous to the observed meridional variation of H_2, it is likely that both escape and large ballistic flows in the exosphere have significant effects, leading to more complicated horizontal structures for H_2 (both meridional and zonal). All H_2 profiles in the lower panel of Fig. 21 appear to be identical below $\sim 2 \times 10^{-6}$ dynes cm^{-2} (at ∼1300 km). The meridional variation of the same species becomes absent at about the same level (see Fig. 20).

4.3.3. *Diurnal variations*

In this section, we investigate possible diurnal variations of thermal structure and gas distribution in Titan's upper atmosphere. Based on the INMS data acquired during the TA, TB and T5 flybys, De La Haye et al. (2007a) found a thermospheric temperature of ∼5 K higher at night than at dusk on Titan, in contrast to the early UVS results (e.g., Smith et al., 1982). Here we extend the analysis to a much larger INMS sample. We divide all N_2 density measurements into two sectors, one for the dayside and the other one for the nightside. The barometric fitting of the N_2 density profiles, averaged over all flybys but constrained within the two selected sectors, are shown in Fig. 19c. For the dayside N_2 distribution, we obtain a best-fit temperature of 142.1 ± 1.4 K, while for the nightside, we get 154.8 ± 1.5 K. With significantly improved statistics, our analysis confirms the result of De La Haye et al. (2007a) that Titan's sunlit side presents a lower thermospheric temperature. Such a trend is clearly in opposite to the predictions of any solar-driven model.

We further examine the diurnal variations of CH_4 and H_2 distribution in Titan's upper atmosphere. Solar-driven TGCM models predict horizontal thermospheric winds of ∼20–50 m s^{-1} (Müller-Wodarg et al., 2008). Since the associated dynamical time constant (of order 10^5 s) is much shorter than the photochemical time constants of CH_4 and H_2, the horizontal wind field may produce accumulation of these light species on Titan's nightside. On the other hand, if the horizontal winds are primarily driven by the precipitating electrons/ions from Saturn's magnetosphere, such a feature may be absent.

The CH_4 and H_2 density profiles averaged over the dayside and nightside hemispheres are shown in Fig. 22. Clear diurnal variations are seen, with both species depleted at the nightside and accumulated at the dayside. Such a feature can be accommodated with the temperature difference between the dayside and nightside hemispheres described above, in the sense that the warmer side is always associated with depletion of light species, and the cooler side associated with accumulation. However, the diurnal variations observed for these species are contradictory to the predictions of solar-driven models. We will return to this issue in Section 4.3.5.

4.3.4. *Horizontal/diurnal variations of heavy species*

In Section 4.2.2, we present our analysis of the abundances of various hydrocarbons, nitrogen-bearing species and oxygen compounds in Titan's upper atmosphere, both in terms of the direct inbound measurements adopting the 'ideal' ram enhancement factor and in terms of the corrected values taking into account the processes of adsorption/desorption on the chamber walls. In this section, we describe our investigation of the horizontal/diurnal variations of these minor species, based on the values directly obtained from the inbound measurements. A similar investigation based on the values corrected for wall effects will not be discussed here, since the values of the adsorption probability and desorption time constant are not well constrained in this study (see Fig. 10), and thus the uncertainties of the corrected abundances are large. In fact, we find that for some combination of the adsorption probability and desorption time constant, significant horizontal/diurnal variations are present for the corrected abundances of several species, while the same feature becomes absent for other choices of p_{ads} and $t_{\mathrm{des}}^{(\mathrm{ref})}$. In spite of this difficulty, we will present in Section 4.3.5 a qualitative assessment of the observed variations of heavy species, taking into account possible wall effects.

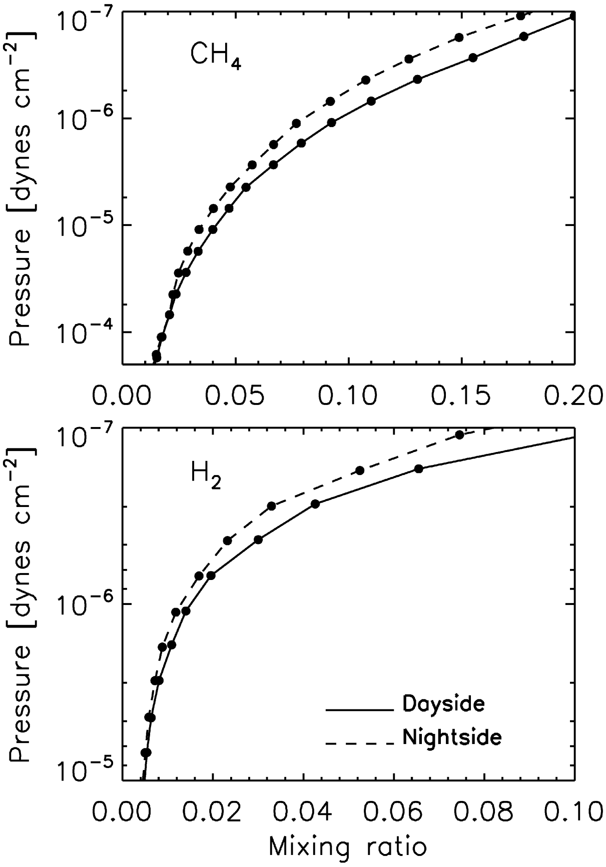

Fig. 22. The average profiles of CH_4 and H_2 mixing ratios for Titan's dayside and nightside hemispheres. For both species, depletion over the nightside and accumulation over the dayside are observed.

Based on the direct inbound measurements, the meridional variations of several representative minor species are shown in Fig. 23, including ^{40}Ar, C_2H_2/C_2H_4, C_4H_2, C_6H_6, HC_3N and CH_3C_2H. Downward arrows indicate 3σ upper limit measurements. Here the analysis is restricted to the northern hemisphere, due to the incomplete latitude coverage in the southern hemisphere. All measurements have been scaled to a common altitude of 1050 km based on the simple power law fitting shown in Fig. 16. These scaled mixing ratios are shown by the open circles in Fig. 23. For comparison, direct INMS measurements based on SVD fits between 1025 and 1075 km are overplotted with the solid circles. In general, the meridional variations of these minor species show some degree of depletion at high latitudes. Such a trend is most prominent for C_2H_2/C_2H_4, C_4H_2 and CH_3C_2H, less evident for HC_3N and C_6H_6, but becomes absent for ^{40}Ar. Except for C_2H_2/C_2H_4, all species shown in Fig. 23 are heavier than N_2, and have smaller scale heights. Therefore, the observed meridional variations are consistent with the prediction of subsidence near polar regions driven by horizontal wind field in Titan's thermosphere.

More quantitatively, we calculate the rank order correlation coefficients for each heavy species, based on the model independent Kendall's-τ test (Press et al., 1992). The correlation coefficients be-

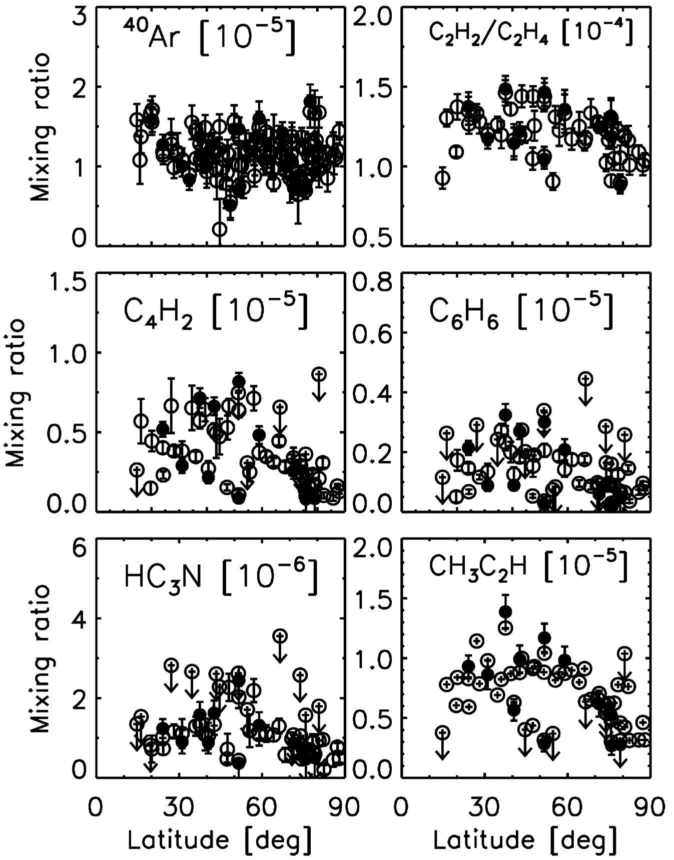

Fig. 23. The meridional variations of several representative minor species in Titan's upper atmosphere. All measurements have been scaled to a common altitude of 1050 km. These scaled mixing ratios are given by the open circles. For comparison, the solid circles represent the directly measured mixing ratios between 1025 and 1075 km based on SVD fits. Downward arrows indicate 3σ upper limit measurements. All species, expect for ^{40}Ar, show some signature of depletion near the north polar region (at more than 2σ significance level, see Table 7). The mixing ratios presented in the figure are obtained by assuming ram pressure enhancement only.

Table 7

Kendall's-τ correlation coefficients. The numbers in the parenthesis are the significance levels of the Kendall's-τ correlation coefficients that deviate from a null hypothesis. The correlation coefficients are calculated between mixing ratio and latitude (ϕ) in the northern hemisphere (meridional), between mixing ratio and longitude (θ) relative to the sub-Saturn direction or the ideal ram direction, and between mixing ratio and local solar time (t) relative to 12 h (diurnal).

Species	Meridional	Zonal		Diurnal
	ϕ	$\lvert\theta\rvert$	$\lvert\theta - 270°\rvert$	$\lvert t-12\rvert$
C_2H_2/C_2H_4	−0.33 (3.4)	−0.15 (1.3)	+0.07 (0.2)	+0.01 (0.2)
CH_3C_2H	−0.36 (3.4)	−0.40 (3.3)	−0.20 (0.5)	−0.04 (0.5)
C_4H_2	−0.43 (4.0)	−0.43 (3.5)	+0.33 (0.7)	−0.03 (0.4)
C_6H_6	−0.26 (2.1)	−0.50 (3.5)	+0.00 (0.0)	−0.12 (1.2)
HC_3N	−0.31 (2.5)	−0.54 (3.9)	+1.00 (1.6)	−0.09 (0.8)
C_2N_2	−0.22 (1.9)	−0.42 (3.2)	+0.60 (1.5)	−0.11 (1.1)
^{40}Ar	−0.08 (1.2)	−0.02 (0.2)	+0.12 (0.6)	+0.10 (1.7)

tween absolute latitude and mixing ratio are listed in Table 7, along with the significance levels of their deviations from zero, representing null hypothesis. Upper limits are not included in evaluating the correlation coefficients. From Table 7, except for ^{40}Ar, all species show some trend of anti-correlation with latitude, at more than 2σ significance level. For C_2H_2/C_2H_4, C_4H_2 and CH_3C_2H, the significance level of the observed anti-correlation is more than 3σ. As mentioned above, such a behavior is consistent with the prediction of subsidence near polar regions by solar-driven TGCM models (Müller-Wodarg et al., 2008).

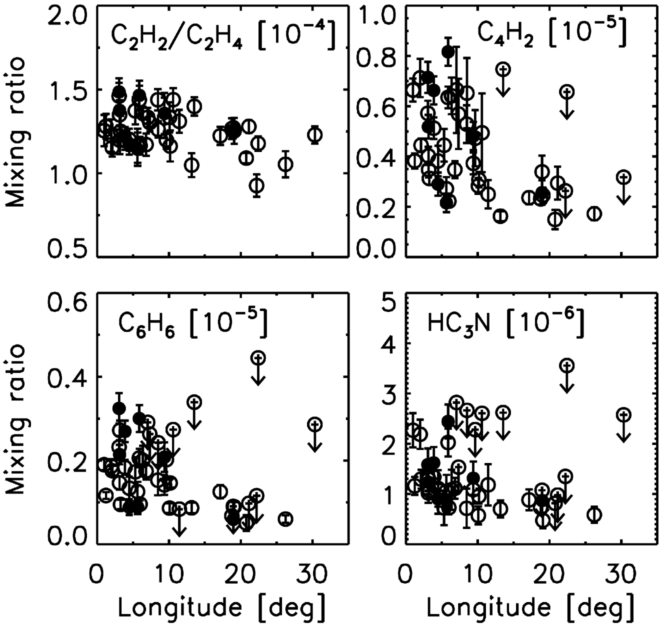

Fig. 24. The zonal variations of several heavy species in Titan's upper atmosphere. Drawing conventions are the same as Fig. 23. These species show a trend of accumulation toward the sub-Saturn direction. However, such a feature is likely to be an observational bias caused by wall effects (see Section 4.3.5 for details).

Next we investigate the zonal variations of heavy species. In analogy to the observed zonal variations of CH_4 distribution (see Section 4.3.2), the auroral-driven thermospheric dynamics on Titan may also induce accumulation/depletion of heavy species over limited ranges of longitude. Two possibilities are explored here, assuming that energy deposit through precipitating ions/electrons primarily take place at the facing-Saturn side or magnetospheric ramside of Titan. These two choices are suggested by the observed zonal variations of thermospheric temperature as well as CH_4 distribution. For the first case, we perform Kendall's-τ tests between the derived mixing ratios and zonal angles relative to the sub-Saturn direction. The corresponding correlation coefficients are listed in the 3rd column of Table 7, which shows that most heavy species (except for ^{40}Ar and C_2H_2/C_2H_4) show some trend of accumulation near the sub-Saturn direction, at more than 3σ significance level. For the second case, we calculate the correlation coefficients between mixing ratios and zonal angles relative to the ideal magnetospheric ram direction. These coefficients are given in the 4th column of Table 7, suggesting no zonal variation for all heavy species.

According to the above analysis, significant zonal variations for the distribution of heavy species are presented in terms of a trend of accumulation toward the sub-Saturn direction, except for ^{40}Ar and C_2H_2/C_2H_4. This feature is shown in Fig. 24 for several representative species (restricted to regions with longitudes, $\theta < 35°$), with all mixing ratios scaled to a common altitude level of 1050 km. At the face value, accumulation of heavy species toward the sub-Saturn direction can be accommodated with the scenario of auroral-driven dynamics in Titan's upper atmosphere with precipitation of energetic electrons/ions primarily on the facing-Saturn side of Titan. However, such a conclusion deserves some skepticism, since the observed zonal variations of heavy species primarily rely on data obtained near the facing-Saturn side, as shown in Fig. 1. Constraining the analysis to inbound measurements further reduces the sample size, covering mostly the longitude range between 0° and 35°. For heavy species, very few measurements are available on either the anti-Saturn side or the magnetospheric ramside and wakeside, making it difficult to justify the observed trend over a larger scale. In fact, what is most surprising is that the zonal variations of heavy species are present over such a small longitude range that covers only ∼10% of the entire surface of Titan. However, we will show in Section 4.3.5 that these observed zonal variations are likely to be observational biases due to wall effects.

Finally, we perform Kendall's-τ test for possible diurnal variations of heavy species. The corresponding correlation coefficients are given in Table 7, calculated between the mixing ratio and $|t-12|$ where t is the local solar time in hour. No significant correlation or anti-correlation is found for any species.

4.3.5. *Reliability check of the observed horizontal/diurnal variations*

In the previous sections, we discuss possible horizontal and diurnal variations of the thermal structure and neutral gas distribution in Titan's upper atmosphere above 950 km. However, the sample distribution with respect to latitude, longitude and local solar time may not be independent. This may introduce observational biases to the analysis of horizontal/diurnal variations, which have to be examined carefully when interpreting the data. For example, in the case when daytime measurements also preferentially select measurements made over the magnetospheric ramside, then in principle we cannot distinguish between the solar-driven model and the auroral-driven model (assuming precipitation of energetic ions/electrons is primarily on the ramside).

The observed horizontal/diurnal variations of heavy species are subject to some additional uncertainties. First, in our analysis, we scale their local densities with the simple power laws (see Fig. 16). Such a procedure introduces additional uncertainties into the observed variations, associated with the deviation of the true distribution from the power law. Second, strictly speaking, the power-law scaling to a common altitude of 1050 km rather than a common pressure level implicitly assumes that Titan's thermosphere is spherically symmetric. However, such an assumption may not be valid (Müller-Wodarg et al., 2008) and the observed horizontal variations of heavy species might be contaminated by the actual atmospheric shape. Finally, as mentioned above, though it is difficult to investigate the variations of heavy species based on the abundances corrected for wall adsorption/desorption (since the parameters, p_{ads} and $t_{\mathrm{des}}^{(\mathrm{ref})}$, are usually not well constrained), the possible contamination of the observed variations by wall effects has to be assessed at least in a qualitative sense.

4.3.5.1. Variations of heavy species In this section, we investigate whether the observed horizontal/diurnal variations of heavy species are reliable. These variations can be summarized as depletion near the north polar region and accumulation toward the sub-Saturn direction, but no apparent correlation with local solar time. The density determination for these species relies exclusively on the SVD analysis of inbound data, and only measurements below 1200 km are considered.

In terms of the meridional variations of heavy species, the effect of thermospheric oblateness (Müller-Wodarg et al., 2008) is a major concern. Qualitatively, the isobaric surfaces near the equator are higher, implying an overestimate of the abundances of heavy species at low latitudes, since we scale all measurements to the same altitude rather than a common pressure level when discussing the horizontal/diurnal variations (see above). Fig. 15 shows that the mixing ratio of the *imaginary* species, $\frac{3}{4}n(C_2H_2)+\frac{1}{4}n(C_2H_4)$, remains roughly constant between 950 and 1200 km, due to the fact that its scale height is close to the N_2 scale height. Therefore, the observed C_2H_2/C_2H_4 depletion near the north pole may not be significantly affected by the atmospheric shape. In the other extreme case, C_6H_6 presents the strongest altitude dependence in Fig. 15. The C_6H_6 scale height is roughly 30 km based on the power law fitting shown in Fig. 16, and the scale height of the background atmosphere is ∼64 km. These give a difference of ∼55% in the C_6H_6 mixing ratio over a vertical extent of 45 km, corresponding to the altitude difference along the isobar between the equator and north pole (Müller-Wodarg et al., 2008). From Fig. 23, the C_6H_6 mixing ratio at the north pole also appears to be depleted by ∼50%, compared with the measurements made near the equator. Therefore, the effect of thermospheric oblateness might be strong enough to offset the observed meridional variation of C_6H_6. Similar calculations performed for other species give a mixing ratio difference of 3% for C_2H_2/C_2H_4, 21% for CH_3C_2H, 40% for C_4H_2 and 33% for HC_3N, over a vertical extent of 45 km. By comparing with Fig. 23, the depletion of these heavy species near Titan's north pole may not be strongly affected by the atmospheric shape. It should be born in mind that the above analysis assumes an altitude difference of 45 km along the isobar between the equator and north pole (Müller-Wodarg et al., 2008). Whether or not the observed meridional variation can be counteracted by the effect of atmospheric oblateness is sensitive to the choice of this value, especially for those species with strong altitude dependence. Considering this, we have more confidence with the observed depletion of C_2H_2/C_2H_4 near Titan's north pole, of which the mixing ratios do not strongly vary with altitude.

Next, we check for possible biases caused by wall effects. We find that longitude is correlated with time from C/A at 7.5σ significance level, estimated from the Kendall's-τ test. This implies that measurements made near the sub-Saturn direction also concentrate near C/A when the contamination by wall effects becomes more serious. This can be easily seen from Fig. 11, which shows that along the inbound portion of the spacecraft trajectory, the realistic instrument response increases toward the 'ideal' ram enhancement factor near C/A. This also implies that the mixing ratios obtained from direct SVD fits to the inbound mass spectra near C/A are closer to the true atmospheric values, compared with those obtained away from C/A. We have shown in Section 4.3.4 that the mixing ratios of heavy species tend to increase toward the sub-Saturn direction, which according to the analysis here, might simply be an observational bias caused by wall adsorption/desorption. The fact that zonal variations are not observed for the distributions of ^{40}Ar and C_2H_2/C_2H_4 further supports this point, since wall effect is not involved for the former (see Fig. 5) and not as pronounced as the other minor species for the latter (see Fig. 6). The same argument may not hold for the meridional variations of heavy species, since the spacecraft approaches Titan from a wide range of latitude covering the whole northern hemisphere and part of the southern hemisphere, with the sample distribution in latitude independent of time from C/A.

Finally, the simple power law fitting shown in Fig. 16 contributes to additional uncertainties in the observed horizontal/diurnal variations of heavy species. Based on the scattering of the globally averaged densities around the best-fit power relation, we estimate for each heavy species the uncertainty associated with the simple power law fitting, characterized by a mean fractional variation. The largest uncertainty appears for C_4H_2, with a factional variation of 59%. We examine 5000 random realizations, each adopting a power law profile randomly fluctuated by 59% on average around the best-fit relation shown in Fig. 16. These random power laws are used to scale the observed C_4H_2 mixing ratios to a common altitude of 1050 km. We then perform Kendall's-τ test on these random samples, to investigate possible meridional variation of C_4H_2. We find that the mean significance level of the 5000 random realizations is 2.3 ± 0.8, with roughly 67% of the C_4H_2 random samples showing evidences of meridional variation at more than 2σ level and only 19% at more than 3σ level. This indicates that the uncertainty inherent in the adopted power law for scaling tend to weaken the observed meridional variation of C_4H_2. By applying such an analysis to all heavy species, we find that our conclusions on the meridional variations of heavy species are likely to be contaminated significantly by the uncertainties associated with the simple power law fitting. However, the meridional variations of most heavy species are still discernible at more than 2σ significance level.

To summarize, we suggest that for heavy species, their depletion near the north polar region and accumulation near the equatorial region are likely to be realistic features, though not significant due to the uncertainties associated with the adopted power law scaling. Possible atmospheric oblateness seems not strong enough to offset the observed meridional variations of most heavy species. On the other hand, realistic zonal and diurnal variations are not observed for these species, with the apparent accumulation near the sub-Saturn direction revealed by the INMS data likely to be an observational bias due to wall effects.

4.3.5.2. Variations of light species and temperature We further check the reliability of the horizontal/diurnal variations of the distribution of light species as well as temperature, presented in Sections 4.3.1–4.3.3. Here the contamination by atmospheric shape is not a concern for the observed CH_4 and H_2 variations, since throughout our analysis, we investigate their profiles as a function of pressure rather than altitude. Also, no model dependent scaling is applied to these light species, indicating that the additional uncertainties associated with scatterings from the average vertical profile is not a worry either. Along with the insignificance of wall effects for these abundant species, the potential source of uncertainty comes from selective sampling with respect to latitude, longitude and local solar time. For the variations of light species, we will concentrate on CH_4 only, since we have mentioned above that the variations of H_2 present a more complex pattern, probably due to the rapid thermal escape as well as large ballistic flow in Titan's exosphere for this species.

First, we notice that the dayside hemisphere also preferentially selects high latitude measurements with a distribution peaking at ~75° N, as shown in the upper panel of Fig. 25. This indicates that the observed diurnal temperature variation, represented by a warmer nightside on Titan, may simply be a side-effect of the meridional variation due to biased samplings of the dayside and nightside hemispheres. Similarly, the observed diurnal variation of CH_4, as shown in Fig. 22, might be explained by the same argument, since the dayside hemisphere where enhanced mixing ratios are observed for CH_4 is coincident with high latitude regions where accumulation of light species is expected.

We also find that the latitude distribution in different longitude sectors are not exactly identical, as shown in the lower panel of Fig. 25. The ideal magnetospheric wakeside of Titan significantly overlap with high latitude regions. This implies that the lower thermospheric temperature, as well as CH_4 accumulation, obtained for this region may simply reflect an observational bias due to the fact that Titan's polar regions are cooler.

The above analysis is based on an inherent assumption that the meridional variations of temperature and CH_4 distribution presented in Section 4.3.1 are real physical features (e.g., Müller-Wodarg et al., 2008). In principle, we may also accommodate the observed variations into an alternative scenario in which Titan's wakeside is cooler. With such an assumption, the lower temperature obtained near the north pole turns out to be an observational bias due to restricted sampling. A third possibility is that a cooler dayside in Titan's thermosphere is a real feature (though may not be physically motivated), and the observations of both cooler polar regions and cooler wakeside are observational biases.

The analysis of the horizontal/diurnal variations presented here is aimed at identifying whether the thermal structure and gas distribution in Titan's upper atmosphere is driven by solar EUV photons or by precipitating ion/electrons from Saturn's magnetosphere. As we have mentioned above, the former suggests a pattern that varies with both local solar time and latitude, while the latter suggests a pattern that may vary with longitude. While our analysis does suggest tentatively that Titan's ramside appears to be warmer with some signature of CH_4 depletion, a solid assessment of the importance of auroral-driven energetics and dynamics in Titan's upper atmosphere requires a full investigation that reconciles all the observed horizontal/diurnal variations.

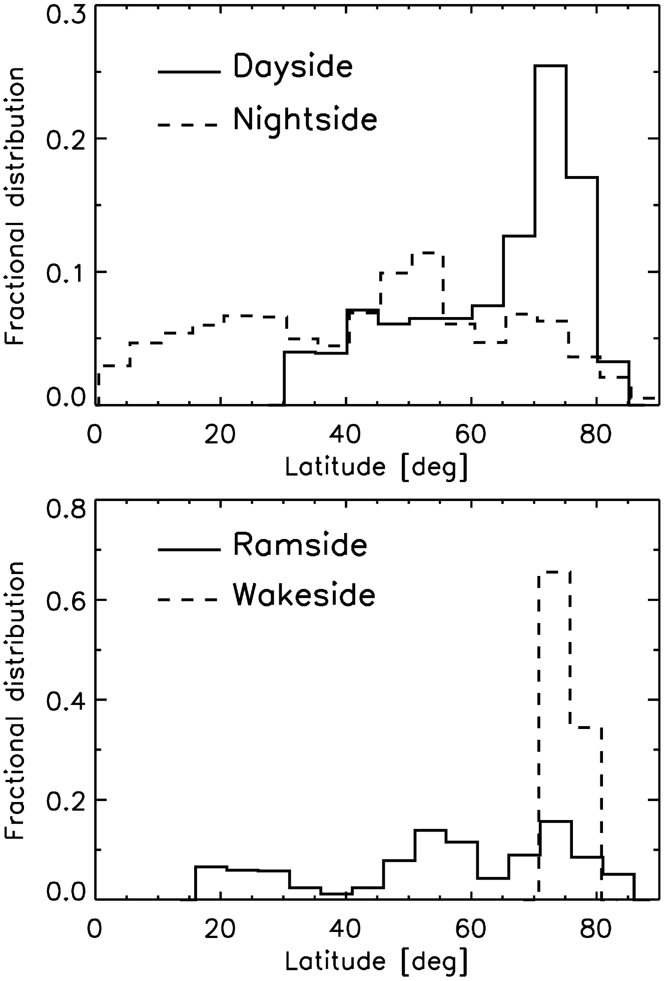

Fig. 25. Upper panel: A comparison between the latitude distributions for Titan's dayside and nightside hemispheres. The dayside subsample preferentially selects measurements made in high latitude regions. Lower panel: A comparison between the latitude distributions for Titan's ramside and wakeside. The wakeside subsample is strongly biased toward high latitude regions.

To disentangle the couplings between different models, the key might be additional information on Titan's thermosphere obtained near the equator and simultaneously on the wakeside. Such a dataset does exist, though in Titan's southern hemisphere: Below 1500 km, the T37 flyby covers Titan's low latitude regions near 20° S, over Titan's wakeside, as well as during the daytime. The barometric fitting of the N_2 densities obtained from the T37 data gives a very low temperature of 135.6 ± 1.4 K, consistent with auroral-driven models but contradictory to the solar-driven models. However, as emphasized by Müller-Wodarg et al. (2008), the observed density profile from any individual flyby may be significantly biased by variations along the spacecraft trajectory. This is further complicated by the fact that Titan's thermosphere may not be symmetric about the equator. At the present time, the restricted sampling of the available INMS data does not allow a firm conclusion on the realistic horizontal/diurnal variations to be made.

5. Concluding remarks

In this paper, we present an in-depth study of the neutral gas distribution in Titan's thermosphere above 950 km, combining the INMS data in the CSN mode acquired during 15 Titan flybys. The sample adopted in this work preferentially selects measurements made over Titan's northern hemisphere, toward the facing-Saturn side, and exclusively at solar minimum conditions.

Determination of the densities of neutral constituents in Titan's upper atmosphere is complicated by the fact that the counts in a particular mass channel are likely to be contributed by more than one species. In order to untangle these overlapping cracking patterns between different species, we adopt Singular Value Decomposition (SVD) to constrain the densities of all species simultaneously (Press et al., 1992). Various tricks are adopted in the SVD analysis to minimize the coupling between different species, the number of free parameters in the fit, as well as uncertainties of the derived densities. These include (1) calculating the densities of N_2 and $^{14}N^{15}N$ directly from counts in channels 14, 28 and 29, which are then used to fix the densities of $^{15}N^{15}N$ according to the observed nitrogen isotope ratios; (2) treating the combination of C_2H_2 and C_2H_4 as an *imaginary* species, in the form of $\frac{3}{4}n(C_2H_2)+\frac{1}{4}n(C_2H_4)$; (3) determining the $^{13}CH_4$ densities from an ad-hoc carbon isotope ratio, with diffusive separation taken into account; and (4) adopting a scheme in which whether a given species is included in the SVD fit depends on its signal-to-noise ratio in one of its main channels.

With the procedures described above, we divide the whole sample into 133 individual mass spectra, obtained by averaging over different altitude bins for any given flyby. Inbound and outbound measurements are treated separately. Error analysis shows that for relatively abundant species such as CH_4, H_2 and C_2H_2/C_2H_4, uncertainties due to sensitivity calibration are the dominant sources of error, whereas for most minor species, those due to counting statistics are more important.

For most minor neutral species in Titan's upper atmosphere, the density measurements show clear asymmetry about C/A, in the sense that density enhancement is always observed during the outbound legs. This can be interpreted as a result of wall effects, which can be either adsorption/desorption of incoming molecules or heterogeneous surface chemistry on the chamber walls. The wall effect has also been used to argue for the detection of NH_3 based on the INMS data. We propose a simple model to describe the processes of adsorption/desorption, assuming a constant adsorption probability and a desorption time constant inversely proportional to the N_2 density in the INMS chamber. Such a model reasonably reproduces the observed time behavior of several heavy species, and suggests that both the inbound and outbound measurements tend to underestimate the true atmospheric abundances by as large as an order of magnitude, when taking into account ram pressure enhancement only. However, in most cases, possible values of the adsorption probability and desorption time constant are not well constrained, leading to relatively large uncertainties of the true atmospheric abundances. For several species, including C_6H_6, C_7H_8 and NH_3, the simple model of adsorption/desorption may not be valid since heterogeneous surface chemistry on the chamber walls might be of more importance, due to the relatively high abundances of the associated radicals in the ambient atmosphere (Vuitton et al., 2008). For N_2, CH_4, H_2 and ^{40}Ar, the wall effects are negligible, since the average inbound and outbound profiles are nearly identical. We use both the inbound and outbound data in our analysis of the distribution of N_2, CH_4, H_2 and ^{40}Ar (as well as their isotopes) in Titan's upper atmosphere. For other minor species, we present both their abundances directly obtained from the inbound measurements adopting the 'ideal' ram enhancement factor (see Table 3), and their abundances corrected for wall adsorption/desorption (see Table 4).

We perform an analysis of the globally averaged density distribution of N_2, CH_4 and H_2 in Titan's upper atmosphere between 950 and 1500 km. The barometric model fitting of the N_2 profile gives a best-fit thermospheric temperature of 151.0 ± 1.5 K, consistent with previous determination (Vervack et al., 2004; Yelle et al., 2006; Cui et al., 2008). The average CH_4 and H_2 profiles are each described by the diffusion model, which constrains their most probable fluxes as $2.6 \times 10^9\ \mathrm{cm^{-2}\,s^{-1}}$ and $1.1 \times 10^{10}\ \mathrm{cm^{-2}\,s^{-1}}$, referred to Titan's surface. An eddy profile given by Yelle et al. (2008) is adopted in the diffusion model fitting. The H_2 flux is higher than the Jeans value by nearly a factor of 3, which has been interpreted as enhanced thermal escape primarily driven by an upward conductive heat flux (Cui et al., 2008). However, the interpretation of the CH_4 flux requires non-thermal escape processes (De La Haye et al., 2007a, 2007b; Yelle et al., 2008).

Among all the minor species included in our spectral analysis, we have firm detections of C_2H_2, C_2H_4, C_2H_6, CH_3C_2H, C_4H_2, C_6H_6, CH_3CN, HC_3N, C_2N_2 and NH_3, based on direct inbound measurements. However, the detection of NH_3 in Titan's upper atmosphere deserves some caution, since a significant fraction of the observed NH_3 molecules might be those formed on the chamber walls from N and H radicals in the ambient atmosphere. Upper limits are put for C_3H_8, C_4H_6, C_7H_8, C_2H_3CN, H_2O and CO_2, in a global average sense. The abundances of heavy hydrocarbons and nitrogen-bearing species derived directly from the INMS neutral data are systematically lower than the values predicted from the ion-neutral chemistry model with ion densities obtained from the INMS data in the OSI mode (Vuitton et al., 2007). However, with reasonable corrections for wall adsorption/desorption, both works reach consistent results.

Finally, the INMS data also show some signature of horizontal/diurnal variations of temperature and neutral gas distribution in Titan's thermosphere, which can be summarized as follows: (1) The equatorial regions appear to be warmer, and present some evidences for the depletion of light species such as CH_4 as well as accumulation of some heavy species. The meridional variation of H_2 shows a more complex pattern, with enhanced mixing ratios present at mid latitudes. (2) The magnetospheric ramside of Titan appears to be warmer than the wakeside. The distribution of CH_4 is found to be depleted at the ramside and accumulated at the wakeside. The zonal variation of H_2 seems to present a different pattern. No reliable zonal variation of heavy species can be concluded. (3) Titan's nightside hemisphere appears to be warmer than the dayside, and shows depletion of light species including both CH_4 and H_2. No diurnal variation is observed for heavy species.

While some of the above variations might be interpreted by either the solar-driven models or auroral-driven models, proposing a physical scenario that reconciles all the observed horizontal/diurnal variations in a consistent way is not easy. This requires a careful evaluation of the effect of restricted sampling. Especially, we notice that the available INMS measurements made near the north polar region also preferentially select the wakeside and dayside of Titan. This implies that from a pure observational point of view, we can not distinguish between a cooler north pole, a cooler wakeside and a cooler dayside. The observed horizontal/diurnal variations of H_2 present a further complication, and the effects of rapid thermal escape and large ballistic flow in the exosphere may also be important.

Acknowledgments

This work is supported by NASA through grant NAG5-12699 to the Lunar and Planetary Laboratory, University of Arizona. We are grateful to Roland Thissen for useful discussions on problems with calibration of the mass spectrometry data, and Ronald Vervack regarding the Voyager UVS data and analysis. We also wish to thank the anonymous referees for their useful comments on this manuscript.

Appendix A. Calibrations

We present in this appendix the details of the INMS data calibration in the CSN mode. Specifically, we take into account calibration of sensitivities, ram pressure enhancement, saturation in the high gain counter, thruster firing contaminations, subtraction of background counts, as well as channel crosstalk.

A.1. Sensitivities

The laboratory sensitivity calibration of the INMS flight unit (hereafter FU) was performed at Goddard Space Flight Center (GSFC) prior to launch (Waite et al., 2004). This pre-flight calibration was performed with the principle non-reactive neutral species expected on Titan, including N_2, CH_4, H_2, C_2H_2, C_2H_4 and ^{40}Ar. In addition, He and Kr were also chosen as reference species. Especially, Kr was used to characterize the FU performance for large M/Z (Waite et al., 2004). The calibration with Kr is important because of the presence of heavy hydrocarbons on Titan, such as C_6H_6 (Vuitton et al., 2008).

Characterization of INMS performance was continued during the post-launch period with the engineering unit (hereafter EU), including additional neutral species that had not been calibrated pre-flight. After the initial EU characterization immediately post-launch, the EU sensor ion sources were refurbished to better represent FU. This refurbished engineering unit (hereafter REU) has been used since early 2006 to characterize a large number of gases of scientific interest on Titan guided by preliminary INMS results. Because of differences in the response of the FU and REU, it is necessary to derive an algorithm to transfer the REU sensitivities for the newly calibrated gases to the FU. This algorithm, described below, is based on the gases common to both the FU and REU calibrations.

It is also worth mentioning that the FU and/or REU characterizations of several species were performed on mixtures of reference gases with isotopes (e.g., $^{14}N_2$ and $^{14}N^{15}N$, $^{12}CH_4$ and $^{13}CH_4$, ^{40}Ar and ^{36}Ar). Before calibration between the FU and REU sensitivities is made, we separate the relative contributions from the main gas and its isotope with the appropriate terrestrial isotope ratios. The procedure for correcting for isotope ratios will not be detailed here.

A.1.1. Calibrations of peak sensitivities between flight unit (FU) and refurbished engineering unit (REU)

We present several possible schemes for calibrating the peak sensitivities between the FU and REU characterizations. The calibration depends on eight species for which both FU and REU sensitivities are available, including H_2, He, CH_4, C_2H_2, N_2, C_2H_4, Ar, Kr and their isotopes. The peak sensitivity of a neutral species always refers to the highest value shown in its cracking pattern. For most species, the channel of peak sensitivity corresponds to the singly ionized state of the parent molecule.

One possible scheme for calibrating peak sensitivities is to examine the offsets between FU and REU values, i.e., $S_{FU}-S_{REU}$. The upper panel of Fig. 26 shows that although the scattering is relatively large, the offset varies approximately linearly with M/Z. The best-fit linear relation is given by the solid line in the figure. The lower panel of Fig. 26 presents the relation between REU peak sensitivities and M/Z, with the solid line giving the offsets that need to be applied to obtain the FU values. We see that for several heavy species (C_4H_6, C_2H_3CN, C_6H_6 and C_7H_8), the required offsets are comparable with or even greater than the measured REU sensitivities. This raises a conceptual difficulty, in the sense that the peak sensitivity for a heavy species might be largely controlled by the offset alone, independent of the actually measured REU value. This is a physically unrealistic situation, and the scheme for calibration based on offset is therefore not adopted in this work.

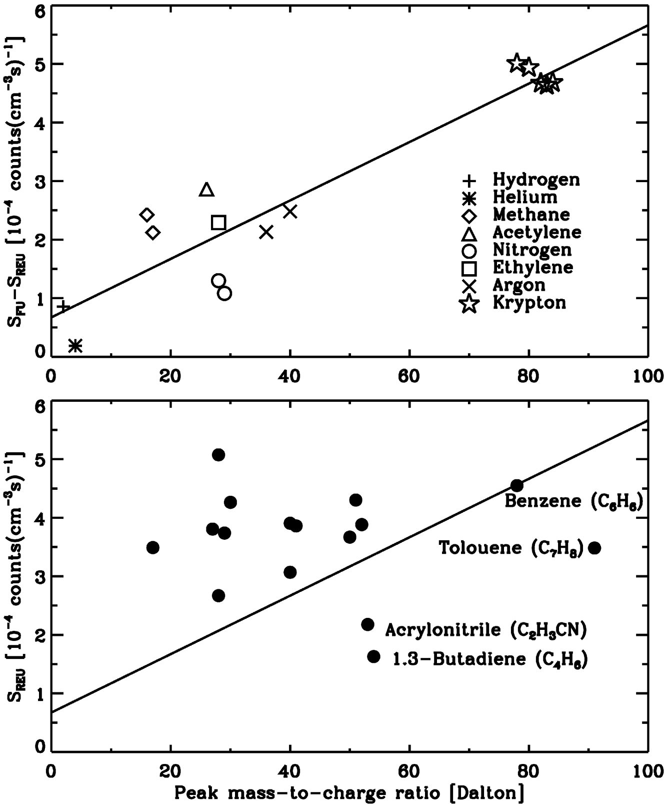

Fig. 26. Upper panel: The difference between the FU and REU peak sensitivities shown as a function of peak M/Z. All FU/REU measurements can be roughly fitted with a linear relation. Lower panel: The REU peak sensitivities as a function of peak M/Z. The solid line represents the offset, $S_{FU} - S_{REU}$ that needs to be applied to get the corresponding FU values. For several heavy neutral species (C_4H_6, C_2H_3CN, C_6H_6 and C_7H_8), the required offsets are comparable with or greater than the measured REU sensitivities.

As an alternative scheme, we normalize the REU sensitivities to the FU values with a direct scaling, as shown in Fig. 27a. Except for Kr, the correlation between the FU and REU values can be reasonably described by a linear relation, shown as the solid line in Fig. 27a. However, the Kr data are quite badly fit by the linear relation. This is a serious failure because Kr is the only species available for characterizing the high-mass end of the INMS spectrum, and it is important to adopt a calibration scheme that is valid for this species.

We further investigate a different linear relation between the FU and REU peak sensitivities, in which data from both FU and REU are scaled by the cross section of electron impact ionization for the species in question. Such a scaling is physically motivated, since the probability of ionization by electron impact is proportional to the corresponding cross section. The relation between the FU and REU peak sensitivities scaled by cross section is shown in Fig. 27b, indicating that measurements for Kr are still outliers, similar to the unscaled case.

The way that an ionized molecule passes through the switching and focusing lens system depends on M/Z (Waite et al., 2004). This motivates us to investigate the relationship between the FU and REU peak sensitivities, when both are scaled by M/Z of the disso-

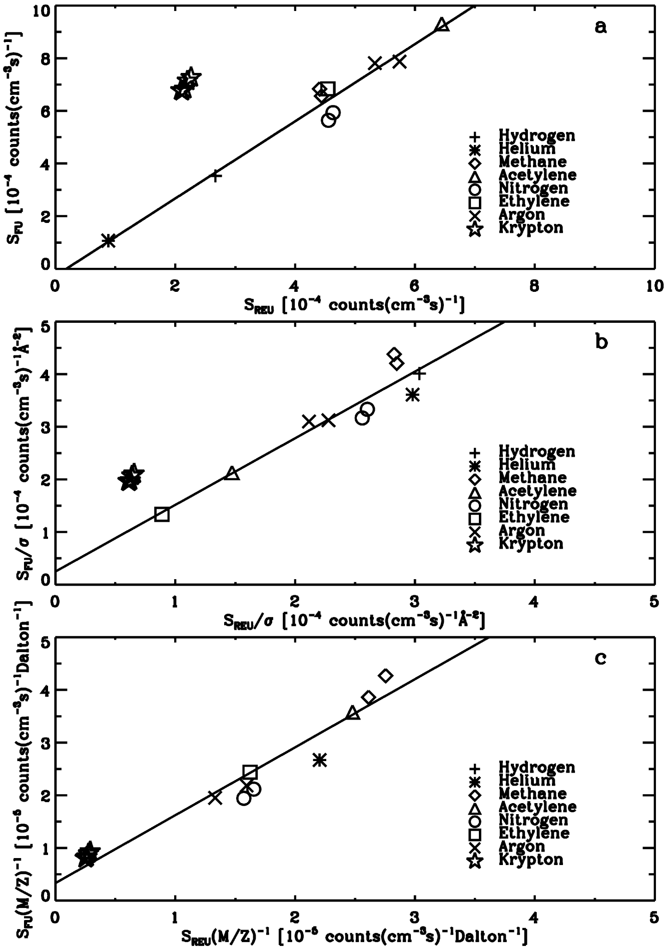

Fig. 27. The relation between the FU and REU peak sensitivities, unscaled (panel a), scaled by the cross section for electron impact ionization (panel b), or scaled by the peak M/Z (panel c). Except for panel c, isotopes of Kr appear to be outliers. The solid lines are obtained by a linear fitting to the FU and REU measurements, including all species for panel c but excluding Kr for panels a and b. The best-fit relation shown in panel c is given by Eq. (A.1).

Table 8
Flight unit peak sensitivities. Values in parentheses are calibrated REU values according to Eq. (A.1), while the remainings are directly measured FU values. All sensitivities are in units of 10^{-4} counts $(\mathrm{cm}^{-3}\,\mathrm{s})^{-1}$.

Species	Name	Peak M/Z	S_{FU}	$\sigma(S_{FU})/S_{FU}$
H_2	Hydrogen	2	3.526	0.018
HD	Deuterium hydride	3	1.857	0.021
CH_4	Methane	16	6.833	0.025
$^{13}CH_4$	Methane	17	6.563	0.027
(NH_3)	Ammonia	17	5.068	0.032
(H_2O)	Water	18	4.696	0.036
C_2H_2	Acetylene	26	9.310	0.028
(HCN)	Hydrogen cyanide	27	5.809	0.042
C_2H_4	Ethylene	28	6.836	0.038
N_2	Nitrogen	28	5.931	0.044
$^{14}N^{15}N$	Nitrogen	29	5.638	0.047
$(^{15}N^{15}N)$	Nitrogen	30	6.498	0.042
(C_2H_6)	Ethane	28	7.478	0.035
^{36}Ar	Argon	36	7.872	0.042
^{40}Ar	Argon	40	7.811	0.046
$(CH_2C_2H_2)$	Allene	40	6.368	0.055
(CH_3C_2H)	Methyl acetylene	40	5.288	0.066
(CH_3CN)	Acetonitrile	41	6.343	0.057
(C_3H_8)	Propane	29	5.787	0.045
(CO_2)	Carbon dioxide	44	8.154	0.048
(C_4H_2)	Diacetylene	50	6.396	0.068
(HC_3N)	Cyanoacetylene	51	7.244	0.061
(C_2N_2)	Cyanogen	52	6.737	0.067
(C_2H_3CN)	Acrylonitrile	53	4.569	0.099
(C_4H_6)	1,3-Butadiene	54	3.895	0.118
(C_2H_5CN)	Propanenitrile	28	4.374	0.056
(C_6H_6)	Benzene	78	8.460	0.079
(C_7H_8)	Toluene	91	7.516	0.103

ciative fragments. Such a relation is presented in Fig. 27c, which shows that all species, including Kr, lie approximately on a straight line given by

$$(\mathrm{M/Z})^{-1} S_{\mathrm{FU}} = 3.32 \times 10^{-6} + 1.29(\mathrm{M/Z})^{-1} S_{\mathrm{REU}}, \tag{A.1}$$

where S_{FU} and S_{REU} represent the FU and REU peak sensitivities in units of counts $(\mathrm{cm}^{-3}\,\mathrm{s})^{-1}$. We adopt this relationship to transfer REU sensitivities to the FU. However, for species for which both REU and FU calibrations are available, the FU peak sensitivities are always used.

An estimate of the uncertainties of peak sensitivities is required, which can be used to determine the density errors of the ambient atmosphere from the INMS data (see Section 3.4). The measured uncertainties of the lab data due to counting statistics are very small, as compared with the scatterings of the lab data from the best-fit relation (Eq. (A.1)). To characterize the scatterings of the lab data, the uncertainties for the two coefficients in Eq. (A.1) are calculated from the corresponding covariance matrix. These are then used to calculate the uncertainties of the peak FU sensitivities. The peak sensitivities for all neutral species included in our spectral analysis, appropriate for the FU characterization, are listed in Table 8, with 1σ relative uncertainties. The relative uncertainty tends to increase with mass, and can be as large as 10% for complex species such as C_4H_6 and C_7H_8. The origins for the listed sensitivities are also indicated in Table 8, either directly taken from pre-flight measurements, or calibrated from the REU values according to Eq. (A.1).

We notice that the best-fit linear relation given by Eq. (A.1) has a finite offset, implying that the predicted FU peak sensitivity is non-zero even if the REU calibration gives a zero sensitivity. Although this is a physically unrealistic feature, the smallest peak sensitivity (scaled by M/Z) among all species appears for C_4H_6 with a value of 7.22×10^{-6} counts $(\mathrm{cm}^{-3}\,\mathrm{s})^{-1}$. This is more than a factor of 2 greater than the offset value of 3.32×10^{-6} counts $(\mathrm{cm}^{-3}\,\mathrm{s})^{-1}$, implying that the potential errors associated with the non-zero offset in Eq. (A.1) are not significant.

Finally, we emphasize that the REU-to-FU conversion according to Eq. (A.1) is chosen to be valid for Kr, which is the only species available for characterizing the high-mass end of the INMS spectrum. Accordingly, such a scheme gives different peak sensitivities for heavy species such as C_6H_6, as compared with the other two schemes in Figs. 27a and 27b. On the other hand, different schemes give similar peak sensitivities for relatively light species, since all of them work reasonably well at the low mass end. More specifically, we notice that the peak sensitivity of C_6H_6 calculated with Eq. (A.1) is 32% higher than the value from unscaled conversion (Fig. 27a) and 11% lower than the value from conversion scaled by cross section (Fig. 27b). In contrast, the difference in peak sensitivities of C_2H_6 is only ∼5% for different schemes. These facts imply that different schemes of the FU-to-REU conversion give similar abundances for relatively light neutral species but significantly different results for heavy ones. However, as addressed in Section 4.1, the primary uncertainties in the derived densities of minor species are more likely to be associated with wall effects.

A.1.2. Cracking patterns

In addition to the peak sensitivity, the cracking pattern of a given neutral species, i.e., the ratios of the sensitivities of various dissociative fragments to the peak sensitivity, also requires calibration between the FU and REU measurements. We show in Fig. 28 the FU and REU branching ratios for several species, in-

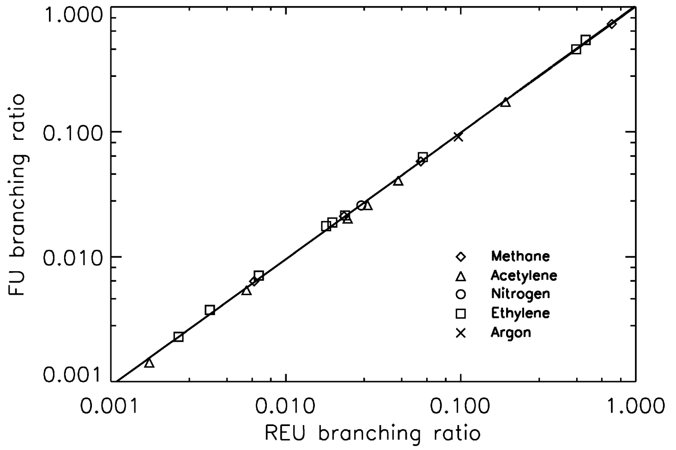

Fig. 28. The relation between the REU and FU branching ratios for N_2, CH_4, ^{40}Ar, C_2H_2 and C_2H_4. The solid line shows the best-fit log-linear relation, given by Eq. (A.2).

cluding N_2, CH_4, C_2H_2, C_2H_4 and Ar. Typically, the REU and FU cracking patterns are nearly identical. Fig. 28 shows that the calibration between the REU and FU branching ratios can be described by a log-linear relation with the form

$$\log b_{\mathrm{FU}} = 0.007 + 1.014 \log b_{\mathrm{REU}}, \tag{A.2}$$

where b_{FU} and b_{REU} represent the FU and REU branching ratios. Such a log-linear relation is given by the solid line in Fig. 28. Similar to the calibration of peak sensitivities, for all species with FU characterization available, the FU cracking patterns are always adopted. For gases with only REU measurements, Eq. (A.2) is used to predict the corresponding FU cracking patterns. The corrections according to Eq. (A.2) are small, ranging between 0.5% and 7%.

Uncertainties of the inferred branching ratios are estimated from the errors of the two coefficients in the log-linear relation given by Eq. (A.2), which are calculated from the corresponding covariance matrix. On average, the relative uncertainties of branching ratios are ~4%. Also notice that the calibration of cracking pattern presented here depends on the measurements of dissociative fragments with $M/Z < 20$. A simple extrapolation to heavy fragments, encountered in the cracking patterns of heavy neutral species such as C_6H_6, is implicitly assumed in the calibration.

Additional calibration of the cracking pattern is required to guarantee that densities of a given species derived from different channels are consistent. As an example, we find that the N_2 densities determined from channel 28 are not identical to those determined from channel 14. As pointed out by Yelle et al. (2006), this may reflect a change of the INMS sensitivity to N_2 at channel 14, likely to be caused by excess kinetic energy imparted to N^+ ions through electron impact dissociative ionization of N_2. This may influence the N_2 branching ratio at channel 14, by affecting the way that the fragment ions are transmitted through the INMS ion optics. To correct for this, we calculate for each flyby the ratio of the N_2 density profile determined from channel 28 to that determined from channel 14, between 1100 and 1450 km. For each flyby, the average ratio is taken as a constant scaling factor, which is then used to calibrate the branching ratio of N_2 at channel 14 to guarantee that the N_2 densities determined from channel 14 are consistent with those determined from channel 28.

A similar procedure is performed for calibrating the branching ratios of CH_4 at channels 12, 13 and 15. An analogous scaling factor for CH_4 at channel 14 is not considered, since it is coupled to the issue of N_2 calibration at the same channel. An illustration is given in Fig. 29, with the solid circles representing N_2 (CH_4) densities determined from counts in channel 28 (16) and the plus signs representing those determined from counts in channel 14 (12) adopting the uncalibrated branching ratios. Offsets are clearly seen between them. The open diamonds in Fig. 29 give the densities derived from the calibrated branching ratios, which are consistent with those determined from the peak channels. The mean scaling factors are 0.83 ± 0.03 for N_2 at channel 14, 0.78 ± 0.02 and 0.82 ± 0.01 for CH_4 at channels 12 and 13, where the errors quoted here reflect scatterings among different flybys. The CH_4 scaling factor at channel 15 is very close to unity for all flybys.

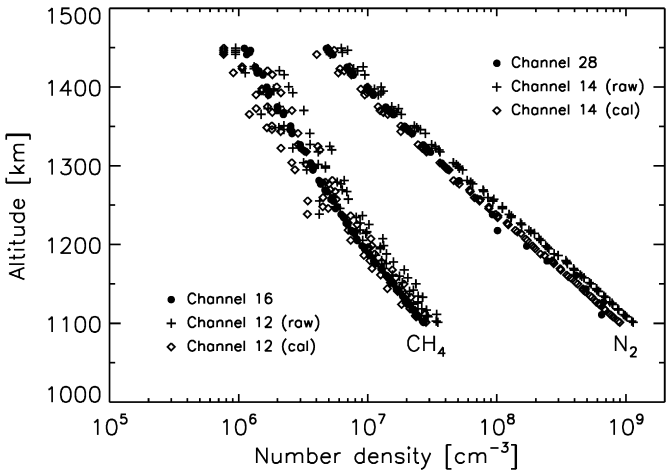

Fig. 29. The N_2 and CH_4 density profiles (for the inbound T32 measurements) as a function of altitude, determined from counts in different channels. The solid circles represent densities determined from counts in the main channel (28 for N_2 and 16 for CH_4), while the plus signs represent those from counts in a secondary channel (14 for N_2 and 12 for CH_4). The open diamonds are densities determined from the secondary channels, scaled to ensure agreement with densities determined from the peak channels.

In principle, a similar calibration is required for other species. However, a full knowledge of all the individual scaling factors is impossible, due to the coupling between cracking patterns of these species. In addition, introducing too many scaling factors is equivalent to introducing the same number of free parameters in the overall fit of an observed mass spectrum, which is practically unrealistic and unnecessary. For simplicity, such a correction for other species is not attempted in this work. However, it should be born in mind that the neglect of this effect may introduce additional uncertainties as large as ~20% in the derived densities of a neutral species, unless the densities are primarily estimated from the peak channel.

A.2. Ram pressure enhancement

The INMS response in the CSN mode, in terms of the ram pressure enhancement factor, is shown in Fig. 30, for several species with different molecular masses. For instrument configurations with the angle of attack (the angle between the INMS aperture normal and the spacecraft velocity) smaller than 90°, an enhancement of the ambient number density is achieved by limiting the conductance through the transfer tube (to the ionization region) and maintaining the high conductance through the entrance aperture (Waite et al., 2004). With the presence of the spherical antechamber, the closed source has a geometric field of view as wide as 2π steradians, and the angular response varies as the cosine of the angle of attack (Waite et al., 2004). The ram enhancement factor increases with molecular mass. At a temperature of 150 K for the ambient atmosphere, the maximum enhancement factor, which appears for zero angle of attack, ranges from 13.5 for H_2, 38 for CH_4, 50 for N_2, 60 for ^{40}Ar, to 84 for C_6H_6. For angles of attack greater than 90°, the instrument response drops to zero, and the

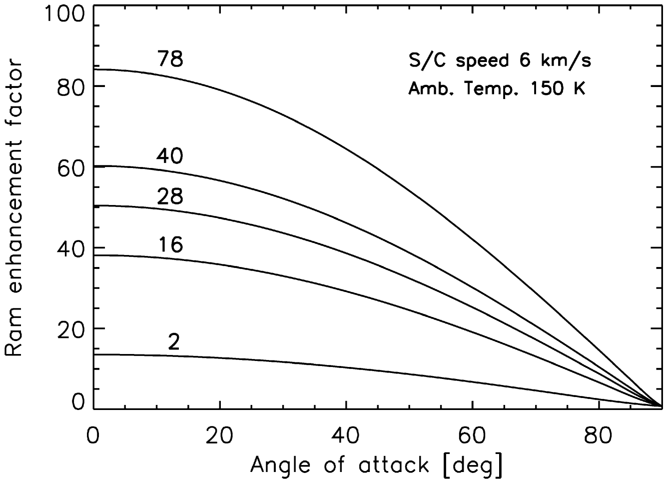

Fig. 30. The INMS instrument response in the CSN mode (the ram enhancement factor), as a function of angle of attack, i.e., the angle between the aperture normal and the spacecraft velocity vector. Several species with different molecular masses are shown, assuming a spacecraft velocity of 6 $\mathrm{km\,s^{-1}}$, a temperature of 150 K in the ambient atmosphere, and a chamber wall temperature of 300 K. The instrument response increases with molecular mass and varies approximately as the cosine of the angle of attack.

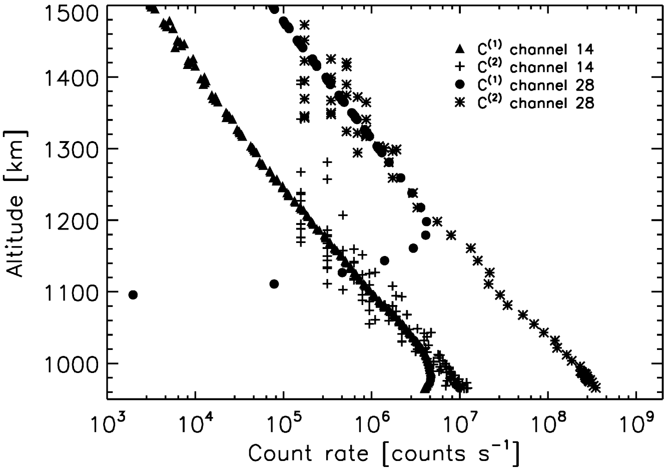

Fig. 31. The count rates in channels 14 and 28 as a function of altitude, adopted from the INMS measurements made during the inbound T32 flyby. Solid triangles and circles represent data recorded at the $C^{(1)}$ counter, while plus signs and asterisks represent data recorded at the $C^{(2)}$ counter, multiplied by the average conversion ratios of 5792 for channel 28 and 5606 for channel 14. The $C^{(1)}$ count rates are saturated at altitudes below ∼1200 km for channel 28 and below ∼1020 km for channel 14.

spacecraft configuration does not allow the recording of any useful data of the ambient atmosphere.

The instrument response mentioned above implies an effective peak sensitivity for any given species that is equal to the actual sensitivity multiplied by the corresponding ram enhancement factor (see also Section 3.1). The dependence of the instrument response on molecular mass, angle of attack, as well as the temperature of the ambient gas can be predicted from the kinetic theory, which estimates the number density in the antechamber by balancing the incoming flux at the spacecraft velocity with the outgoing flux at the thermal velocity corresponding to the wall temperature (Waite et al., 2004). Throughout this work, the ram enhancement factor is calculated from the kinetic theory with a fixed spacecraft velocity of 6 $\mathrm{km\,s^{-1}}$, a temperature of 150 K in the ambient atmosphere, and a chamber wall temperature of 300 K.

The above discussion on ram pressure enhancement implicitly assumes that the incoming molecules through the entrance aperture collide elastically with the chamber walls, and effects such as adsorption/desorption and heterogeneous surface chemistry are not involved. However, such an assumption may not be correct, as described in Section 4.1.

A.3. Saturations

The INMS has both a high gain counter (hereafter $C^{(1)}$) and a low gain counter (hereafter $C^{(2)}$). In more detail, two electron multipliers are electronically biased to allow most of the ions to be deflected into the primary detector, with the remaining being scattered into the secondary one (Waite et al., 2004). This design increases the overall dynamic range of INMS measurements by a factor of 1500 (Waite et al., 2004). When not saturated, the $C^{(1)}$ counts, with much higher signal-to-noise ratios than $C^{(2)}$, are always used for density determination. However, the $C^{(1)}$ counts for channels 14, 15, 16, 28 and 29 are likely to be saturated at low altitudes, leading to an underestimate of the densities of N_2, CH_4 and $^{14}N^{15}N$ in the ambient atmosphere. This typically happens as the signal approaches a level of $\sim 10^5$ counts per IP in the $C^{(1)}$ counter. Correction for saturation requires a determination of the $C^{(1)}/C^{(2)}$ conversion ratio, which is assumed to be constant for a given mass channel and for a given flyby in our work. At low altitudes, these conversion ratios are used to scale the $C^{(2)}$ counts to the actual $C^{(1)}$ counts, from which unbiased densities can be determined.

We calculate the $C^{(1)}/C^{(2)}$ conversion ratios for channels 14, 15, 16, 28 and 29 with the following procedure. First, we correct all $C^{(1)}$ counts for saturation assuming a detector dead time of 3.26×10^{-8} s (Waite et al., 2004). Adopting a threshold count rate of 1.0×10^5 counts/IP, we then determine the altitude boundary where the $C^{(1)}$ counts for the given channel reach the threshold. Regions below this altitude are considered to be saturated for that channel. Finally, we examine the linear correlation between the $C^{(1)}$ and $C^{(2)}$ counts, with the best-fit slope adopted as the $C^{(1)}/C^{(2)}$ conversion ratio for that channel. In such a procedure, only inbound data are considered, to avoid possible problems associated with detector fatigue. Such problems are evident for the T16 flyby and could be present at a less obvious but still troubling level for other flybys.

The $C^{(1)}/C^{(2)}$ conversion ratio, which is assumed to be constant for each flyby, varies for different channels. The average values are 5606 ± 288 for channel 14,4237 ± 233 for channel 15,3977 ± 186 for channel 16,5792 ± 255 for channel 28, and 5741 ± 315 for channel 29, where the uncertainties represent standard deviations among different flybys. An illustration of the $C^{(1)}/C^{(2)}$ conversion is given in Fig. 31 for the inbound T32 data. The solid circles (triangles) represent $C^{(1)}$ counts of channel 28 (14), and the asterisks (plus signs) represent the corresponding $C^{(2)}$ counts multiplied by the average conversion ratio. Throughout this work, the average values of the $C^{(1)}$–$C^{(2)}$ conversion ratios are adopted to correct for saturation in channels 14, 15, 28 and 29, for all flybys.

A.4. Thruster firings

For channel 2, additional corrections for thruster firings are required (Yelle et al., 2006; Cui et al., 2008). The Cassini spacecraft thrusters operate with hydrazine (N_2H_4), with H_2 being a significant component of the thruster effluent. This effect is usually manifest as large excursions from the expected counts in channel 2, interspersed over the whole altitude range over which measurements were made. In most cases, contamination by thruster firings is serious near C/A when thrusters fire frequently to offset the torque on the spacecraft due to atmospheric drag (Yelle et al., 2006). Regions thought to be contaminated by thruster firings are identified by correlating with accumulated thruster operation time,

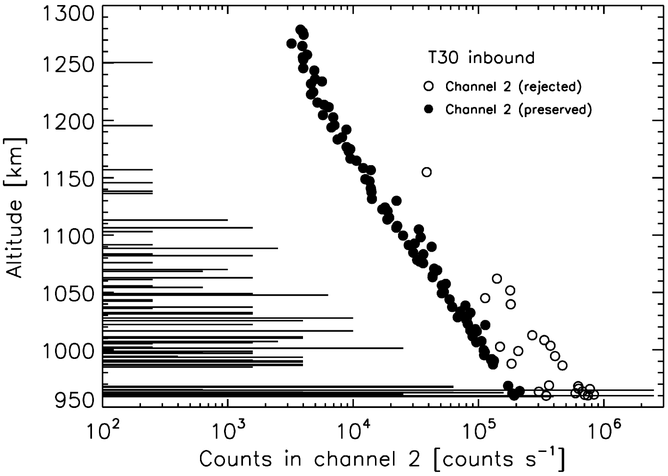

Fig. 32. The count rates in channel 2 as a function of altitude, for the inbound T30 flyby. Overplotted on the count rate profile is the information of accumulated thruster operation time on 1 s intervals. Each thruster firing nominally lasts 0.125 s, from which we calculate the total number of thruster firings in each 1 s interval. This number is shown on an arbitrary linear scale, at altitudes that coincide with real measurements made in channel 2. The channel 2 counts rejected from the spectral analysis due to thruster firing contaminations are shown as the open circles, while those uncontaminated are shown as the solid circles.

accompanied by eyeball checking (Cui et al., 2008). The counts in channel 2 for these regions can be replaced by the values interpolated from surrounding measurements unaffected by thruster firings for each flyby. The contamination of channel 28 counts by the same effect is ignored here, since the N_2 densities of the ambient atmosphere are much higher than those of the spacecraft effluent.

An example of the thruster firing contaminations is shown in Fig. 32, for the inbound T30 measurements. The open (solid) circles represent channel 2 counts which are thought to be contaminated (uncontaminated) by this effect. Also shown on the figure is the information on the accumulated thruster operation time on 1 s intervals. Each thruster firing nominally lasts 0.125 s, from which we calculate the total number of thruster firings in each 1 s interval. This number is shown on an arbitrary linear scale in Fig. 32, at altitudes that coincide with real measurements made in channel 2. Fig. 32 shows that the total number of thruster firings is not exactly correlated with the apparent deviations of channel 2 counts. Eyeball checking and manual rejection are sometimes required, in order to obtain a reasonable correction for the thruster firing contaminations.

A.5. Subtraction of background counts

A.5.1. Empirical background model

A typical INMS mass spectrum at low altitudes shows clear peaks centered in isolated mass channels, superimposed on a broad smooth spectrum extending over the whole M/Z range from 1 to 99 Daltons. While the isolated peaks are clearly associated with neutral constituents in the INMS antechamber, the broad spectrum is interpreted as background signals.

To subtract the background spectra, we construct an empirical model, $B(\mathrm{M/Z})$, defined as the sum of a constant level and the convolution of a square function with a Gaussian kernel,

$$B(\mathrm{M/Z})=\frac{1}{\sqrt{2\pi w^2}}\int_{m_0-\frac{\Delta}{2}}^{m_0+\frac{\Delta}{2}} h\exp\left[-\frac{(\mathrm{M/Z}-m)^2}{2w^2}\right]dm+c, \qquad (\mathrm{A.3})$$

where c is the constant level, h, m_0 and Δ are the height, center and width of the square function, w is the width of the Gaussian kernel. There are consequently five free parameters in the empirical model fitting.

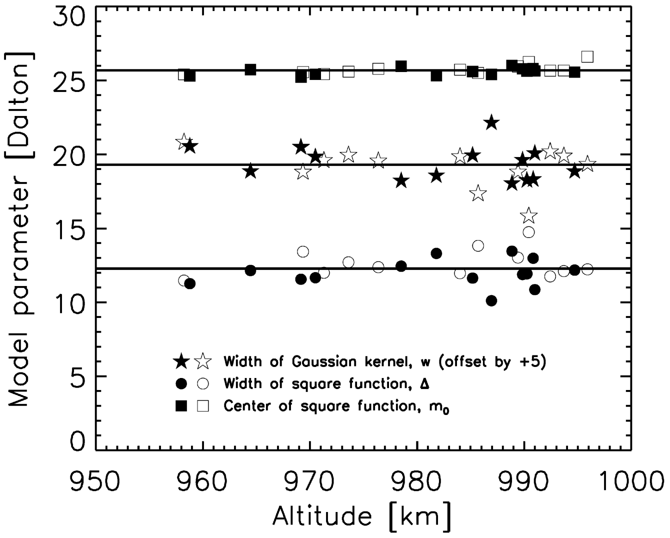

Fig. 33. The width of the Gaussian kernel, the center and width of the square function for the empirical model fitting of the background mass spectra (see Eq. (A.3)). Solid and open symbols stand for inbound and outbound, respectively. The values of the Gaussian width have been artificially offset by +5 Dalton to make them separate from the width of the square function in the figure. All parameters shown in the figure appear to be constant with altitude. The mean values, given by the dashed lines, are 14.2 for the width of the Gaussian kernel, 25.7 for the center of the square function, and 12.2 for the width of the square function. These mean values are fixed in the empirical background model fitting.

In practice, for a given mass spectrum, we determine the constant level, c by taking the average of all counts in channels with $\mathrm{M/Z} > 65$. Channels 73–80 and 90–91 are not included, to avoid possible contributions from C_6H_6 and C_7H_8 molecules in the ambient atmosphere (or the INMS antechamber). The most probable values for the other parameters in the empirical model are determined by a Levenberg–Marquardt least-squares fit to measured counts with the constant level subtracted (Press et al., 1992). Except for mass slots associated with C_6H_6 and C_7H_8, channels 12–18, 24–30, 39–40, 44, 49–52, 61–62 are also excluded in the background fitting, since these channels are likely to be contributed by various neutral species in Titan's upper atmosphere (see Section 3.3).

Because the signals in the background spectra are relatively low, an accurate determination of the model parameters is sometimes difficult. This is an especially serious concern at high altitudes where the Levenberg–Marquardt least-squares fit occasionally gives unrealistic parameter values for h, Δ, m_0 or w (e.g., negative). Usually, this happens when many channels under consideration have zero counts.

To avoid the above difficulty, we first consider measurements made at altitudes below 1000 km and typically binned by 25 km, where values of all the free parameters can be determined accurately. Although the binsize is smaller than the spatial resolution of 56 km for most channels (see Section 2), a binned spectrum typically incorporates 2–3 consecutive measurements in any given channel, due to the inclination of the spacecraft trajectory with respect to vertical. The empirical fitting for each flyby is performed on the mass spectra with count rates in all channels interpolated to a common altitude grid defined by channel 26, i.e., the main peak channel of C_2H_2 (see Table 8).

We present in Fig. 33 the variations of the parameters w, Δ and m_0, which show that their values are approximately independent of altitude. Notice that the values of w have been artificially offset by +5 Dalton to make them separate from Δ in the figure.

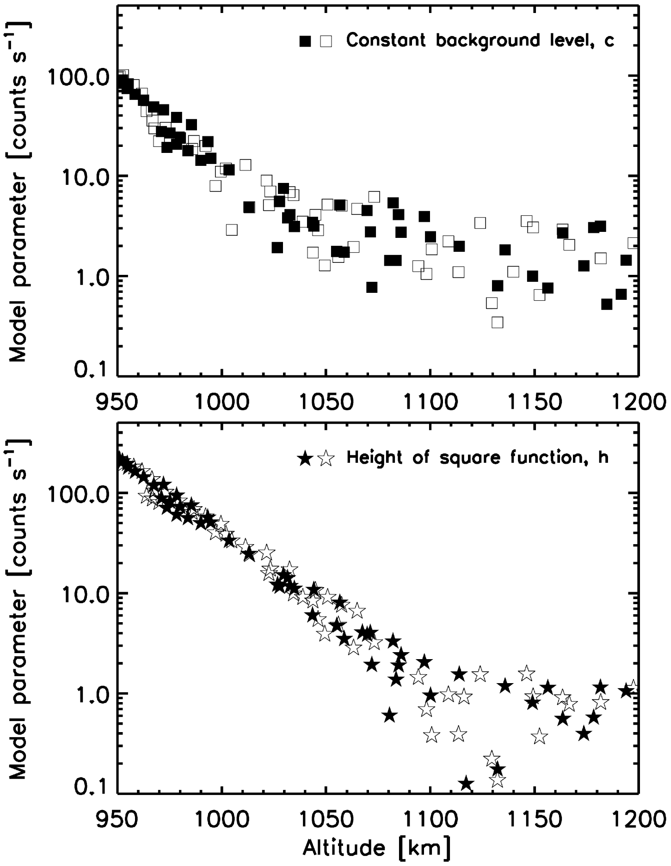

Fig. 34. The constant level (squares) and the height of the square function (five-stars) for the empirical model fitting of the background mass spectra (see Eq. (A.3)). Solid and open symbols stand for inbound and outbound, respectively. Both parameters show strong altitude variations.

The negligible variations of these parameters with altitude suggest us to adopt the mean values of w, Δ and m_0 as fixed model parameters at all altitudes and for all flybys. Specifically, we adopt $w = 14.2 \pm 1.3$, $\Delta = 12.2 \pm 1.0$ and $m_0 = 25.7 \pm 0.3$, where all values are in units of Dalton and the 1σ errors represent standard deviations. With these fixed values, we run Levenberg–Marquardt least-squares fit again on the unbinned spectra, and the values for the remaining parameter, h at all altitudes can be reliably determined from the data. The variations of this parameter, as well as the constant level, c are presented in Fig. 34, both of which show strong altitude dependence. It also appears that both parameters tend to be constant with altitude above ∼1100 km. A typical example of the empirical background fitting is shown in Fig. 35, for the inbound T16 observation at an altitude of ∼995 km. Values for w, Δ and m_0 are fixed in the fitting, whereas c and h are treated as free parameters. Such a scheme is adopted throughout this work.

The errors associated with the background signals are estimated with a Monte-Carlo method, in which the mean values and uncertainties of all free parameters in the empirical background fitting are estimated from the spread of points in Figs. 33 and 34, taking into account possible altitude variations. By choosing random values of model parameters, we calculate 1000 random background spectra at any given altitude. The spread of these background model counts is used to represent the uncertainties associated with the background model. This procedure is repeated for all altitudes between 950 and 1200 km, which essentially constructs an error matrix depending on both altitude and M/Z.

Finally, we discuss briefly the potential sources for the background spectra. The fact that the background counts decrease with increasing altitude suggests that these signals are related to processes in the ambient atmosphere. Titan's thermosphere coexists with an ionosphere (e.g., Bird et al., 1997; Wahlund et al., 2005; Kliore et al., 2008), that could be created through either photoionization by solar EUV radiation or impact ionization by precipitating electrons/ions from Saturn's magnetosphere (e.g., Nagy and Cravens, 1998). Although reduced by an external tantalum shield, the highly energetic particles such as suprathermal electrons created in Titan's ionosphere can contribute to a residual count rate on the INMS detector which is not separated by quadrupole selection according to M/Z (Waite et al., 2004). This is likely the cause of the constant background level incorporated in our empirical model. The thermal background noise in the INMS detectors is not relevant here, since it is much weaker, producing signals of order 1 count min^{-1}, and it should not vary significantly with altitude (Waite et al., 2004). The origin for the broad structure centered near channel 25 is still unknown. The leakage of N_2^+ ions from mass channel 28 is not a concern, since the shape of the background spectra is too broad to be interpreted by overflow (see Section A.6). In this paper, we will not attempt to provide a physical model for the broad distribution of background counts described here. However, it is worth emphasizing that such a model should be able to account for both the shape and altitude dependence of the background spectra. Also, in Figs. 33 and 34, the solid and open symbols represent background model parameters obtained from inbound and outbound mass spectra, respectively. No systematic difference between inbound and outbound appears to be present. This indicates that the parent molecules responsible for the broad distribution of background counts are not involved in wall effects (see Section 4.1).

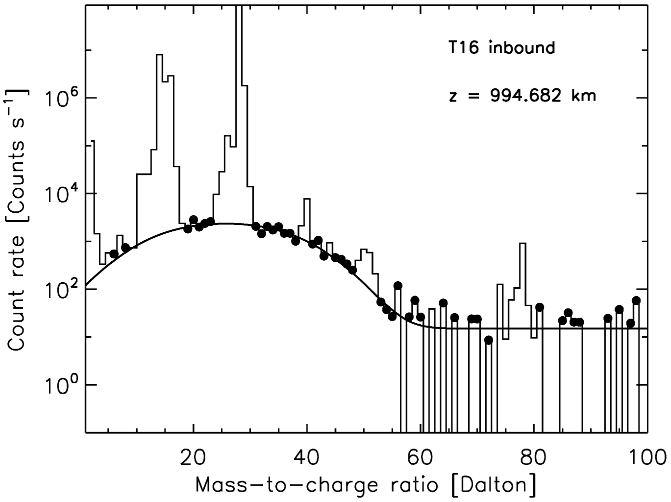

Fig. 35. The empirical model fitting of the background spectrum for the inbound T16 data at an altitude of ∼995 km. The histogram shows the full observed mass spectrum, and the solid line gives the best-fit background model. The model fitting is based on counts in channels not affected by neutral constituents in the ambient atmosphere, represented by the solid circles.

A.5.2. Residual gas in the INMS chamber

In addition to the empirical background model described above, residual gases in the INMS antechamber represent an additional channel-specific background that must be subtracted. As compared to the empirical background model which occupies all mass channels and shows strong altitude variations as illustrated in Fig. 34, the residual gases in the chamber tend to create constant background signals in mass slots occupied by neutral species, including H_2, CH_4, H_2O, N_2, CO, CO_2 and probably other inert species (Waite et al., 2004). An example for the inbound T18 flyby is given in Fig. 36, which shows the mean inbound (solid line) and outbound

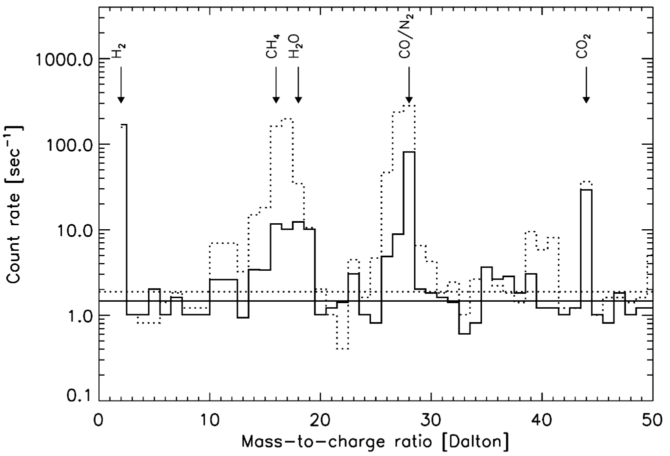

Fig. 36. The mean mass spectra obtained between 10,000 km and 20,000 km for the inbound (solid) and outbound (dotted) T18 flybys. These spectra are produced by the residual gases in the INMS chamber, including H_2, CH_4, H_2O, N_2, CO and CO_2 (marked by arrows). The horizontal straight lines indicate the constant background levels, corresponding to the mean values calculated from counts in channels not occupied by residual gases.

(dotted line) mass spectra obtained by averaging counts between 10,000 km and 20,000 km. Peaks associated with H_2, CH_4, H_2O, N_2, CO and CO_2 are marked with arrows. At such far distances from Titan, the densities of all ambient neutral species become vanishingly small, with the only possible source for the observed counts being residual gases in the INMS chamber.

To obtain accurate densities of neutral constituents in Titan's atmosphere, the contributions from these residual gases are subtracted from the observed mass spectra (e.g., Cui et al., 2008). Inbound and outbound spectra are treated separately, because Fig. 36 shows that the residual signals recorded during the outbound legs are systematically higher than those recorded during the inbound legs, a signature of the wall effect as described in Section 4.1. For the T25 flyby and the outbound T37 flyby during which no INMS measurements were made above ~10,000 km, the residual spectra averaged over all the other flybys are adopted. The residual spectra show constant background levels, as indicated by the horizontal straight lines in Fig. 36, which are calculated as the mean values of counts in those channels not occupied by possible residual gases. These constant background levels are analogous to the constant term, *c* in Eq. (A.3), and need to be subtracted from the spectra of the residual gases before removing their contributions to the observed INMS spectra. It is interesting to note that the background level of order 1 count s^{-1} shown in Fig. 36 is consistent with the asymptotic value of the constant background above ~1100 km shown in the upper panel of Fig. 34. This implies a common origin for both background signals, which is likely to be the energetic particles in Titan's ionosphere, as mentioned above.

A.6. Channel crosstalk

The INMS quadrupole mass analyzer consists of four rods mounted in a mechanical assembly and excited by radio frequency (RF) and direct current (DC) potentials (Waite et al., 2004). While the combination of the RF amplitude and frequency (either 3.57 MHz and 1.64 MHz) determines the transmitted M/Z, the resolution is controlled by the ratio of the DC and RF amplitudes (Waite et al., 2004). The finite resolving capability indicates that the incident ions are never separated perfectly according to M/Z, but rather produce a spectrum that spills over slightly into adjacent channels. An example is given in Fig. 37, which shows the mass spectrum for the N_2 reference gas obtained during the FU characterization. While the peaks at channels 28 and 29 reflect contributions from N_2 and its isotope $^{14}N^{15}N$, the residual counts at surrounding channels (especially channel 27) are interpreted by channel crosstalk. Notice that the minor peak at channel 32 is likely to be caused by O_2 impurities in the calibration chamber.

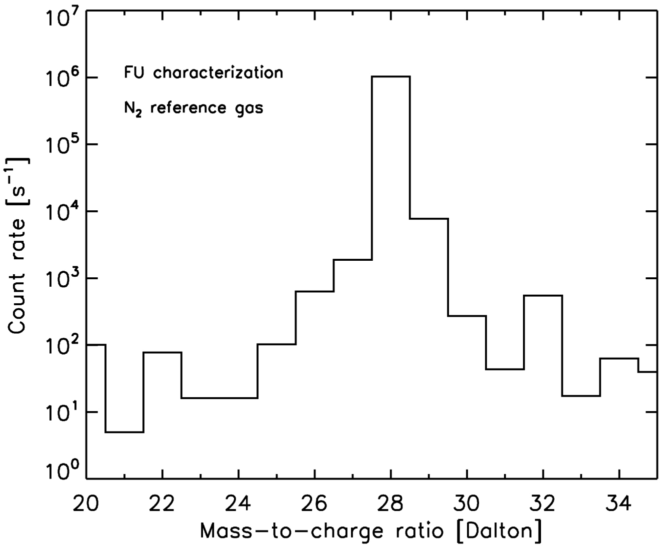

Fig. 37. The mass spectrum for the N_2 reference gas used for FU characterization. Only the portion near M/Z ~ 28 is shown. While counts in channels 28 and 29 are clearly associated with N_2 and $^{14}N^{15}N$, the residual counts in surrounding channels are interpreted as a result of channel crosstalk. The minor peak at channel 32 is caused by O_2 impurities in the calibration chamber.

In principle, the FU spectrum for the N_2 reference gas allows us to characterize crosstalk near channel 28, which can then be used to correct for the same effect in an observed spectrum. Based on the data shown in Fig. 37, we estimate that the overflow of counts from channel 28 to 27 is approximately 0.15%. As an example, the count rate in channel 28 is $\sim 5 \times 10^8$ counts s^{-1} at C/A of the T16 flyby. This implies that the signal in channel 27 due to crosstalk is $\sim 8 \times 10^5$ counts s^{-1}, about a factor of 3 higher than the actual count rate. This indicates that the overflow of counts from channel 28 to 27 is overestimated by the crosstalk pattern shown in the mass spectra of the N_2 reference gas. We expect that the correction for crosstalk may strongly depend on the pressure or density of the measured gas, and therefore the reference N_2 spectrum cannot be directly used to correct for channel crosstalk in the observed INMS spectra. Due to the lack of a reliable way to correct for such an instrumental effect, channel 27 will be excluded in our spectral analysis, which prevents us from determining the HCN abundance in Titan's atmosphere.

Fortunately, the correction for crosstalk is not important for other channels, since the signals produced by ambient neutrals are always much higher than those due to crosstalk. As an example, we estimate that the counts in channel 39 caused by overflow from channel 40 are about 0.1% of those caused by the ambient atmosphere. Here, we assume that the channel 40 count is due to ^{40}Ar, with a typical mixing ratio of 5×10^{-6} (Yelle et al., 2008), and that channel 39 count is due to CH_3C_2H, with a typical mixing ratio of 1×10^{-5} (Wilson and Atreya, 2004). We have also used the fact that the ^{40}Ar sensitivity at channel 40 is about 50% higher than the CH_3C_2H sensitivity at channel 39. The difference in the ram enhancement factors for these two species is ignored for simplicity. We will not correct for the overflow from channel 28 to 29 for the same reason, i.e., the counts caused by the ambient $^{14}N^{15}N$ molecules are much higher that those due to crosstalk. In addition, the effect of crosstalk is usually within 1 Dalton (Waite et al., 2004), thus the overflow of counts from channel 28 to more distant channels such as channel 26 is also ignored.

References

Backes, H., Neubauer, F.M., Dougherty, M.K., Achilleos, N., André, N., Arridge, C.S., Bertucci, C., Jones, G.H., Khurana, K.K., Russell, C.T., Wennmacher, A., 2005. Titan's magnetic field signature during the first Cassini encounter. Science 308, 992–995, doi:10.1126/science.1109763.

Banaszkiewicz, M., Lara, L.M., Rodrigo, R., Lòpez-Moreno, J.J., Molina-Cuberos, G.J., 2000. A coupled model of Titan's atmosphere and ionosphere. Icarus 147, 386–404, doi:10.1006/icar.2000.6448.

Bernard, J.-M., Coll, P., Coustenis, A., Raulin, F., 2003. Experimental simulation of Titan's atmosphere: Detection of ammonia and ethylene oxide. Planet. Space Sci. 51, 1003–1011, doi:10.1016/S0032-0633(03)00131-4.

Bézard, B., Coustenis, A., McKay, C.P., 1995. Titan's stratospheric temperature asymmetry: A radiative origin? Icarus 113, 267–276, doi:10.1006/icar.1995.1023.

Bird, M.K., Dutta-Roy, R., Asmar, S.W., Rebold, T.A., 1997. Detection of Titan's ionosphere from Voyager 1 radio occultation observations. Icarus 130, 426–436, doi:10.1006/icar.1997.5831.

Brecht, S.H., Luhmann, J.G., Larson, D.J., 2000. Simulation of the saturnian magnetospheric interaction with Titan. J. Geophys. Res. 105, 13119–13130, doi:10.1029/1999JA900490.

Broadfoot, A.L., and 15 colleagues, 1981. Extreme ultraviolet observations from Voyager 1 encounter with Saturn. Science 212, 206–211, doi:10.1126/science.212.4491.206.

Coustenis, A., Salama, A., Schulz, B., Ott, S., Lellouch, E., Encrenaz, T.H., Gautier, D., Feuchtgruber, H., 2003. Titan's atmosphere from ISO mid-infrared spectroscopy. Icarus 161, 383, doi:10.1016/S0019-1035(02)00028-3.

Coustenis, A., and 24 colleagues, 2007. The composition of Titan's stratosphere from Cassini/CIRS mid-infrared spectra. Icarus 189, 35–62, doi:10.1016/j.icarus.2006.12.022.

Cravens, T.E., Keller, C.N., Ray, B., 1997. Photochemical sources of non-thermal neutrals for the exosphere of Titan. Planet. Space Sci. 45, 889–896, doi:10.1016/S0032-0633(97)00064-0.

Cravens, T.E., and 15 colleagues, 2006. Composition of Titan's ionosphere. Geophys. Res. Lett. 33, doi:10.1029/2005GL025575. L07105.

Cui, J., Yelle, R.V., Volk, K., 2008. Distribution and escape of molecular hydrogen in Titan's thermosphere and exosphere. J. Geophys. Res. 113, doi:10.1029/2007JE003032. E10004.

De La Haye, V., and 12 colleagues, 2007a. Cassini INMS data in Titan's upper atmosphere and exosphere: Observation of a suprathermal corona. J. Geophys. Res. 112, doi:10.1029/2006JA012222. A07309.

De La Haye, V., Waite, J.H., Cravens, T.E., Nagy, A.F., Johnson, R.E., Lebonnois, S., Robertson, I.P., 2007b. Titan's corona: The contribution of exothermic chemistry. Icarus 191, 236–250, doi:10.1016/j.icarus.2007.04.031.

Feigelson, E.D., Nelson, P.I., 1985. Photochemical sources of non-thermal neutrals for the exosphere of Titan statistical methods for astronomical data with upper limits. I. Univariate distributions. Astrophys. J. 293, 192–206, doi:10.1086/163225.

Fox, J.L., Yelle, R.V., 1997. Hydrocarbon ions in the ionosphere of Titan. Geophys. Res. Lett. 24, 2179–2182.

Gan, L., Keller, C.N., Cravens, T.E., 1992. Electrons in the ionosphere of Titan. J. Geophys. Res. 97, 12137–12151.

Hörst, S.M., Vuitton, V., Yelle, R.V., 2008. The origin of oxygen species in Titan's atmosphere. J. Geophys. Res. 113, doi:10.1029/2008JE003135. E10006.

Hunten, D.M., 1972. The atmosphere of Titan. Comments Astrophys. Space Phys. 4, 149.

Ip, W.-H., 1990. Titan's upper ionosphere. Astrophys. J. 362, 354–363, doi:10.1086/169271.

Kasprzak, W.T., Hedin, A.E., Niemann, H.B., Spencer, N.W., 1980. Atomic nitrogen in the upper atmosphere of Venus. Geophys. Res. Lett. 7, 106–108.

Keller, C.N., Cravens, T.E., Gan, L., 1992. A model of the ionosphere of Titan. J. Geophys. Res. 97, 12117–12135.

Kliore, A.J., and 12 colleagues, 2008. First results from the Cassini radio occultations of the Titan ionosphere. J. Geophys. Res. 113, A09317, doi:10.1029/2007JA012965.

Lammer, H., Bauer, S.J., 1993. Atmospheric mass loss from Titan by sputtering. Planet. Space Sci. 41, 657–663, doi:10.1016/0032-0633(93)90049-8.

Lammer, H., Stumptner, W., Bauer, S.J., 1998. Dynamic escape of H from Titan as consequence of sputtering induced heating. Planet. Space Sci. 46, 1207–1213, doi:10.1016/S0032-0633(98)00050-6.

Lara, L.M., Lellouch, E., Lòpez-Moreno, J.J., Rodrigo, R., 1996. Vertical distribution of Titan's atmospheric neutral constituents. J. Geophys. Res. 101, 23261–23283, doi:10.1029/96JE02036.

Lavvas, P.P., Coustenis, A., Vardavas, I.M., 2008a. Coupling photochemistry with haze formation in Titan's atmosphere. Part I. Model description. Planet. Space Sci. 56, 27–66, doi:10.1016/j.pss.2007.05.026.

Lavvas, P.P., Coustenis, A., Vardavas, I.M., 2008b. Coupling photochemistry with haze formation in Titan's atmosphere. Part II. Results and validation with Cassini/Huygens data. Planet. Space Sci. 56, 67–99, doi:10.1016/j.pss.2007.05.027.

Ledvina, S.A., Cravens, T.E., Salman, A., Kecskemety, K., 2000. Ion trajectories in Saturn's magnetosphere near Titan. Adv. Space Res. 26, 1691–1695, doi:10.1016/S0273-1177(00)00075-2.

Lellouch, E., Hunten, D.M., Kockarts, G., Coustenis, A., 1990. Titan's thermosphere profile. Icarus 83, 308–324, doi:10.1016/0019-1035(90)90070-P.

Luhmann, J.G., 1996. Titan's ion exosphere wake: A natural ion mass spectrometer? J. Geophys. Res. 101, 29387–29393, doi: 10.1029/96JE03307.

Lunine, J.I., Yung, Y.L., Ralph, D.L., 1999. On the volatile inventory of Titan from isotopic abundances in nitrogen and methane. Planet. Space Sci. 47, 1291–1303, doi:10.1016/S0032-0633(99)00052-5.

Marten, A., Hidayat, T., Biraud, Y., Moreno, R., 2002. New millimeter heterodyne observations of titan: Vertical distributions of nitriles HCN, HC_3N, CH_3CN, and the Isotopic Ratio $^{15}N/^{14}N$ in its atmosphere. Icarus 158, 532–544, doi:10.1006/icar.2002.6897.

Mason, E.A., Marrero, T.R., 1970. The diffusion of atoms and molecules. In: Bates, D.R., Esterman, I. (Eds.), Advances in Atomic and Molecular Physics. Academic Press, San Diego, CA, pp. 155–232.

Michael, M., Johnson, R.E., 2005. Energy deposition of pickup ions and heating of Titan's atmosphere. Planet. Space Sci. 53, 1510–1514, doi:10.1016/j.pss.2005.08.001.

Michael, M., Johnson, R.E., Leblanc, F., Liu, M., Luhmann, J.G., Shematovich, V.I., 2005. Ejection of nitrogen from Titan's atmosphere by magnetospheric ions and pick-up ions. Icarus 175, 263–267, doi:10.1016/j.icarus.2004.11.004.

Müller-Wodarg, I.C.F., Yelle, R.V., 2002. The effect of dynamics on the composition of Titan's upper atmosphere. Geophys. Res. Lett. 29 (23), 2139, doi:10.1029/2002GL016100.

Müller-Wodarg, I.C.F., Yelle, R.V., Mendillo, M., Young, L.A., Aylward, A.D., 2000. The thermosphere of Titan simulated by a global three-dimensional time-dependent model. J. Geophys. Res. 105 (A9), 20833–20856, doi:10.1029/2000JA000053.

Müller-Wodarg, I.C.F., Yelle, R.V., Mendillo, M.J., Aylward, A.D., 2003. On the global distribution of neutral gases in Titan's upper atmosphere and its effect on the thermal structure. J. Geophys. Res. 108 (A12), 1453, doi:10.1029/2003JA010054.

Müller-Wodarg, I.C.F., Yelle, R.V., Borggren, N., Waite Jr., J.H., 2006. Waves and horizontal structures in Titan's thermosphere. J. Geophys. Res. 111, doi:10.1029/2006JA011961. A12315.

Müller-Wodarg, I.C.F., Yelle, R.V., Cui, J., Waite Jr., J.H., 2008. Horizontal structure and dynamics of Titan's thermosphere. J. Geophys. Res. 113, doi:10.1029/2007JE003033. E10005.

Nagy, A.F., Cravens, T.E., 1998. Titans ionosphere: A review. Planet. Space Sci. 46, 1149–1155.

Niemann, H.B., and 17 colleagues, 2005. The abundances of constituents of Titan's atmosphere from the GCMS instrument on the Huygens probe. Nature 438, 779–784, doi:10.1038/nature04122.

Press, W.H., Teukolsky, S.A., Vetterling, W.T., Flannery, B.P., 1992. Numerical Recipes in C: The Art of Scientific Computing, second ed. Cambridge Univ. Press, Cambridge, UK, pp. 681–688.

Rishbeth, H., Yelle, R.V., Mendillo, M., 2000. Dynamics of Titan's thermosphere. Planet. Space Sci. 48, 51–58, doi:10.1016/S0032-0633(99)00076-8.

Shematovich, V.I., Tully, C., Johnson, R.E., 2001. Suprathermal nitrogen atoms and molecules in Titan's corona. Adv. Space Res. 27, 1875–1880, doi:10.1016/S0273-1177(01)00268-X.

Shematovich, V.I., Johnson, R.E., Michael, M., Luhmann, J.G., 2003. Nitrogen loss from Titan. J. Geophys. Res. 108 (E8), 5087, doi:10.1029/2003JE002096.

Smith, G.R., Strobel, D.F., Broadfoot, A.L., Sandel, B.R., Shemansky, D.E., Holberg, J.B., 1982. Titan's upper atmosphere—Composition and temperature from the EUV solar occultation results. J. Geophys. Res. 87, 1351–1359, doi:10.1029/JA087iA03p01351.

Strobel, D.F., Shemansky, D.E., 1982. EUV emission from Titan's upper atmosphere—Voyager 1 encounter. J. Geophys. Res. 87, 1361–1368, doi:10.1029/JA087iA03p01361.

Strobel, D.F., Summers, M., Zhu, X., 1992. Titan's upper atmosphere: Structure and ultraviolet emissions. Icarus 100, 512–526, doi:10.1016/0019-1035(92)90114-M.

Teanby, N.A., and 11 colleagues, 2007a. Latitudinal variations of HCN, HC_3N, and C_2N_2 in Titan's stratosphere derived from Cassini CIRS data. Icarus 181, 243–255, doi:10.1016/j.icarus.2005.11.008.

Teanby, N.A., and 11 colleagues, 2007b. Vertical profiles of HCN, HC_2N, and C_2H_2 in Titan's atmosphere derived from Cassini/CIRS data. Icarus 186, 364–384, doi:10.1016/j.icarus.2006.09.024.

Toublanc, D., Parisot, J.P., Brillet, J., Gautier, D., Raulin, F., McKay, C.P., 1995. Photochemical modeling of Titan's atmosphere. Icarus 113, 2–26, doi:10.1006/icar.1995.1002.

Vervack, R.J., Sandel, B.R., Strobel, D.F., 2004. New perspectives on Titan's upper atmosphere from a reanalysis of the Voyager 1 UVS solar occultations. Icarus 170, 91–112, doi:10.1016/j.icarus.2004.03.005.

Vuitton, V., Yelle, R.V., Anicich, V.G., 2006. The nitrogen chemistry of Titan's upper atmosphere revealed. Astrophys. J. 647, L175–L178, doi:10.1086/507467.

Vuitton, V., Yelle, R.V., McEwan, M.J., 2007. Ion chemistry and N-containing molecules in Titan's upper atmosphere. Icarus 191, 722–742, doi:10.1016/j.icarus.2007.06.023.

Vuitton, V., Yelle, R.V., Cui, J., 2008. Formation and distribution of benzene on Titan. J. Geophys. Res. 113 (E5), E05007, doi:10.1029/2007JE002997.

Wahlund, J.-E., and 17 colleagues, 2005. Cassini measurements of cold plasma in the ionosphere of Titan. Science 308, 986–989, doi:10.1126/science.1109807.

Waite Jr., J.H., and 15 colleagues, 2004. The Cassini Ion and Neutral Mass Spectrometer (INMS) investigation. Space Sci. Rev. 114, 113–231, doi:10.1007/s11214-004-1408-2.

Waite Jr., J.H., and 21 colleagues, 2005. Ion Neutral Mass Spectrometer results from the first flyby of Titan. Science 308, 982–986, doi:10.1126/science.1110652.

Waite, J.H., Young, D.T., Cravens, T.E., Coates, A.J., Crary, F.J., Magee, B., Westlake, J., 2007. The process of tholin formation in Titan's upper atmosphere. Science 316, 870–875, doi:10.1126/science.1139727.

Wilson, E.H., Atreya, S.K., 2004. Current state of modeling the photochemistry of Titan's mutually dependent atmosphere and ionosphere. J. Geophys. Res. 109 (E6), doi:10.1029/2003JE002181. E06002.

Yelle, R.V., 1991. Non-LTE models of Titan's upper atmosphere. Astrophys. J. 383, 380–400, doi:10.1086/170796.

Yelle, R.V., Borggren, N., De La Haye, V., Kasprzak, W.T., Niemann, H.B., Müller-Wodarg, I.C.F., Waite Jr., J.H., 2006. The vertical structure of Titan's upper atmosphere from Cassini Ion Neutral Mass Spectrometer measurements. Icarus 182, 567–576, doi:10.1016/j.icarus.2005.10.029.

Yelle, R.V., Cui, J., Müller-Wodarg, I.C.F., 2008. Eddy diffusion and methane escape from Titan's atmosphere. J. Geophys. Res. 113 (E10), doi:10.1029/2007JE003031. E10003.

Yung, Y.L., Allen, M., Pinto, J.P., 1984. Photochemistry of the atmosphere of Titan: Comparison between model and observations. Astrophys. J. Suppl. 55, 465–506, doi:10.1086/190963.